

Anisotropic and Tunable Characteristics of the Colloidal Behavior of Metal Oxide Surfaces

by

Joseph W. Bullard, III

B.S. Materials Science and Engineering (2000)
Rice University

S.M. Materials Science and Engineering (2003)
Massachusetts Institute of Technology

SUBMITTED TO THE DEPARTMENT OF MATERIALS SCIENCE AND ENGINEERING
IN PARTIAL FULFILLMENT OF THE REQUIREMENTS FOR THE DEGREE OF

DOCTOR OF PHILOSOPHY IN MATERIALS SCIENCE AND ENGINEERING
AT THE
MASSACHUSETTS INSTITUTE OF TECHNOLOGY

SEPTEMBER 2006

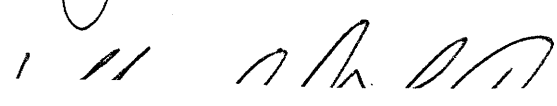
© 2006 Massachusetts Institute of Technology. All rights reserved.

Signature of Author: _____


Department of Materials Science and Engineering

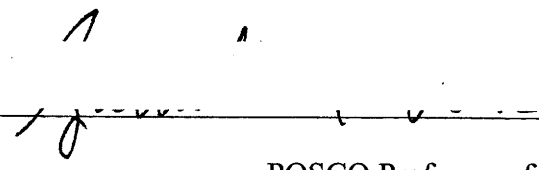
June 28, 2006

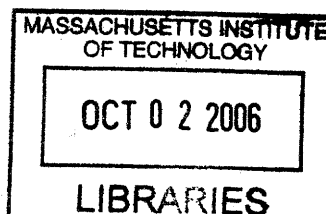
Certified by: _____


Sumitomo Electric Industries Professor of Engineering

Thesis Supervisor

Accepted by: _____


Samuel M. Allen
POSCO Professor of Physical Metallurgy
Chair, Departmental Committee on Graduate Studies



ARCHIVES

Anisotropic and Tunable Characteristics of the Colloidal Behavior of Metal Oxide Surfaces

by

Joseph W. Bullard, III

Submitted to the department of Materials Science and Engineering
on June 28, 2006, in partial fulfillment of the requirements for the
degree of Doctor of Philosophy in Materials Science and
Engineering.

ABSTRACT

The electroosmotic behavior of the rutile polymorph of titanium dioxide was explored as a function of crystallographic orientation. Atomic force microscopy (AFM) was employed to make high-resolution force spectroscopy measurements between a silica sphere attached to a traditional, contact-mode AFM cantilever and TiO₂ (110), (100), and (001) surfaces in aqueous solutions. Measurements were taken in a variety of solution conditions across a broad range of pH values, and the resultant force-distance curves were used to deduce relative behaviors of each orientation of rutile, with particular interest in changes of the isoelectric point (iep). Differences in iep as a function of orientation are explained in terms of differences in both the coordination number and density of (Lewis) acidic and basic sites on the surface. The results were supported by angle-resolved X-ray photoelectron spectroscopy (XPS) measurements of a nominal monolayer of palladium metal deposited on each of the three orientations studied. The palladium monolayer served as a means of probing the relative electron affinities of the three surfaces studied, which was exhibited in shifts of the palladium XPS peak that corresponded to differences in binding energy as a function of substrate orientation. The correlation between rutile orientation and shift in palladium binding energy corresponded directly to the relationship between isoelectric point and orientation, with the surface of lowest isoelectric point exhibiting the highest Pd binding energy.

Force spectroscopy was also used to investigate the changes in the electroosmotic behavior of rutile surfaces induced by exposure to ultraviolet irradiation (UV). Force-distance measurements using a silica sphere in aqueous potassium chloride solutions were performed on surfaces exposed to UV, and compared with data taken on identically oriented surfaces stored in darkness. Changes in the characteristics of both the extension and retraction components of the force measurements were observed. Differences in the former suggest changes in the double layer characteristics of the rutile surfaces, whereas differences in the latter denote changes in the adhesion forces between the probing silica sphere and the surface.

Thesis Supervisor: Michael J. Cima

Title: Sumitomo Electric Industries Professor of Engineering

ACKNOWLEDGEMENTS

The completion of my thesis has at times felt rushed, while at others it has seemed brilliantly stimulating. Still other occasions of reflection have crushed me with its seemingly impossible weight. Pausing for a moment to take stock in my time at MIT, I am left, after six wonderful and difficult years, with more questions to ask than ones I have answered. I remain uncertain about many things, but am absolutely sure about a single truth: I did not do this alone.

The work detailed in these pages is a testament to the power of collaboration and the fruit of the labors of many. Help has come in many forms over the past six years, and has at times come from people who were likely unaware that they were even giving it. Help has also come both directly and indirectly, as insightful analysis in the lab and as nonsensical humor at the pub, as well as in many ways between. There is no way to express how grateful I am for all of it, and I will not be able to do its impact justice in just a few short paragraphs.

I would like to begin by thanking my thesis advisor, Michael Cima. His guidance and support over the years have helped to mold this work in so many ways, and I am grateful for his mentorship. Michael's approach to materials science is nothing short of inspirational; his ability to identify important technological problems and chart an effective course of study amazes me, and his firm grasp of such a breadth of relevant fields is something to aspire to. My time in his lab has taught me far more than the work presented here, and I will constantly look to his example as I begin to develop my own scientific career.

I must also thank the numerous members of CPRL, whose input, friendships, and support have been invaluable to me on a daily basis. I would like to particularly thank Ryan Kershner, with whom I worked so closely during the first six months of my time in Michael's lab. The strides made in his thesis and the time we spent working together truly laid the foundation to the work in this thesis. I would also like to thank Chris Vassiliou and Dan Wesolowski, who at various times put their own projects aside to lend their programming expertise to me. What took them many hours may have saved me many months. I am also indebted to Barbara Layne, Lenny Rigione, and John Centorino for all of their support in so many ways over the years.

There are also a number of students and staff around MIT and outside of CPRL who have provided me with their time, talents, and insights over the years. Libby Shaw, Kurt Broderick, David Bono, Tim McLure, Jorge Feuchtwanger, Jen Vandiver, and Siddarth Kumar have all given so much to me so generously in many different ways.

I have also been fortunate to have made many great friendships in my time at MIT. Spending Wednesday evenings at the Muddy with Josh Hertz, Dan Sparacin, Ryan Williams, and Nate Vandesteege is something that I always looked forward to, and sharing in a good laugh, a spirited debate, or musings of work-related struggles has been an invigorating source of support to me. I will take with me many memories of so many wonderful times with them at MIT.

Coming home to Boston after four years of college in Texas has also been an amazing blessing in my time at MIT. To celebrate holidays, to enjoy a dinner with my parents, wife, and sister at the house where I grew up, to spend Christmas with grandparents, aunts, uncles, and cousins, has

been a joy. I would like to particularly acknowledge my parents, Joe and Bonnie, who have always taken a loving interest in my successes and failures. Their emphasis on hard work and their enthusiasm for everything that I have attempted in life is something that I hope I can emulate one day with children of my own. I would also like to thank my sister, Christine, whose love and friendship I will always hold close.

Last, my wife Vanessa, who has never known me as anything but a graduate student, has been an incredible force behind the efforts detailed in these pages. Her love and support have not only helped me through my most difficult hours, but have also inspired me to strive to do my very best. She has been a sounding-board for frustration, a weekend and late-night lab companion, and a potent source of strength and encouragement for as long as I can remember. Her delicious cooking and tender care to all of life's details have lent an anchor of sanity to some very insane times, and I will always be thankful to her for all of it. She has been an inspiration and a rock, and in many ways I consider this thesis ours, not mine.

*Old father, old artificer, stand me
now and ever in good stead.*

- James Joyce

Table of Contents

1. Introduction.....	12
1.1 Motivation for this Study.....	12
1.2 Additional Areas of Importance.....	19
1.3 The Purpose of this Work.....	19
1.4 Organization of the Thesis.....	20
1.5 References.....	21
2. Theoretical Background and Experimental Technique.....	25
2.1 Organization.....	25
2.2 Origins of the Electrical Double Layer: Gouy-Chapman Theory.....	25
2.2.1 The Poisson-Boltzmann Equation.....	26
2.3 Stern and Debye Layer Components of the EDL.....	30
2.4 The Double Layer and Forces Between Suspended Bodies.....	31
2.4.1 Interactions Between Flat Surfaces of Identical Constant Potential.....	32
2.4.2 Interactions Between Different Surfaces of Constant Potential or Charge.....	37
2.4.3 The Derjaguin Approximation.....	37
2.4.4 The Linear Superposition Approximation.....	39
2.5 Probing the Double Layer: Zeta Potential.....	40
2.6 Double Layer Formation on Oxide Surfaces.....	43
2.7 Force Distance Spectroscopy.....	44
2.7.1 General Overview.....	44
2.7.2 Anatomy of a Force-distance Curve.....	47
2.8 X-Ray Photoelectron Spectroscopy.....	50
2.9 References.....	51
3. Orientation Dependence of Surface Properties of Sapphire.....	56
3.1 Preface.....	56
3.2 Streaming Potential and XPS Results.....	56
3.3 Discussion: Developing Structure-Property Relationships.....	59
3.4 Refereneces.....	63

4. Anisotropy of the IEP of Rutile Surfaces.....	65
4.1 Introduction.....	65
4.2 Materials and Methods.....	66
4.2.1 Solution and Sample Preparation.....	66
4.2.2 AFM Measurements.....	67
4.2.3 Zeta Potential Measurements of Particles.....	69
4.2.4 X-ray Photoelectron Spectroscopy (XPS).....	69
4.3 Results.....	70
4.3.1 Zeta Potential of Silica and Rutile Powder Suspensions.....	70
4.3.2 Surface Characterization.....	72
4.3.3 Force Spectroscopy.....	73
4.3.3.1 General Criterea.....	73
4.3.3.2 Correlation of AFM Data to Streaming Potential Measurements.....	78
4.3.3.3 Force Spectroscopy Results of Rutile.....	79
4.3.4 X-Ray Photoelectron Spectroscopy.....	83
4.4 Discussion.....	85
4.4.1 Structure of the (110) Rutile Surface.....	85
4.4.2 Structure of the (100) Rutile Surface.....	85
4.4.3 Structure of the (001) Rutile Surface.....	87
4.4.4 Influence of Hydroxyl Groups on Surface Behavior.....	89
4.4.5 Connections Between Single Crystalline and Powder Behavior.....	91
4.5 Conclusions.....	92
4.6 References.....	93
5. Photoinduced changes in EDL Properties of Rutile Surfaces.....	98
5.1 Introduction.....	98
5.2 Materials and Methods.....	99
5.3 Results.....	101
5.3.1 EDL Interactions of the Rutile (100) Surface.....	101
5.3.2 EDL Interactions of the Rutile (110) Surface.....	105
5.3.3 Photoinduced Changes in Adhesion Forces on Rutile Surfaces.....	108

5.4 Discussion.....	109
5.4.1 Influence of UV on EDL Interactions.....	109
5.4.2 Influence of UV on Forces of Adhesion.....	111
5.5 References.....	113
6. Summary and Future Work.....	115
Appendix: Matlab AFM Analysis Program.....	120

Chapter 1: Motivation, Purpose and Organization of this Thesis

1.1 Motivation for this Study: Novel Assembly Methods for Novel Materials

The broad field of materials science is rife with examples of decreasing lengthscales in both emerging and extant materials technologies. The technological push for all things macro- to become micro-, and all things micro- to shrink to nano- is a driving force in reducing the size of nearly everything. This push is approached in a variety of ways, including the direct reduction of the active volumes of existing materials systems, as seen in the development of thin film and micro-battery technology. Other areas call for novel approaches to redesign existing concepts, a phenomenon clearly evident in the race to keep up with Moore's Law by finding new ways to shrink the lengthscales of electronic transistors beyond the limits of conventional microfabrication techniques. The development of nanoscale and molecular transistors falls into this category [1-3]. Entirely new classes of materials with new properties to exploit are also emerging, redefining existing materials technologies and creating new ones. Colloidal crystal technology is one such example of this, as their development has found applications in areas as diverse as microfiltration devices, photonic band gap and wave guiding materials [4-11], and useful tools for developing effective models for understanding the dynamics of atomic crystal systems [12].

As lengthscales decrease, however, practical issues of efficient assembly and production begin to appear. Micro- and nanoscale materials systems exhibit physical phenomena that lie at the overlapping boundaries of ballistic, electrostatic, and colloidal behaviors. Their high surface to volume ratios require the consideration of previously insignificant surface forces acting on systems, as macroscopic bodies are too large to be significantly affected by any of these types of interactions. The result is that conventional assembly techniques begin to break down, as the small size of functional components reduces the ability of gravitational forces to override these microscale phenomena. An example of this is found in the development of passive microscale electronic components, such as miniature multilayer ceramic capacitors. The small size of such components is critical to increasing their density on functional circuit boards. However, the small size is also an obstacle to the use of conventional production techniques, as electrostatic forces become too strong to "pick and place" capacitors in their desired positions in circuitry. The

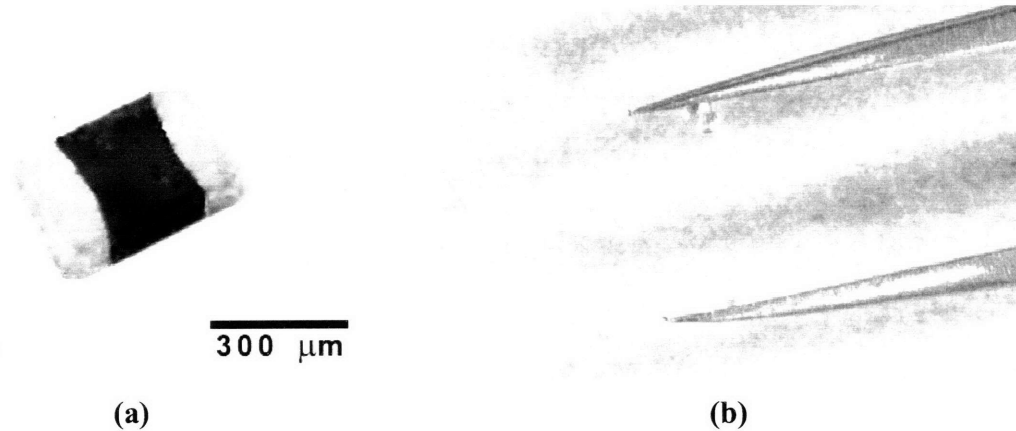
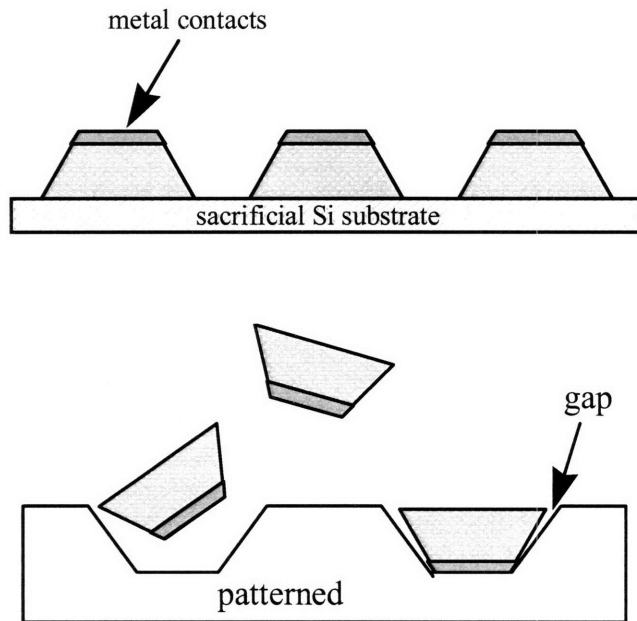


Figure 1.1: (a) A photograph of of the 0201 capacitor, having dimensions on the order of 300 μm . (b) The high surface-to-volume ratio leads to the dominance of electrostatic forces over gravitational forces, and the capacitor sticks to a pair of tweezers. This illustrates the problem with using conventional “pick and place” methods in efficient assembly techniques of micro- and nanoscale electronic components. [Taken from 13]

essence of this problem is shown in Figure 1.1, where an 0201 minichip capacitor, approximately 300 μm in length, is seen adhering to a pair of tweezers [13].

If a single capacitor is so difficult to manipulate, how can thousands be properly and efficiently positioned in their precise locations on a circuit board? Clearly, new approaches are required, and the surface forces impeding the use of conventional technologies must be at least understood, and ultimately manipulated. An example of a possible approach to a solution can be found in a proposal to integrate optoelectronic components such as GaAs LEDs on a silicon substrate [14]. The proposed approach requires the fabrication of trapezoidal LED components and etching pits of matching geometry in a silicon substrate, as shown in Figure 1.2. The devices are then suspended in a fluidic medium above the patterned substrate, and an external source of acoustic vibration is provided to hasten the settling of components into their desired locations. The directional geometry of both substrate and device allows for a lock-and-key type of fit, which enables the self-alignment of the LEDs in their positions. One significant observation from these experiments was that placement efficiency was inversely related to component size. Relatively large, 1 mm LEDs were readily positioned in their proper locations with near-perfect success. A reduction in LED size, however, corresponded to a decrease in positioning efficiency. Once again, this result can be attributed to increases in surface-to-volume ratios of the smaller devices, leading to an increase in the influence of surface forces relative to the gravitational

Figure 1.2. Schematic diagram of a proposed process for the fluidic assembly of GaAs LEDs on a patterned silica surface. The devices are fabricated to have a trapezoidal geometry (top), which promotes proper alignment between the patterned surface (bottom) and the electrical contacts of each LED. Taken from [14].



forces relied on for the positioning of larger components. While the initial successes of this method are evident, its shortcomings speak to the importance of studying the origins of these surface forces for improved assembly techniques.

Future generations of electronic devices are similarly plagued with controllable assembly issues defined by interactions between surfaces of various components. The fabrication of effective molecular transistors, for example, requires the placement of carbon nanotubes or other transistor molecules or nanoparticles between a pair of gold electrodes and above a gate dielectric [1-3], which is usually a silica or alumina surface. An example of a molecular transistor is shown in Figure 1.3. Current positioning techniques, however, involve suspending transistor molecules or nanotubes in solution and placing a droplet of the solution on top of an array of electrodes and deposited gate oxide. Successful positioning (and, consequently, transistor fabrication) relies upon achieving a desirable ratio of suspended molecules to patterned electrode pairs, and is highly uncertain.

Regardless of the laboratory successes of nanoscale and molecular electronic devices, their transfer to the marketplace will not be possible without effective, efficient assembly methods. Separation distances between electrodes can be on the order of 1nm, rendering the interactions between oxide surface and transistor molecules crucial to developing more effective

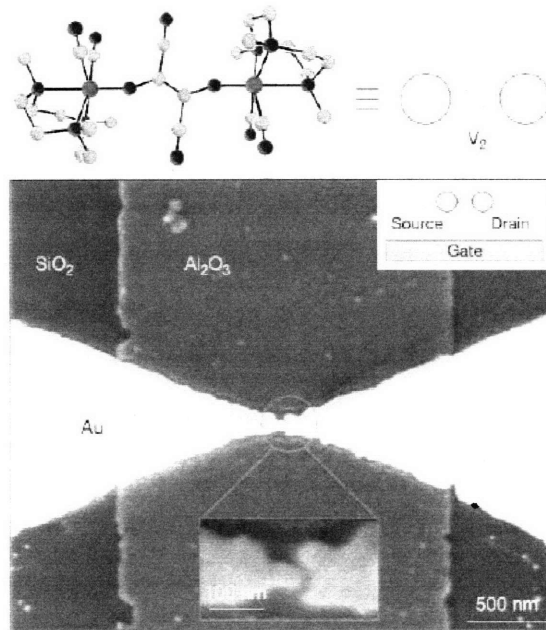


Figure 1.3. Image of an early molecular transistor. The bottom inset shows the nanoscale separation distances between source and drain, whereas the top inset shows a schematic of the cross-sectional view. The lengthscales of the entire transistor are on the order of interactions between the alumina substrate and the transisting molecule (shown above). These issues would also translate into electronic components build with small nanoparticles, as well. [Taken from 2].

placement techniques. A recent approach this problem capitalizes on the unique ability of various metal oxide surfaces to form self-assembled monolayers (SAMs) of phosponic acids, which can be tuned to selectively prevent or enhance the adsorption of single-walled carbon nanotubes [15].

However, the dimensionality of the controlled selectivity is limited by existing microcontact printing and lithographic techniques. Other researchers are attempting to use variations of conventional electrophoretic deposition processes to assemble transisting molecules at electrical contacts [16], illustrating both the richness of opportunity and the depth of difficulty in harnessing surface forces to work in favor of assembly.

The synthesis and manipulation of colloidal crystal systems is another growing area of materials technology with direct ties to studies in the surface forces that govern particle manipulation. These types of materials have found new and unique applications in a breadth of fields in recent years. Photonic bandgap materials, for example, can be produced by the arrangement of dielectric materials in periodic structures designed to filter specific electromagnetic states [4-6]. Colloidal crystals have been used to act either as a photonic material itself or as a template to be filled with a second material [4-11]. This latter technique,

upon removal of the templating microspheres, results in a porous periodic structure having a continuous air phase [8-11]. Recent work has utilized these structures as optical waveguides, with specific patterns of defects engineered into the crystal to guide light in a specified direction [17]. A variety of applications beyond photonics are also possible for these structures, including the development of microfilters and more efficient catalysts. Colloidal crystals have also found applications serving as model structures for the study of the mechanical deformation of solids at the atomic scale [12].

Colloidal crystal systems, however, are fundamentally limited by existing synthesis techniques. The predominant means of production of relatively large crystals relies on simple sedimentation processes or derivatives thereof [18-20]. This results in the close packing of each plane of particles, and the $\{111\}$ FCC orientation emerges as the only family of crystallographic surface terminations. Expanding the library of available crystal structures to colloid-based materials is critical to seeing its full promise reached as a new class of structures. Some methods have been already developed to create non-FCC crystals, but certain processes can be extraordinarily slow. Construction of a diamond cubic cell is possible, however, but it requires the individual positioning of colloid spheres of two different materials in alternating locations of a stack close-packed plane, followed by heat treatment above the decomposition temperature of one material and below the decomposition of the other [21], which leaves vacancies at exactly half of the lattice sites of the original structure. This method works well for constructing small structures for research purposes, but is not readily transferable to large-scale production techniques.

Various thrusts of materials research are now aimed at resolving the issues of directed assembly which are problematic to these myriad micro- and nanoscale technologies. One particular area of research that pertains to the work presented here is that of template systems for the direction of particle assembly. Ideal approaches to templated assembly capitalize on the very surface forces that impede the use of conventional production techniques, as they can be designed to either attract or repel suspended particles at specific locations on the substrate surface. Several micro-contact printing methods, for example, have been utilized to create templates to dictate the ordering of colloidal crystals, providing a means of producing ordered arrays of colloids on a surface [22-25]. The production of such materials using templated

assembly techniques requires a developed understanding of the interplay between template surface structure and its environment.

The essential component of any template-based approach to the directed assembly of any type of suspended media is the local variation of surface characteristics. Put simply, an effective template will have specified areas of strongly attracting and (ideally) repulsing interactions between substrate and suspended matter. There is no reason that such heterogeneous surface structures cannot be utilized as substrates for selective adsorption and templates for the directed assembly of molecular electronics as well as nano and microscale particles; the same fundamental principles should apply at any lengthscale.

A large emphasis in this field of study is the use of organic materials as the primary means of adding functionality to a surface. Self-segregating block copolymers, for example, readily assemble into ordered surfaces with periodically varying local characteristics [26-29]. The use of tailored monomer chemistries is an effective means for careful control of specific surface properties. The potential for engineered patterns of variant surface properties of inorganic crystals is certainly extant [30-34], and some have been engineered in the form of multi-material systems with applications in colloid science in mind. Work by Aksay, for example [34], uses masked ITO substrates to define locations preferable for particle adsorption. The photoresponsive behavior of the substrate is then used to electrophoretically manipulate suspended particles into their desired location. An example of this is shown in Figure 1.4.

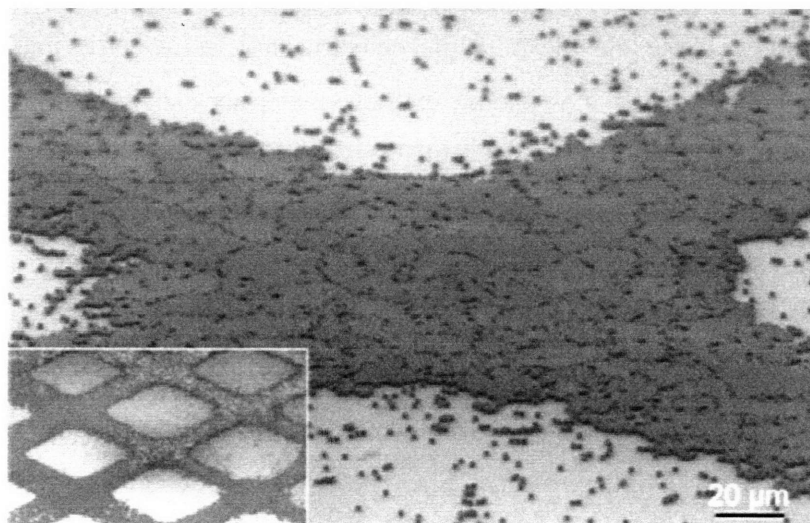


Figure 1.4. SEM images of the electrophoretic deposition of silica particles on an indium tin oxide (ITO) surface with specific regions of the surface exposed to light. From [34].

Such designer materials are less susceptible to degradation in numerous environments, largely insensitive to factors such as ultraviolet radiation, and stable over dramatically longer periods of time than their organic-based counterparts. Multi-material templates, however, are fundamentally limited by the limits of their processing lengthscales. Similar designer patterns on crystalline surfaces, on the other hand, might be achieved by careful control of defect structures and inclusion chemistry, reducing the complexity of the system and diminishing the roughness of the patterned surface to the order of a few angstroms. Cultivating this type of technology would rely on a well-developed understanding of relevant structure-property relations at the atomic level in crystal systems of interest.

The importance of atomic structure to colloidal behavior is outlined in subsequent chapters of this thesis. One natural conclusion drawn from a developed understanding of the intimate relationship between structure and properties is the assumption that changes in the atomic and electronic landscape of a particular surface will result in changes in the behaviors exhibited by that surface. This leads to further possibilities for using specific oxide surfaces as assembly templates by exploiting the externally tunable behaviors exhibited in certain types of systems. Surfaces of such active materials could serve as loci of functional interactions with a colloidal system. Conditions might be varied locally, for instance, to alter the nature of interactions with suspended particles, or to control the reaction of a dissolved molecule at the interface.

A variety of metal oxide systems of varying complexity currently exist with the potential for tunable applications. These include both piezoelectric and ferroelectric materials such as quartz and strontium titanate, as well as photoresponsive materials such as the rutile and anatase forms of titanium dioxide. The well-known behavior of piezoelectric materials, for example could be used to alter the electronic properties of a surface under the influence of an external mechanical stimulus. This approach is used in reverse in the field of surface acoustic wave (SAW) chemical sensors, a class of devices used for, among other things, the detection of biological agents in liquid media [56-57]. Typical SAW sensors consist of a piezoelectric crystal coated with an active layer to which ambient molecules adsorb. The presence of these adsorbed species is indicated in changes in the velocity and attenuation of acoustic wave signals generated between patterned electrodes on the piezoelectric surface. Applied electric fields might be used in lieu of mechanical stimuli with ferroelectric materials to the same effect. The crystal structures

such as the strontium and barium titanates are known to contain cations that can shuttle between a pair of lattice sites depending on the direction of an applied field. This phenomenon might find relevance in template technology as the atomic structure of a surface would be altered as these cations were moved closer to or farther from the surface in an applied field.

One drawback of using piezoelectric or ferroelectric systems for the work proposed here is that in both cases, the external stimuli would affect the entire system that it interacts with. Although their intensities can vary as a function of location, mechanical stresses and electric fields cannot be readily targeted to discrete positions across the continuum of a surface. Photoresponsive materials, however, are more susceptible to highly local events, as incident irradiation can readily be masked in locations where it is not desired. This permits increased system complexity, as the impact of the external stimulus can now be varied not only temporally, but spatially as well.

1.2 Additional Areas of Importance

The governing principles that make atomistic studies of colloid behavior important in advancing directed assembly techniques also pertain to other emerging materials technologies. One example of the direct impact of studies on titania surfaces ties in with recent work by Moorthy and coworkers, who used the photoresponsive properties of TiO₂ films to modulate electroosmotic flow in microfluidic channels [37]. The success of their work was rooted in the production of electrons at the surface of the films, whose presence altered the surface potential of the titania-coated walls of the channel. Control of flow in microfluidic channels through external means may have applications in drug delivery and discovery as well as in novel filtration techniques.

Oxide surfaces also serve as passive components in other forms of particle control. The electrophoretic manipulation of micron-sized silica particles, for example, has been studied between microelectrodes patterned onto sapphire surfaces [38-39]. Because the particles and microelectrodes are of similar lengthscales, interactions between the two essentially occur directly on the substrate surface. This was shown to be important, as Faradaic processes at both electrodes produced H⁺ and OH⁻ groups which locally altered the pH, and thus the surface potential, of the sapphire substrate. The result was a significant shift from repulsive to attractive

interactions between the suspended particles and the underlying substrate, which led to the adhesion of previously mobile particles onto the sapphire surface rather than the patterned electrodes. A continued bias across electrodes resulted in further electrolysis of water, which continued to shift interactions between surface and particles from repulsive to attractive at increasing distances away from the electrodes.

1.3 The Purpose of this Work

These studies aim to establish quantitative relationships between the structure and functionality of metal oxide surfaces in aqueous media. Specifically, the work relates the electro-osmotic properties of a crystalline surface to its structure, rather than just its chemistry. This approach bridges the crystal chemistry of a surface and the specific absorption and desorption of ions in an electrolyte. Such phenomena are at the heart of the development of the technologies outlined above, and their understanding is therefore critical. Thus far, only minimal work has been done in exploring the connections between the structures of inorganic surfaces and their aqueous chemistry behavior. Forging the links between a macroscopic property such as the isoelectric point of a material and the atomistic features of a crystal also creates closer connections between the nanoscale and the micron scale. Progress on this front in both alumina and titania oxide systems is presented, with thorough discussion of the relationship between surface structure and observed anisotropy.

The role that external stimuli can play in controlling the electro-osmotic behavior of systems is also explored. Model surfaces of single crystalline titanium dioxide are again used, with work focusing on the influence of ultraviolet irradiation (UV) on the behavior of these surfaces in solution. Capitalizing on the photoactivity of this system illustrates the viability of specifying surface functionality through external means, and may prove to be an effective approach to manipulating surfaces both spatially and temporally with applications in directed assembly, flow modulation, and flocculation control.

1.4 Organization of this Thesis

This author has attempted to organize the work detailed in these pages into a series of largely self-contained chapters, with each chapter featuring a smaller project that contributed to the whole of the thesis. The result is a document that might be regarded as a series of separate,

but interrelated academic papers. As such, each chapter contains its own discussion on the specific motivations for the work it contains, as well as its own descriptions of experimental procedure, presentation of results, and relevant discussion in terms of the larger body of academic work on the topic at hand. The most glaring of redundancies are eliminated by presenting in a single chapter both the theoretical framework of the phenomena studied here and the foundational principles of the most important experimental techniques. The thesis concludes with a chapter proposing a series of possible experiments to build on the work discussed here, and an appendix containing the major components of a Matlab analysis program written for the manipulation of AFM data.

1.4 References

- [1] A. Bachtold, P. Hadley, T. Nakanishi, and C. Dekker, "Logic circuits with carbon nanotube transistors." *Science* **294** (2001) 1317
- [2] W. Liang, M.P. Shores, M. Bockrath, J.R. Long, and H. Park, "Kondo resonance in a single-molecule transistor." *Nature* **417** (2002) 725
- [3] A.W. Ghosh, P.S. Damle, S. Datta, and A. Nitzan, "Molecular electronics: Theory and device prospects." *Mat. Res. Bull.* **29** (2004) 391
- [4] J.E.G.J. Wijnhoven and W.L. Vos, "Preparation of photonic crystals made by air spheres in titania." *Science* **281** (1998) 802
- [5] A. Imhof and D.J. Pine, "Ordered macroporous materials by emulsion templating." *Nature* **389** (1997) 948
- [6] Y.A. Vlasov, X.-Z. Bo, J.C. Sturm, and D.N. Norris, "On-chip natural assembly of silicon photonic bandgap crystals." *Nature* **414** (2001) 289
- [7] P.V. Braun and P. Wiltzius, "Microporous materials – Electrochemically grown photonic crystals." *Nature* **402** (1999) 603

- [8] O.D. Velev, and E.W. Kaler, "Structured porous materials via colloidal crystal templating: From inorganic oxides to metals." *Adv. Mater.* **12** (2000) 531
- [9] D.J. Norris and Y.A. Vlasov, "Chemical approaches to three dimensional semiconductor crystals." *Adv. Mater.* **13** (2001) 371
- [10] V.G. Solovyev, S.G. Romanov, C.M. Sotomayor Torres, M. Muller, R. Zental, N. Gaponik, A. Eychmuller, and A.L. Rogach, "Modification of the spontaneous emission of CdTe nanocrystals in TiO₂ inverted opals." *J. App. Phys.* **94** (2003) 1205
- [11] Y. Xia, B. Gates, Y. Yin, Y. Lu, "Monodispersed colloidal spheres: Old materials with new applications." *Adv. Mater.* **12** (2000) 693
- [12] P. Schall, I. Cohen, D.A. Weitz, and F. Spaepen, "Visualization of dislocation dynamics in colloidal crystals." *Science* **305** (2004) 1944
- [13] M.M. Tupper, Fabrication and Assembly of Micron-Scale Ceramic Components, *Doctoral Thesis*, M.I.T., 2004
- [14] H.J. Yeh and J.S. Smith, "Fluidic self-assembly for the integration of GaAs light-emitting diodes on Si substrates." *IEEE Photo Tech Lett* **6** (1994) 706
- [15] J.B. Hannon, A. Afzali, Ch. Klinke, and Ph. Avouris, "Selective placement of carbon nanotubes on metal-oxide surfaces." *Langmuir* **21** (2005) 8569
- [16] T. Teranishi, "Fabrication and electronic properties of gold nanoparticle superlattices." *Comptes Rendus Chimie* **6** (2003) 979
- [17] M. Piech, M.C. George, N.S. Bell, and P.V. Braun, "Patterned colloid assembly by grafted photochromic polymer layers." *Langmuir* **22** (2006) 1379
- [18] S. Noda, K. Tomoda, N. Yamamoto, and A. Chutinan, "Full three-dimensional photonic bandgap crystals at near-infrared wavelengths." *Science* **289** (2000) 604
- [19] W. Lee, A. Chan, M.A. Bevan, J.A. Lewis, and P.V. Braun, "Nanoparticle-mediated epitaxial assembly of colloidal crystals on patterned substrates." *Langmuir* **20** (2004) 5262
- [20] J.P. Hoogenboom, D. Derks, P. Vergeer, and A. van Blaaderen, "Stacking faults in colloidal crystals grown by sedimentation." *J Chem Phys* **117** (2002) 11320
- [21] F. Garcia-Santamaria, H.T. Miyazaki, A. Urquia, M. Ibisate, M. Belmonte, N. Shinya, F. Meseguer, and C. Lopez, "Nanorobotic manipulation of microspheres for on-chip diamond architectures." *Advanced Materials* **14** (2002) 1144
- [22] A. Kumar, H.A. Biebuyck, and G.M. Whitesides, "Patterning self-assembled monolayers: Applications in materials science." *Langmuir* **10** (1994) 1498

- [23] J.L. Wilbur, A. Kumar, H.A. Biebuyck, E. Kim, E., and G.M. Whitesides, "Microcontact printing of self-assembled monolayers: Applications in microfabrication." *Nanotechnology* **7** (1996) 452
- [24] P. Yang, T. Deng, D. Zhao, P. Feng, D. Pine, B.F. Chmelka, G.M. Whitesides, and G.D. Stucky, "Hierarchically ordered oxides." *Science* **282** (1998) 2244
- [25] K.M. Chen, X. Jiang, L.C. Kimerling, and P.T. Hammond, "Selective self-organization of colloids on patterned polyelectrolyte templates." *Langmuir* **16** 7825 (2000) 7825
- [26] I.W. Hamley, "Nanostructure fabrication using block copolymers." *Nanotechnology* **14** (2003) R39
- [27] M.F. Rubner in Multilayer Thin Films, Eds. G. Decher and J.B. Schlenoff (Wiley, Weinheim, 2003) 133-154
- [28] X. Jiang, H. Zheng, S. Gourdin, and P. Hammond, "Polymer-on-polymer stamping: Universal approaches to chemically patterned surfaces." *Langmuir* **18** (2002) 2607
- [29] M. Husemann, M. Morrison, D. Benoit, J. Frommer, C.M. Mate, W.D. Hinsberg, J.L. Hendrick, and C.J. Hawker, "Manipulation of surface properties by patterning of covalently bound polymer brushes." *J. Am. Chem. Soc.* **122** (2000) 1844
- [30] C.L. Brown, I.A. Aksay, D.A. Saville, M.H. Hecht, "Template-directed assembly of a de novo designed protein." *J. Am. Chem. Soc.* **124** (2002) 6846
- [31] M. Trau, N. Yao, E. Kim, Y. Xia, G.M. Whitesides, I.A. Aksay, "Microscopic patterning of oriented mesoscopic silica through guided growth." *Nature* **390** (1997) 674
- [32] M. Ogawa, "Nanoporous silica films containing aluminum and titanium." *Colloid Polym. Sci.* **281** (2003) 665
- [33] M. Heule, S. Vuillemin, L.J. Gauckler, "Powder-based ceramic meso- and microscale fabrication processes." *Adv. Mater.* **15** (2003) 1237
- [34] R.C. Hayward, D.A. Saville, and I.A. Aksay, "Electrophoretic assembly of colloidal crystals with optically tunable micropatterns." *Nature* **404** (2000) 56
- [35] E. Gizeli, M. Liley, C.R. Lowe, and H. Vogel, "Antibody binding to a functionalized supported lipid layer: A direct acoustic immunosensor." *Anal. Chem.* **63** (1997) 4808
- [36] K. Lange, F. Bender, A. Voigt, H. Gao, and M. Rapp, "A surface acoustic wave biosensor concept with low flow cell volumes for label-free detection." *Anal. Chem.* **75** (2003) 5561

- [37] J. Moorthy, C. Khoury, J.S. Moore and D.J. Beebe, "Active control of electroosmotic flow in microchannels using light." *Sensors Actuators B* **75** (2001) 223
- [38] R.J. Kershner, J.W. Bullard, and M.J. Cima, "The role of electrochemical reactions during electrophoretic particle deposition." *J Colloid Interf Sci* **278** (2004) 146
- [39] J.W. Bullard, R.J. Kershner, and M.J. Cima, "Scanning Probe Characterization of Localized pH Changes on a Sapphire Surface in the Presence of an Applied Field." *Proc Mat Res Soc* **782** (2003) A3.1.1

Chapter 2: Theoretical Background and Experimental Technique

2.1 Organization

This chapter of this thesis is intended to provide a theoretical framework within which subsequent experimental results are viewed and discussed. It provides a brief summary of the major elements of colloid science most germane to the work at hand, often referred to as DLVO theory, and begins with a discussion of the behavior of a generic dielectric surface in an electrolytic medium. This background is then focused on the specifics of behavior of metal oxide surfaces in aqueous salt solutions, and expanded to detail the models of interaction between two such interfaces in close proximity to each other.

The latter half of the chapter is dedicated to various means of quantifying the colloidal behavior of oxide surfaces, covering techniques for investigating both dispersed ceramic powders as well as flat substrates. Particular attention is paid to the methodology of making force spectroscopy measurements on a conventional atomic force microscope (AFM), as this technique serves as the primary investigative tool in the work on rutile surfaces detailed in ensuing chapters. A brief discussion of x-ray photoelectron spectroscopy (XPS) and Auger electron spectroscopy (AES) is also offered. These spectroscopic techniques were used as a secondary means of surface characterization, the results of which were correlated to direct measurements of the colloidal behavior of the oxide surfaces studied here.

2.2 Origins of the Electrical Double Layer: Gouy-Chapman Theory

Interactions between dielectric materials and aqueous solutions have long been known to result in the formation of a layer of electrical charge associated with the oxide surface, commonly referred to as the electrical double layer (EDL). EDL formation is the result of the attraction of solvated ions to the charged surface of the dielectric, which creates a localized imbalance of charge that trends towards the equilibrium condition at increased distance away from the surface (Figure 2.1). The double layer of charge necessarily results in some potential Ψ that is a function of the concentration of adsorbed species, which is described by a gradient away from the surface. $\Psi(x)$, by definition has the boundary conditions of $\Psi(x) = \Psi_0$ at $x=0$ and $\Psi(x) = 0$ at an infinite distance away from the surface [1-3].

2.2.1 The Poisson-Boltzmann Equation

The resultant imbalance of charge that defines EDL formation can be described as a function of the energy required to add an additional counterion, or solvated ion opposite in charge to that of the dielectric surface, from the solution to a given position away from the dielectric surface in the classic Boltzmann form:

$$\frac{n(x)}{n_o} = \exp\left(\frac{-\Delta G}{k_b T}\right) \quad (2.1)$$

where $n(x)$ is the concentration of counterions at some distance x away from the interface, n_o is the concentration of the same ion in bulk solution, and ΔG is the energy required to place an ion from the bulk solution to its new position at x . By definition of ΔG , the energy of the system is reduced by a redistribution of counterions if the work required to place a cation or anion at a given position is negative. It follows from equation 2.1 that when $\Delta G < 0$ for a particular ion at a particular position, the concentration of that ion at that position will be greater than its concentration in bulk solution, and vice versa. The energy required to move an ion to a given location can be defined as

$$\Delta G(x) = ze\Psi(x) \quad (2.2)$$

where z is the valence number of the ion, e is the charge of an electron, and Ψ is the electrical potential. The concentration of cations and anions at a given position can then be described by the expressions:

$$\frac{n_+}{n_o} = \exp\left(\frac{-ze\Psi(x)}{k_b T}\right) \quad \text{and} \quad \frac{n_-}{n_o} = \exp\left(\frac{-(-z)e\Psi(x)}{k_b T}\right) \quad (2.3)$$

where the terms n_+ and n_- denote the concentrations of cations and anions, respectively.

These Boltzmann energetics can be combined with Poisson's equation by first defining the charge density at some position away from the surface of interest as the product of the net ionic charge at that position, the valence of the ions, and the charge of an electron:

$$\rho = ze(n_+ - n_-) \quad (2.4)$$

This definition of ρ reveals the requirement in this derivation that the valence z is the same for both cationic and anionic species.

The one-dimensional Poisson equation states that the second spatial derivative of a potential is linearly related to the volume density of charge and the dielectric constant of the medium of interest, ϵ :

$$\frac{\partial^2 \Psi}{\partial x^2} = \frac{-\rho}{\epsilon} \quad (2.5)$$

Because ρ is itself a function of $\Psi(x)$ through equations 2.3 and 2.4, equations 2.4 and 2.5 can be combined as a differential equation known as the Poisson-Boltzmann equation. Replacing the terms n_+ and n_- with the exponentials from equation 2.4 and taking the second derivative with respect to position yields the relation

$$\frac{\partial^2 \Psi}{\partial x^2} = \frac{2ze n_o}{\epsilon} \sinh\left(\frac{ze\Psi(x)}{k_b T}\right) \quad (2.6)$$

commonly referred to as the nonlinear Poisson-Boltzmann equation. The physical construct of such a system requires that at the surface of the material of interest, the potential must be equal to the surface potential, Ψ_o , and that at infinite distance away from the surface (i.e., into the bulk solution, the potential must be zero. These boundary conditions yield the exact solution

$$\Psi(x) = \frac{2k_b T}{ze} \ln\left(\frac{1 + \gamma \exp[\kappa x]}{1 - \gamma \exp[\kappa x]}\right) \quad (2.7)$$

where γ and κ are defined as

$$\gamma \equiv \frac{\exp\left(\frac{ze\Psi_o}{k_b T}\right) - 1}{\exp\left(\frac{ze\Psi_o}{k_b T}\right) + 1} \quad \text{and} \quad \kappa \equiv \sqrt{\frac{2e^2 n_o z^2}{\epsilon k_b T}} \quad (2.8, 2.9)$$

This cumbersome equation is greatly simplified by using the convention that for small values of some variable t , $\sinh(t)$ is approximated as t . Therefore, for the condition that $ze\Psi(x) \ll k_b T$,

$$\frac{\partial^2 \Psi}{\partial x^2} = \frac{2ze n_o}{\epsilon} \left(\frac{ze \Psi(x)}{k_b T} \right) \Rightarrow \frac{2e^2 n_o z^2}{\epsilon k_b T} \Psi(x). \quad (2.10)$$

The definition of κ simplifies this relation further to

$$\frac{\partial^2 \Psi}{\partial x^2} = \kappa^2 \Psi(x), \quad (2.11)$$

which has the solution

$$\Psi(x) = \Psi_o \exp(-\kappa x). \quad (2.12)$$

This relationship is known to as the linear Poisson-Boltzmann equation, and shows the exponential nature of the decay of an electrostatic potential away from a dielectric surface in solution.

The Poisson-Boltzmann treatment of the EDL can also be used to describe the concentration of surface charge in terms of electrical potential. Recalling equation 2.5, the surface charge density, σ_o , can be related to the charge everywhere else in the liquid (i.e., far away from the interface, by charge balance. The result is that σ_o is defined as the negative of the integral of the solution charge density as a function of distance away from the surface:

$$\sigma_o = - \int_{x=0}^{\infty} \rho dx \quad (2.13)$$

Replacing ρ using the Poisson equation, this integral becomes

$$\sigma_o = \epsilon \int_{x=0}^{\infty} \frac{\partial^2 \Psi}{\partial x^2} dx \Rightarrow \epsilon \frac{\partial \Psi}{\partial x} \Big|_{x=\infty} - \epsilon \frac{\partial \Psi}{\partial x} \Big|_{x=0} \quad (2.14)$$

The first term of the solution approaches zero at infinite distance away from the interface (bulk conditions are met), leaving only the second term to define the surface charge density. The relationship between surface potential and distance from the interface (equation 2.12) can be used to solve the spatial derivative on the right hand side of equation 2.14, yielding the relation

$$\sigma_o = \epsilon \kappa \Psi_o, \quad \text{or} \quad \frac{\sigma_o}{\Psi_o} = \epsilon \kappa. \quad (2.15)$$

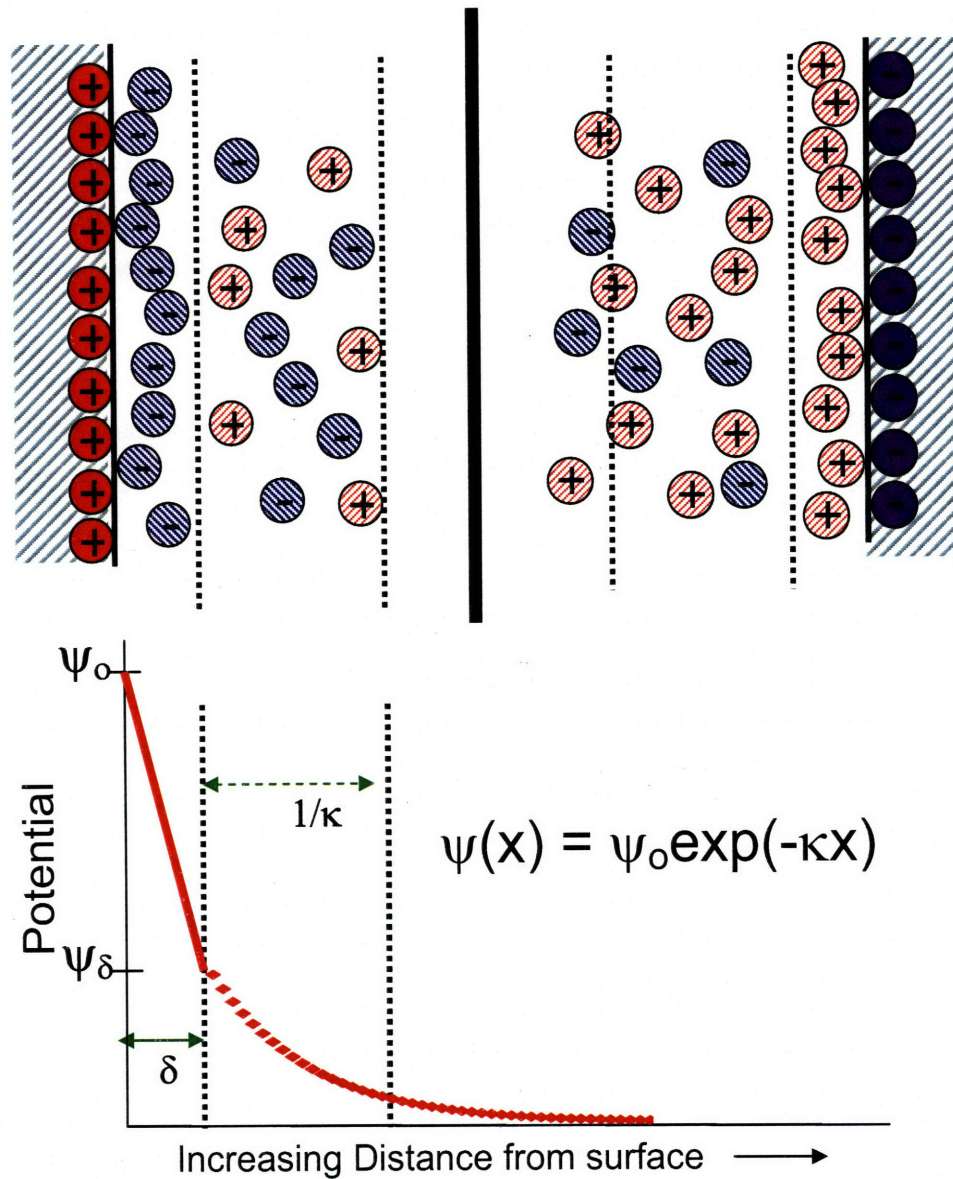


Figure 2.1. Top: Schematic diagram of the formation of an electrical double layer on surfaces of positive (red circles, left-hand side) and negative (blue circles, right-hand side) charge. Ions of charge opposite in sign to that of the surface are tightly bound in the narrow Stern layer, while a more loosely bound layer of charge is shown in the distance of one Debye length away. Bottom: The drop in surface potential is shown as a function of distance away from the surface of the dielectric interface. Potential decreases linearly across the Stern layer as it would in a generic capacitor; the decay through the Debye layer and into the bulk solution, however, follows the behavior described by the Poisson-Boltzmann equation.

The second formulation of this relationship shows that as κ increases with ionic strength, the amount of charge stored in the EDL per unit potential must also increase, as the dielectric constant of aqueous solutions has been shown to retain its bulk value even in nanometer thick films [4]. Equation 2.15 does not indicate, however, whether surface charge density increases or surface potential decreases, and different systems are known to behave in different ways.

2.3 Stern and Debye Layer Components of the EDL

The Poisson-Boltzmann equation predicts an exponential decay of surface potential as a function of increasing distance away from the dielectric interface, but makes no distinction between ions positioned immediately at the dielectric interface and those slightly farther away, but still close enough to represent deviation from bulk solution conditions. The Poisson-Boltzmann derivation, as shown, considers only electrostatic interactions between the dielectric surface and the electrolytic solution. It ignores any contribution to the energetics of the system associated with the direct adsorption of solvated ions to the surface. Ions that interact with the surface in this manner are known to be bound more tightly at the interface in comparison with ions whose presence is dictated only by the electrostatic model outlined above. As a result, the EDL model must be modified to incorporate this tightly-bound layer of adsorbed counterions, commonly referred to as the Stern layer.

The addition of the Stern layer to the Gouy-Chapman model of the EDL results in the delineation of two distinct components of the EDL: The relatively narrow region of tightly-bound, oppositely-charged counterions in the Stern layer, and the region of charge whose potential and concentration are dictated principally by electrostatic interactions, referred to as the diffuse or Debye layer. The thickness of the Stern layer remains essentially constant for a given system of surface material and solution chemistry, as it is defined as a layer of counterions tightly bound to the dielectric surface. Typical thicknesses of the Stern layer are therefore on the order of the radii of adsorbing species, or 1-3 Å. The Debye layer, on the other hand, is a function of the ionic strength of the solution, and is defined by its inverse as:

$$\kappa = \sqrt{\frac{e^2 \sum_i n_i z_i^2}{\epsilon k_b T}} \quad (2.16)$$

A comparison of 2.9 to 2.13 shows that the above definition of the inverse of the Debye layer is only a more generalized form of the constant κ used to simplify the description of the nonlinear Poisson-Boltzmann equation, which assumed a single pair of ionic species of identical valence.

The differences in the characteristics of the Stern and Debye layers is evident in the plot of surface potential as a function of distance from the surface shown in the bottom portion of Figure 2.1. The tightly-bound Stern layer is shown to influence surface potential only over a distance on the order of the lengthscale of the ionic radii of adsorbing species, but the potential drop across this layer is rapid and linear. The diffuse portion of the EDL, on the other hand, obeys the Poission-Boltzmann relation, with an exponential decay in surface potential away from the surface. With no well-defined boundary to this layer, the Debye layer provides a characteristic length to define the limits of the EDL.

For a 1 mM solution where the valences of cationic and anionic species are equal, the Debye length $1/\kappa$ is approximately 10 nm. It is worth noting that solutions ranging in concentration from 0.1 mM to 100 mM result in values of $1/\kappa$ on the nanometer lengthscale, allowing for the approximation of microscale particles as flat plates. Moreover, the size of the Debye layer provides information about the lengthscales over which dielectric surfaces will interact in their suspending media, because they provide a benchmark for the distance over which the surface potential deviates strongly enough from bulk to interact with other surfaces with any significant force. Typically, the surface potential approaches zero three to five Debye lengths away from the surface of interest, a rule of thumb that will be more evident after the derivation followed in section 2.4.1.

2.4 The Double Layer and Forces Between Suspended Bodies

The introduction of one colloidal surface into the vicinity of another results in the interaction between the EDLs of the two surfaces. This leads to an exertion of electrostatic forces of each body on the other, the intensities of which are magnified as separation distances between the two bodies decreases. Interactions between such surfaces are most commonly treated in terms of overlapping surface potentials, with forces between them taken by differentiating those expressions.

Derivations of interactions between EDLs fall into four fundamental categories: Interactions between identical surfaces of constant potential, identical surfaces of constant charge,

dissimilar surfaces of constant potential, and dissimilar surfaces of constant charge. Fundamental assumptions for the derivation of the interaction between two identical surfaces of constant potential will be reviewed here as a means of exploring various events important in the interactions between the surfaces of two suspended bodies; the treatment in these pages is based largely on refs [1-2]. The results of more complex conditions are given, but not derived.

2.4.1 Interactions Between Identical Flat Surfaces of Constant Potential

An understanding of the forces arising from the interactions between the EDLs of separate surfaces can be viewed in terms of changes in the free energies of the EDLs from when the two surfaces are far apart to when they are in close proximity to each other. The free energy f of a single, non-interacting EDL can be shown by relating the chemical energy of an adsorbing species to the chemical energy of the same species in bulk solution as:

$$f = -\frac{1}{2}\sigma_o\Psi_o \quad (2.17)$$

Consider a pair of flat, identical surfaces of constant potential separated by a distance L , with the parameter x defined such that $x = 0$ at the midway point between the two surfaces. Because both surfaces are identical, we have the boundary condition that the potential at both $x = +L/2$ and $x = -L/2$ – that is, at the two surfaces of interest – will be the same, and will be defined as Ψ_o . Because the system is symmetric, changes in the potential as a function of x will be symmetric around the midway point. Therefore, $\frac{\partial\Psi}{\partial x} = 0$ at $x = 0$. Using the linearized Poisson-Boltzmann

equation, the relation is solved by multiplying both sides of equation 2.11 by the term $2\frac{\partial\Psi}{\partial x}$,

which by identity ultimately yields the relation:

$$\frac{d}{dx}\left(\frac{\partial\Psi}{\partial x}\right)^2 = 2\kappa^2\Psi\left(\frac{\partial\Psi}{\partial x}\right) \quad (2.18)$$

Both sides of eq. 2.18 are integrated, and multiplying by $-\varepsilon/2$ and subtracting the x -dependent right hand integrand from the left hand integrand yields results in the equation

$$\frac{\varepsilon}{2}\kappa^2\Psi^2 - \frac{\varepsilon}{2}\left(\frac{\partial\Psi}{\partial x}\right)^2 = P_m \quad (2.19)$$

where the term P_m emerges from an integration constant after 2.18. P_m is dependant only on the separation distance L , and at $x = 0$, where it has been established that the spatial derivative of the potential is zero,

$$\frac{\varepsilon}{2}\kappa^2\Psi^2 = P_m \quad (\text{at } x = 0). \quad (2.20)$$

This definition of P_m gives way to the relation

$$\frac{\varepsilon}{2}\kappa^2\Psi^2 - \frac{\varepsilon}{2}\left(\frac{\partial\Psi}{\partial x}\right)^2 = \frac{\varepsilon}{2}\kappa^2\Psi_m^2 \quad (2.21)$$

where Ψ_m is defined as the potential midway between the two planes. The dependence of Ψ_m solely on L can be shown by rewriting equation 2.21 to define the spatial derivative of Ψ in terms of the square root of the difference between Ψ^2 and Ψ_m^2 , and the introduction of a value ω defined as the inverse hyperbolic cosine of Ψ/Ψ_m . It should be noted that the spatial derivative of Ψ can now be defined as $\Psi_m\sinh(\omega)$. It can be shown from these relationships and a few substitutions that

$$\sinh \omega \frac{d\omega}{dx} = \kappa\sqrt{\cosh^2 \omega - 1} \quad (2.22)$$

The identity $\sqrt{\cosh^2 \omega - 1}$ is also $\sinh(\omega)$, and therefore the spatial derivative of ω is shown to be equal to the Debye layer, κ . Integrating to solve for ω can be achieved by remembering the boundary condition that at $x = \pm L/2$, ω becomes the hyperbolic cosine of Ψ_o/Ψ_m . This is important in determining the integration constant, which allows for the definition of ω in other terms:

$$\omega = \kappa\left(x - \frac{L}{2}\right) + \cosh^{-1}\left(\frac{\Psi_o}{\Psi_m}\right) \quad (2.23)$$

Remembering the original definition of w in terms of $\Psi(x)$ and Ψ_m yields an expression for $\Psi(x)$ which can be defined in terms of Ψ_m , Ψ_o , κ , x , and L . Ψ_m , in turn, can be determined by setting x to 0, which results in the relation

$$\frac{\Psi_m}{\Psi_o} = \frac{1}{\cosh\left(\frac{\kappa L}{2}\right)}. \quad (2.24)$$

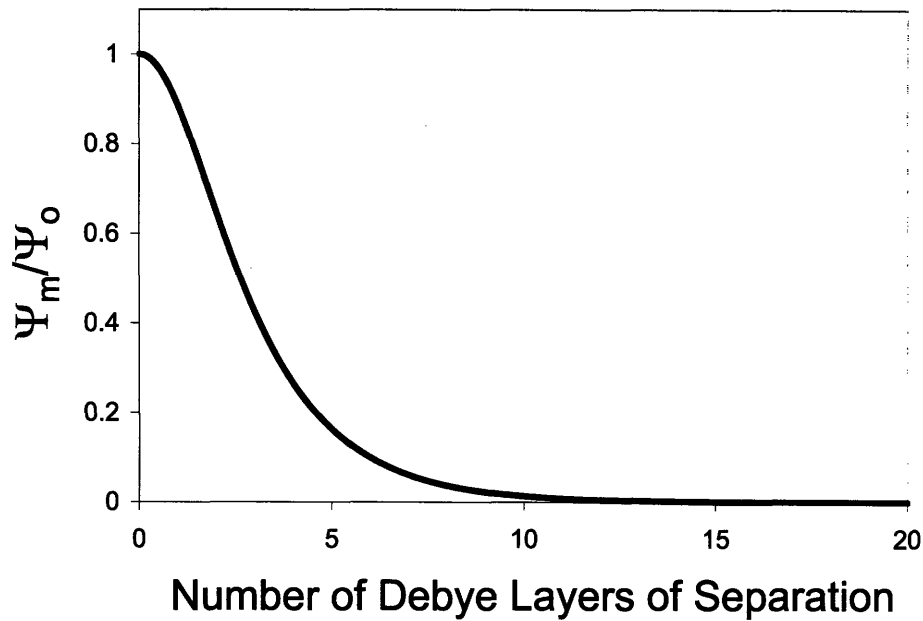


Figure 2.2. A plot of the midplane potential, Ψ_m , as a function of plate separation, defined in terms of number of Debye layers, as described by equation 2.24. The relation holds only for the special case of infinitely large surfaces of constant potential (Ψ_o), but shows the dramatic decline in Ψ_m as a function of separation distance.

The relationship between mid-plane potential and plate separation is shown graphically in Figure 2.2. It is evident that Ψ_m drops significantly after only four or five Debye layers of separation, and vanishes almost completely at distances of approximately ten Debye lengths.

The surface charge density, σ_o , can be determined as it was before, defining it as the negative of the integral of the volume density of all charges in bulk solution. Symmetry arguments for the special case derived here require only the integration x between the mid-plane and one surface. The result is identical to Eq 2.14, with the only difference being the limits of integration. This relation can be combined with a relationship implicit from equation 2.21 to show the relationship between surface charge density and mid-plane potential:

$$\frac{\sigma_o}{\epsilon\kappa\Psi_o} = \sqrt{1 - \left(\frac{\Psi_m}{\Psi_o}\right)^2}. \quad (2.25)$$

where the relationship between mid-plane and surface potentials is shown in equation 2.24. The relationship shown in equation 2.25 is displayed graphically in Figure 2.2. One implication of

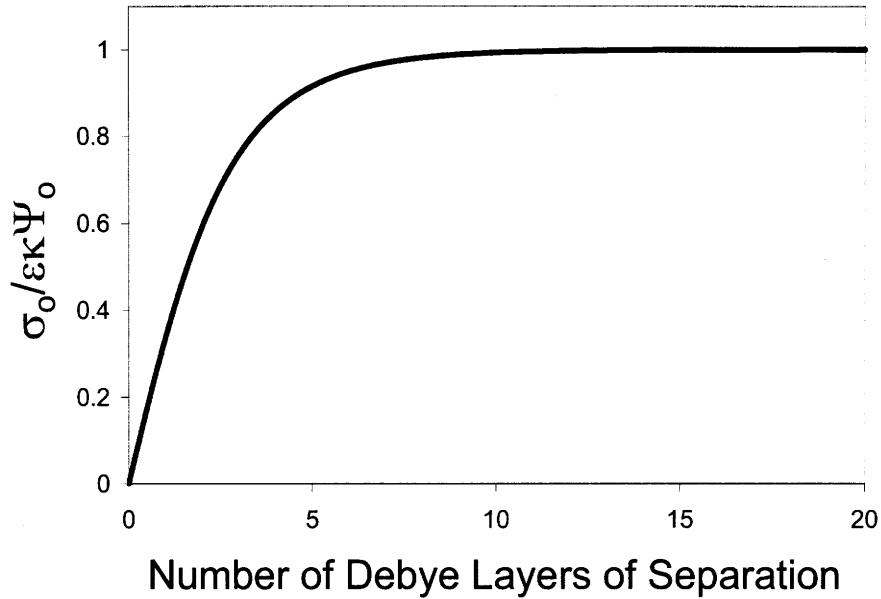


Figure 2.3. A plot of surface charge as a function of the separation distance between two flat, infinite plates of constant surface potential. The sharp decline of surface charge at very small separation distances is required for surfaces to maintain their potential at close proximity.

equation 2.25 is that as plate separations decrease, the charge present on both surfaces approaches zero. This result makes sense in the context of surfaces of constant potential, as a given potential can only be maintained between two plates as their separation is varied if density of charge is altered. One corollary to this observation is that for a real surface to closely approximate the behavior of an idealized surface of constant potential, its surface charges must exhibit a relatively high degree of mobility.

Using these relations, the Gibbs free energy of a pair of charged plates can be derived, which in turn provides an expression for the separation potential, V_R , of two surfaces of constant potential. Having defined the free energy of an individual, charged dielectric surface in equation 2.17, the free energy of two plates of interest will be twice that value at infinite separation. Consider now the energy required to move two such plates to some separation L , attributing the change in energy to the discharge of the EDL of the two plates and assuming the surface potential to be constant:

$$\Delta G = \Psi_o \left(\sigma_o \Big|_{x=\infty} - \sigma_o \Big|_{x=L} \right) \quad (2.26)$$

DG is always positive, because, as seen in Figure 2.3, the surface charge density at some small separation distance L is always smaller than the surface charge density at infinite separation. This relationship can be recast in terms of surface and mid-plane potentials, expressed as

$$\Delta G = \Psi_o \left(\epsilon \kappa \Psi_o - \epsilon \kappa \sqrt{\Psi_o^2 - \Psi_m^2} \right). \quad (2.27)$$

This energy is frequently described as the reduced separation potential, V_R , and equation 2.27 can be used to express V_R as a function of separation distance:

$$\frac{V_R}{\epsilon \kappa \Psi_o^2} = 1 - \tanh\left(\frac{\kappa L}{2}\right) \quad (2.28)$$

The behavior of equation 2.28 is shown in Figure 2.4. Note that for surfaces of constant potential, there still exists a finite value of V_R at $L = 0$, indicating that there is a finite amount of energy required to bring a pair of plates into contact with each other. Moreover, the reduced potential essentially vanishes at separation distances on the order of five Debye layers. This suggests a practical limit of the lengthscale over which interactions between suspended bodies can be expected to occur, which is determined by the solution characteristics that define the characteristic Debye length.

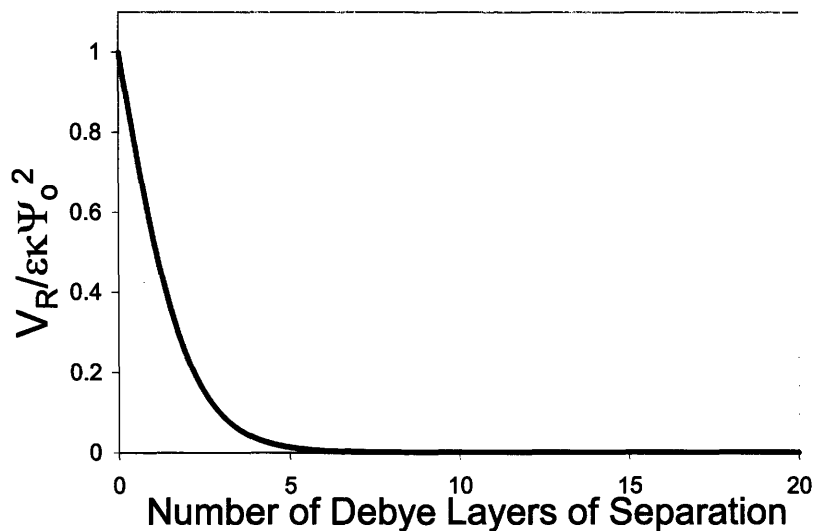


Figure 2.4. Normalized plot of reduced potential V_R , as a function of separation distance between two flat surfaces of constant Ψ_o . V_R is shown to reach a finite value at zero separation distance, as well as a near-zero value at separation distances on the order of five Debye lengths.

2.4.2 Interactions Between Different Surfaces of Constant Potential or Charge

As mentioned before, the interaction potentials of more complex systems have also been derived. Their development remains rooted in the Poisson-Boltzmann description of EDL formation and is based on considerations of the energetics and boundary conditions akin to those involved in the preceding work. A most general description of interaction energy is provided in [5], which combines derivations of others [6-8] to describe interaction potential as

$$\frac{V_R}{\epsilon\kappa\Psi_o^2} = \mp(1 - \coth \bar{h})(\bar{\Psi}_1^2 - \bar{\Psi}_2^2) + \left(\frac{2\bar{\Psi}_1\bar{\Psi}_2}{\sinh \bar{h}} \right) \quad (2.29)$$

where the negative sign preceding the *coth* term pertains to two surfaces of constant charge and the positive sign corresponds to two surfaces of constant potential. It should be made clear that in equation 2.29, the Ψ terms denote the potential Ψ_o at the surface for two different materials, indicated by the subscripts 1 and 2, and are not dependent upon x . It can be further shown from this generic equation that for small separations, systems modeled as having surfaces of constant charge exhibit infinite repulsion, whereas those of constant potential are shown to attract.

2.4.3 The Derjaguin Approximation

The preceding derivation for the interaction parameters of two plates demonstrates the general approach of considering such behavior, but it is limited in the fact that it was developed for the special case of two flat plates. Real systems frequently involve the interaction of suspended particles which are commonly spherical in nature. Modeling the interactions between two such spheres or between a single sphere and a flat plate is critical to understanding the dynamics of actual suspensions. Defining the forces of interaction between spheres or spheres and plates is achieved by way of a method first developed by Derjaguin [9]. Rather than calculate separation distance between spherical surfaces as continuous function accounting for the curvature of the surfaces, Derjaguin showed that any surface with a radius significantly larger than its characteristic Debye length could instead be described as a stack of flat plates of changing cross-sectional area. The energy of interaction U between two surfaces of arbitrary shape separated by some distance D could therefore be related to the energy per unit area U_A of two flat surfaces separated by some distance x . This is shown schematically in Figure 2.5, as well as mathematically in the form

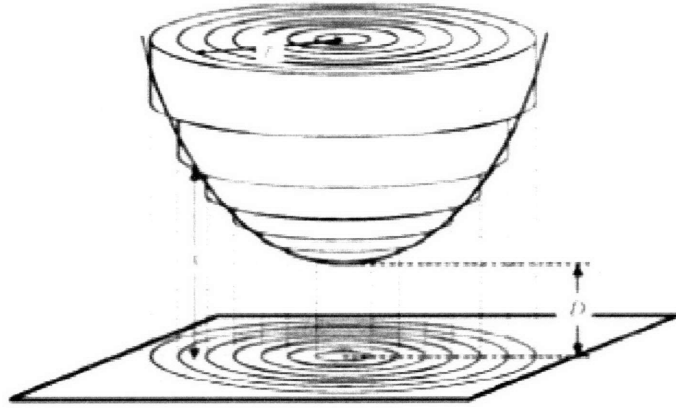


Figure 2.5. A schematic of Derjaguin's approach to the interaction potential between a sphere and a flat plane. The value D represents the actual separation distance between the top and bottom bodies, whereas x is a function of the cross-sectional area of each layer. Taken from [10].

$$U(D) = \int U_A(x) dA \quad (2.30)$$

where dA represents the variance in cross-sectional area of the layered flat surfaces that approximate the actual, irregular surface. The specific case for the interaction between a flat surface and a spherical particle of some known radius R benefits from setting $dA = 2\pi r dr$, where r is the radius of each small slab used to approximate the overall shape of the sphere. This yields the relationship between the radius of each slab and its distance from the surface relative to the defined separation distance D of the sphere and surface

$$x = D + R - \sqrt{R^2 - r^2} , \quad (2.31)$$

which, when differentiated with respect to r , reveals that

$$r dr = dx \sqrt{R^2 - r^2} . \quad (2.32)$$

Furthermore, equation 2.30 can be combined with equation 2.29 to describe the interaction potential between two spheres of any size (Adamczyk):

$$V_R = \varepsilon \kappa \frac{R_1 R_2}{R_1 + R_2} \left[\mp (\bar{\Psi}_1^2 - \bar{\Psi}_2^2) \ln(1 - \exp(-2\kappa h_m)) + 2\bar{\Psi}_1 \bar{\Psi}_2 \ln \left(\frac{1 + \exp(\kappa h_m)}{1 - \exp(\kappa h_m)} \right) \right] \quad (2.33)$$

with the upper minus and lower plus signs used for the cases of surfaces of constant charge and potential, respectively. Equation 2.33 can be differentiated to yield an expression for the force of interaction between two particles. Moreover, the term $\frac{R_1 R_2}{R_1 + R_2}$, which defines a relationship

between the radii of the interacting species, can be shown to reduce to a single R for the case of a sphere interacting with a flat plate (infinite radius).

2.4.4 The Linear Superposition Approximation

The discussion of the interaction of the model surfaces detailed above is effective in demonstrating the origins and variations of interactions in different colloidal systems. However, they suffer from the reality that a limited number of surfaces of interest actually behave as either surfaces of constant potential or surfaces of constant charge. Specifically, most dielectric interfaces exhibit behavior that falls somewhere between the two extrema, and therefore do not conform to the proposed models. One alternative approach to solving the Poisson-Boltzmann relation is commonly known as the linear superposition approximation, or LSA. The essence of LSA is that rather than accounting for interactions of surfaces across all separation distances, the Poisson-Boltzmann relation for two interacting bodies can instead be solved by superimposing the solutions for each individual surface at infinite separation [11]. The approach yields the relation for interaction potential [12]

$$V_R = 64\pi\epsilon R \left(\frac{kT}{z_i e} \right)^2 \gamma_1 \gamma_2 \exp(-\kappa x) \quad (2.34)$$

with the definition

$$\gamma_i = \tanh \left(\frac{z_j e \Psi_{o,i}}{4kT} \right) \quad (2.35)$$

The potential can be differentiated to produce an expression for the force of interaction between a sphere and a flat plate, shown below to be normalized for the radius of the sphere.

$$\frac{F}{R} = \kappa 64\pi\epsilon \left(\frac{kT}{z_i e} \right)^2 \gamma_1 \gamma_2 \exp(-\kappa x) \quad (2.36)$$

The LSA model has been shown to yield good fits to experimental data in some force-distance measurements [13], which will be discussed in greater detail below.

2.5 Probing the Double Layer: Zeta Potential

Probing the characteristics of the double layer of a material is an important means of understanding the behavior of a colloidal system. As such, several techniques have been developed to characterize the double layers of both colloidal particles and flat surfaces. Perhaps

the most common approach to measure the double layer potential of suspended particulate media is the determination of the electrophoretic mobility of a system.

One consequence of the formation of the charged double on a colloidal surface is that such layers, and by extension, the particles on which they form, are responsive to electric fields. The manipulation of such particles with applied fields is commonly known as electrophoresis, and the electrophoretic mobility of suspended particles, μ_E , is linearly related to the zeta potential of the particle, ζ_p [14]:

$$\mu_E = \frac{\epsilon_f \zeta_p}{\eta} \quad 2.37$$

where ϵ_f is the dielectric constant of the suspending medium, ζ_p is the zeta potential of the surface of interest, and η is the viscosity of the suspension.

The electrophoretic velocity of a suspended particle is the product of its mobility and the applied field, as described by

$$v_{\text{electrophoretic}} = \mu_E E = \frac{\epsilon_f \zeta_p E}{\eta} \quad 2.38$$

Equation 2.38 provides a direct relationship between a readily measurable quantity, particle velocity, and a physical property of interest, ζ . Early measurement techniques typically involved the direct observation of the motion of suspended media in the presence of an applied field; investigators would track the time required for a particle to travel a given distance for a given field strength, and knowing ϵ and η , would directly measure ζ . A more modern technique tracks the phase shift of a laser signal passed through the suspension of interest. This method, commonly referred to as phase analysis light scattering (PALS) correlates the phase shift of the laser signal to the velocity of the particles in the suspension through which it passes, and was the method employed in all zeta potential measurements of powders described in these pages.

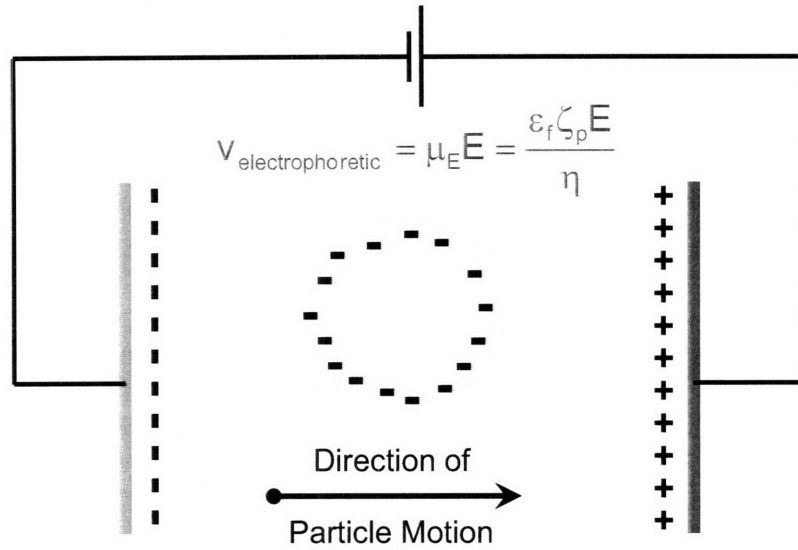


Figure 2.6. A schematic diagram of the electrophoretic mobility of a charged particle in solution. The electric double layer responds to the external stimulus of an applied field, and moves towards the pole of opposite sign. Measuring the velocity of a particle during this process provides a means of quantifying the zeta potential, ζ , of the material.

The zeta potential of flat plates, on the other hand, is typically measured using the streaming potential technique. This approach requires the flow of solution between parallel plates of the surfaces of interest, which effectively shears ions from the double layer. The result is a net accumulation of double-layer ions at the outflow end of the fluid channel, which is quantified in the form of a drop in electrical potential across the channel. ζ is related to this drop by the Helmholtz-Smoluchowski equation [14]:

$$\zeta = \frac{\Delta U_s}{\Delta P} \frac{\eta}{\epsilon \epsilon_0} \frac{L}{A} \frac{1}{R} \quad 2.39$$

Where ΔU_s is the potential drop across the flow channel, ΔP is the drop in pressure, L and A are the length and cross-sectional area of the fluid channel, and R is the electrical resistance of the suspending medium in the channel. The relationship between ζ and ΔU_s is further simplified when the resistance of the solution is high enough that the influence of surface conductivity can be ignored. This condition is typically met in aqueous systems at salt concentrations greater than 1×10^{-3} M, and results in the Fairbrother-Mastin approximation for the ratio L/A :

$$\frac{L}{A} = \kappa R, \quad 2.40$$

where here κ is defined as the conductivity of the solution. Substituting this approximation into equation 2.39 describes ζ as

$$\zeta = \frac{\Delta U_s}{\Delta P} \frac{\mu}{\epsilon \epsilon_0} \kappa. \quad 2.41$$

The electro-osmotic behavior of various orientations of sapphire surfaces summarized both below and in other publications [15-16] utilized this relationship to quantify ζ . One drawback of streaming potential measurements, however, is that commercially available systems typically require the use of relatively large samples to make accurate measurements. A handful of alternative designs have been used, however, to make measurements on smaller surfaces [17-18]. Nevertheless, for the analysis of crystal systems that are not available in large surface areas, alternative techniques are desirable.

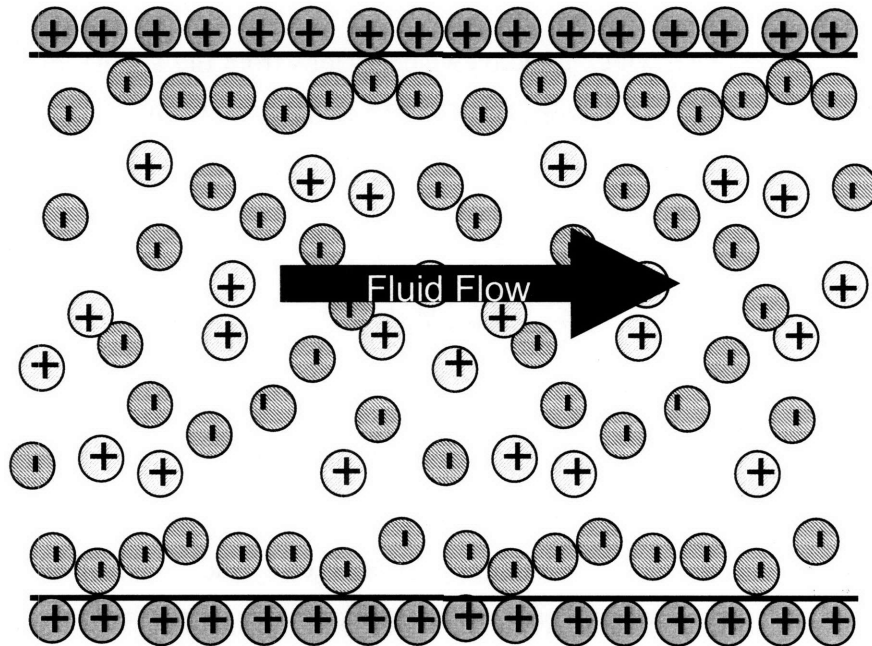
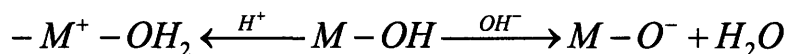


Figure 2.7: Schematic diagram of the streaming potential technique for determining the zeta potential of a flat surface. The flow of fluid between parallel plates results in a shearing of ions from the double layer, which is characterized by a drop in potential across the flow channel. The ratio of this potential drop to a drop in pressure across the same distance is linearly related to ζ by physical parameters of the system.

2.6 Double Layer Formation on Oxide Surfaces: Assumptions and MUSIC Model

This double layer forms as a result of the attraction of solvated ions to the oxide surface, which is charged by the interaction of hydrogen or hydroxyl groups with the surface:



The relationships depicted above assume that the surface of the metal oxide is hydroxylated, taking on the generic form M-OH [1]. Infrared spectroscopy and other surface analysis techniques have shown that such hydroxyl groups are indeed native to the surfaces of numerous metal oxide systems, including titania [19-23] and alumina [24-25].

The adsorption of hydroxyl groups (or, alternatively, H^+ ions) on a metal oxide surface is a function of the specific affinity of a given surface site for such an event. This is largely determined by the electron affinity (or positivity) of a particular site, which is determined by factors such as coordination number and bond length with neighboring atoms. This idea was originally formalized by Hiemstra and co-workers [26-27] as the MUlti Site Complexation (MUSIC) model, and postulates that the energetics of proton or hydroxyl adsorption on a given surface vary locally with atomic landscape.

Predictions by the MUSIC model are readily testable, as the strength of bonds between an oxide surface and solvated protons or hydroxyl groups is intimately related to measurable material properties. This relationship between theory and experiment is perhaps most commonly explored in terms of the isoelectric point of a surface. Surfaces adsorbing an excess quantity of hydroxyl groups will exhibit a negative surface potential, which can be measured in ζ . Considering the pair of equilibrium reactions above, a surface that forms strong bonds with solvated hydroxyl groups will require a greater concentration of solvated protons to drive the equilibrium to a position favorable to proton adsorption, which would result in a positive surface potential. This proton concentration is, by definition, the pH of the solution, and surfaces that strongly adsorb hydroxyl groups will therefore undergo a shift from negative to positive surface potential at a lower pH than surfaces that weakly adsorb hydroxyl groups.

The MUSIC model suggests that an increased affinity for hydroxyl adsorption is directly related to the electronic and atomic structure of a given adsorption site. Hydroxyl groups are negatively charged; therefore, sites that have a high electron affinity will be locations of

preferred adsorption. An exemplary site for such adsorption on a metal oxide surface would be a cationic position with a low coordination number, indicating that a relatively small amount of the site's cationic character is compensated by neighboring oxygen atoms in the crystal lattice. Electron-rich positions, on the other hand, are optimal sites for proton adsorption, and surfaces with an abundance of such sites would be expected to have higher isoelectric points than surfaces with an abundance of hydroxyl adsorption sites.

The implications of the model can be expanded to predict variations in the isoelectric point of a material as a function of crystallographic orientation. The exposure of different crystal planes to solution results in different interactions between solvated species and metal oxide adsorption sites. Variant surface structure leads to differences in the density and coordination number of both cationic and anionic positions, which leads to changes in the energetics of species adsorption.

2.7 Force Distance Spectroscopy

2.7.1 General Overview

Interactions between overlapping double layers of distinct surfaces are known to result in either repulsive or attractive forces, as previously discussed. This phenomenon can also be used as a means of probing the double layer behavior of a given material through a technique commonly referred to as force spectroscopy. Current force spectroscopy techniques typically utilize a conventional atomic force microscope (AFM), which was initially developed for nanoscale, topographic imaging [28]. Operation of an AFM in imaging mode involves using a piezoelectric stack to raster a sharp tip attached to a flexible cantilever across the surface of interest. As the tip interacts with topographic features of the surface, the cantilever is deflected from its equilibrium position. This deflection is measured by a photodiode that tracks the position of a laser focused on the cantilever probe. A feedback loop determines the amount which the piezo stack needs to be raised or lowered in order to restore the equilibrium flexure of the cantilever, which is directly related to the height of the surface. This can be controlled with an extremely high degree of sensitivity, and observations of surface features only a few angstroms in size are not uncommon [29-31]. A topographic image of the surface is therefore produced by plotting either the deflection of the cantilever or the height changes in the piezo stack as a function of position on the surface.

Force spectroscopy measurements made with an AFM operate on the same principle, but the tip is instead fixed above a given position on the surface of interest. The piezoelectric stack then lowers the probe tip towards the surface, and the deflection of the cantilever is measured as a function of vertical separation distance from the surface, rather than as a function of lateral position. Repeated measurements are made by raising and lowering the probe tip at the same position with a controlled frequency. This provides the opportunity not only to measure interaction forces between the tip and surface during the approach of the former, but to also study the forces involved in pulling the tip away from the surface and back into a non-interacting position. Data gathered during approach portions of the measurement allow for the study of phenomena such as electrostatic and van der Waals interactions, whereas the retraction of the tip from the surface provides information on and adhesion forces that may be present.

Conversion of cantilever deflection data to values of interaction force is achieved by using the spring constant of the cantilever, k_c in conjunction with Hooke's Law. This yields a plot of force as a function of separation distance between tip and surface. Typical values of k_c for commonly used, commercially available cantilevers generally vary between 0.06 N/m and 0.58 N/m, depending on the length and width of the cantilever. The use of cantilevers with a smaller k_c results in larger deflections for a given force, and therefore a larger signal at the photodiode. Cantilevers with larger values of k_c , on the other hand, do not vibrate as much when suspended freely (i.e., non-interacting) above the surface of interest, providing a flatter baseline with less noise. The sensitive capabilities of force-distance measurements is evident when one considers that if a cantilever having a spring constant of 0.06 N/m deflects an easily-detectable one nanometer, this corresponds to an interaction force of 60 pN.

Force spectroscopy methods are an attractive means of interaction analysis because they offer the versatility of studying the interactions between almost any two surfaces in any number of media. Probe tips, which are commonly made from silicon or silicon nitride, can be modified to be coated with specific functional chemistries of interest. This allows for the measurement between well-defined chemical groups attached to the probe tip and the surface of interest on which the measurements are performed. One of most pervasive techniques is to coat the probe tip with a layer of gold and attach a self-assembling functional group to the gold surface. Thiolated gold surfaces are perhaps the best example of this, as their assembly on gold surfaces is well-known and results in repeatable, predictable densities of adsorbed species [32-33]. Probe

surfaces containing other organic terminations such as carboxyl, methyl, and amino groups are also known [34-36]. Coating a probe tip with a specific molecule allows for the careful control of the surface characteristics of the probe surface, such as charge density (and sign), hydrophilicity or hydrophobicity, or some known interaction energy with another surface. The high control of such properties on the tip surface is critical to making careful measurements of the behavior of the surface of interest. Knowing the charge density of functional groups on the probe tip, for example, enables one to reliably measure the charge density of a specific surface [37-38].

AFM cantilevers can also be fabricated without any probe tip at all, leaving a large space on the cantilever surface to instead place a specific particle. These probes, known as colloidal probes, were first introduced in the early 1990s by researchers who used micron-sized silica spheres as their probe of choice [39-40]. Using a colloidal probe of a well-defined and relatively large spherical geometry allows for greater certainty and repeatability of experiments, as the interactions between probe and surface are greater in magnitude and less susceptible to discrepancies attributed to irregularities on the probe surface. It has already been shown that spheres with radii much larger than characteristic lengthscales of their EDL can be approximated to interact as flat plates. This makes interactions between colloid probes and surfaces rather well-behaved, and stands in sharp contrast with nanoscale radii of coated tips discussed above, whose curvatures are much closer to the magnitude of typical Debye lengths in dilute solutions. However, the smaller scale of the conventional, coated probe tip offers the alternative advantage of increased site specificity, allowing for a surface to be imaged and forces to be measured at a well-defined position [36]. The large radius of the colloidal probe, on the other hand, makes for a rather crude topographic probe, and good positional correlation between an image of a surface and force measurements at various locations is therefore not possible.

Colloid probes have the added advantage of serving as models for the interaction between particles in suspension and a substrate with which they interact. This technique has recently been used to explore local changes in the pH of aqueous solutions during electrophoretic processes as a function of distance away from an electrode [41-42]. It was observed that Faradaic processes occurring at the electrodes during the electrophoretic deposition (EPD) of silica particles was generating H^+ and OH^- that resulted in a pH gradient away from the electrode, causing silica particles to adhere to the substrate prior to reaching the electrode. Colloid probes of silica spheres were used in an AFM study to model this observed behavior. It was found that

interactions between the probe and the surface shifted from repulsive to attractive as a function of both distance from the working electrode and duration of the EPD process.

The effective use of colloid probes in force spectroscopy is limited only by the quality of microspheres that can be produced. A partial list of tips that have been produced includes alumina [43], titania [44], zirconia [45], zinc sulfide [46], magnesium oxide [47], and oxidized tungsten [48]. Polymeric materials such as polystyrene can also be used for microspheres [49]. Material selection of a colloid probe is specific to a given study. Eggleston and Jordan, for example, used colloid probes of various minerals, such as quartz and hematite, to study the interactions between single crystal surfaces of the same material [50]. Larson and coworkers conducted a similar study between a rutile probe and crystal surface. Hydrophobic polystyrene surfaces have been used to probe the influence of hydrophobicity on the interaction between surfaces [51]. Silica probes, however, remain a good choice for studies of the EDL across broad spectrum of solution conditions, because the EDL of silica is known to remain negative to a pH of roughly 2.0. Therefore, as interaction forces shift from repulsion to attraction, these changes can be attributed to a change in sign of the EDL of the surface of interest, allowing for the determination of the isoelectric point of the material to within the bounds of the solution conditions before and after the shift to attractive interaction. This approach will be used in chapters 4 and 5 of this thesis, and more will be discussed in those sections.

2.7.2 Anatomy of a Force-Distance Curve

Raw data from a typical force-distance measurement are shown in Figures 2.8 and 2.10. The data presented in Figure 2.8 shows the extension, or approach, component of a F-d curve where there is a repulsive interaction between the probe tip and the surface. Cantilever deflection is plotted as a function of distance from the surface. At a distance sufficiently far from the surface (1), there are no observable interactions between tip and surface, and the cantilever remains in its rest position, exhibiting no deflection. As it is lowered closer to the surface, however, the double layer of the probe tip begins to interact with the double layer of the surface (2). The onset of this interaction occurs at roughly five Debye layers of separation distance, corresponding to 50 nm in a 0.001 M electrolyte solution (see Figure 2.4).

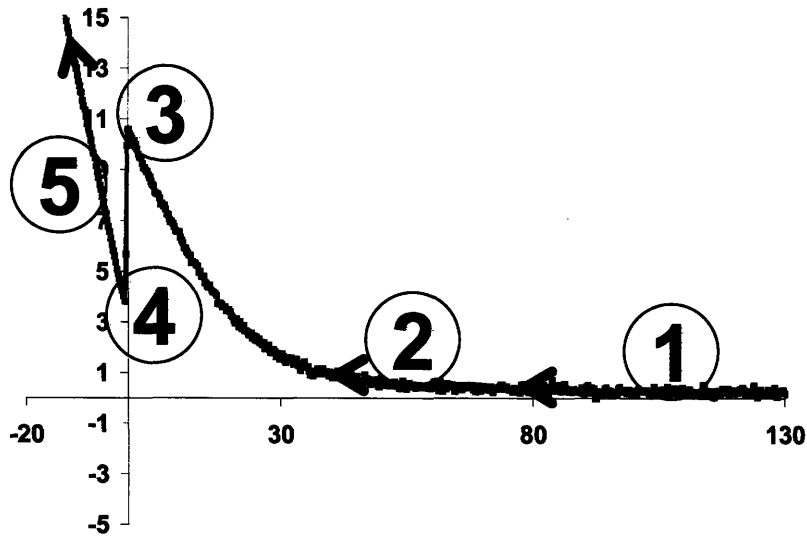


Figure 2.8 Generic force-distance extension curve with a repulsive interaction between the probe tip and the surface. Numbered bubbles highlight various characteristics of the curve.

Further motion of the probe tip towards the surface results in increased cantilever deflection, as the interaction forces between the two double layers increase. The data shown in Figure 2.8 depicts a positive cantilever deflection, indicating a repulsive interaction between double layers of the same sign charge. If the charges of the probe tip and surface were opposite in sign, this interaction would be attractive, as the probe tip would be drawn down towards the surface upon approach. The position (3) in Figure 2.8 represents the maximal interaction force between tip and surface. This maxima appears when the tip and surface are separated by a small distance just large enough to avoid the short-range van der Waals attractions that dominate at small separations. Further approach of the tip towards the surface results in the “jump-to-contact” arising from short-range van der Waals attractions. This is shown in Figure 2.8 as the rapid drop in cantilever deflection from (3) to (4). The strength of these van der Waals interactions is sufficiently strong to override the repulsive interaction between two similarly charged double layers, and results in physical contact between tip and surface. Subsequent tip deflection (5) is merely the flexure of the probe tip as it is pressed against the surface after contact is made at (4). The interaction at (4) therefore represents the zero-point of tip-surface separation.

The data in Figure 2.8 can be converted from piezo-surface separation to tip-surface separation, by factoring in the deflection of the cantilever to measure the true distance of the tip

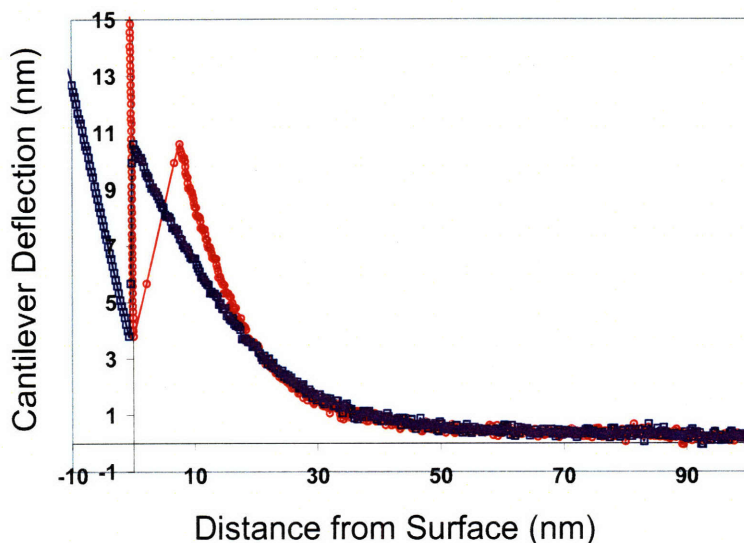


Figure 2.9. The conversion of raw AFM data plotting cantilever deflection as a function of piezoelectric stack position (blue squares) to a plot of cantilever deflection as a function of its actual position (red circles).

from the surface. This is shown in Figure 2.9, where the original data (shown in circles) has been converted to a truer measure of the position of the tip above the surface (squares). This new representation results in all data shown as part of (5) in Figure 2.8 is plotted as a straight vertical line at zero nm separation in Figure 2.9. More over, the distance over which the van der Waals forces dominate tip-surface interactions becomes more clear.

Once the cantilever has traveled its maximum distance and remains pressed against the surface at the end of (5) in Figure 2.8, it must be retracted from this position to begin the next extension curve. The withdrawal, or retraction curve is shown in Figure 2.10, and it too contains data that can also be used to glean significant information about the interaction between tip and surface. The retraction begins with the probe tip pressed against the surface (1), and can remain in contact with the surface at distances well beyond the short separations in the initiated contact during approach. The event (2) shown in Figure 2.10 depicts the “snap-back” of the cantilever as contact between the probe tip and surface is broken. The magnitude of the deflection of the cantilever during retraction provides a means of gauging the adhesive forces between tip and surface. In hydrophilic systems, these forces are often associated with capillary forces between

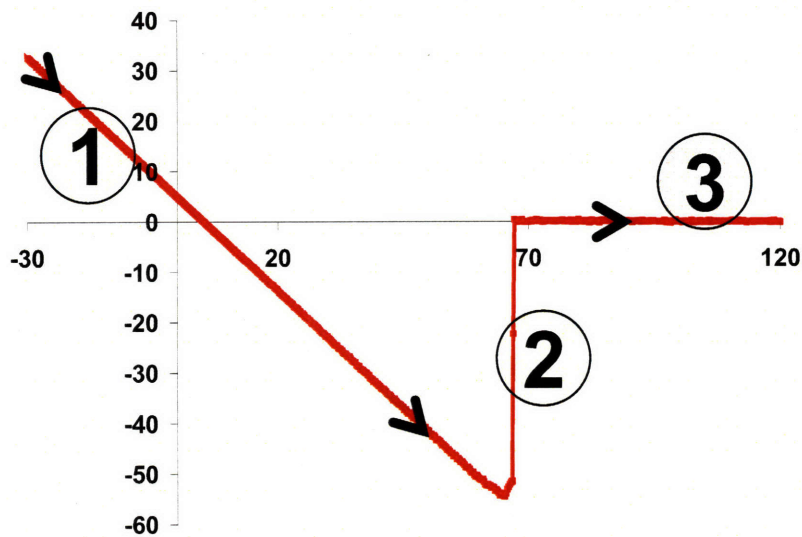


Figure 2.9 Generic force-distance retraction curve revealing an adhesive interaction between the probe tip and the surface after contact. Numbered bubbles highlight various characteristics of the curve.

tip, surface, and liquid media that strongly attract the tip to the surface [10]. Interactions between strongly hydrophobic tips and surfaces have also been observed [10,51]. The last component of the retraction curve, labeled (3) in Figure 2.10, represents the same state shown by (1) in the extension curve, where there is no appreciable interaction between tip and surface at sufficiently large separation distances.

2.8 X-Ray Photoelectron Spectroscopy

An essential, secondary means of surface characterization used in this study is x-ray photoelectron spectroscopy (XPS). This technique operates on the principles of the photoelectric effect, where electrons in the material of interest are excited by incident X-ray radiation. Ejected electrons possess energies characteristic of their originating atomic orbital, and are therefore unique to a specific element. Moreover, XPS is highly sensitive to surface characteristics because although incident X-rays penetrate relatively deeply into a given material, ejected photoelectrons far from the surface are scattered by neighboring atoms and lose their energy before they can escape the material. Only electrons ejected from positions sufficiently close to the surface are capable of leaving the material for detection, which means that signals comprising an XPS spectrum are characteristic of only the first 3-5 Å of a sample. The high degree of sensitivity to elemental surface composition renders XPS a powerful tool for assessing the purity of a given surface.

XPS is also capable of characterizing shifts in energy of emitted photoelectrons from a given element to a certainty of approximately 0.1 eV. Such shifts in energy can distinguish between different chemistries of the same element on a surface; the peak position of carbon photoelectrons, for example, is quite different carbon atoms in carboxyl groups than in amine groups [52]. This would also be true in comparing the signals of pure metals to their respective oxides, or another environment impacting electronic interaction. These differences are exploited here to compare relative electron affinities of various surfaces. This is achieved by depositing an atomically thin monolayer of an electron-rich metal on top of a series of either alumina or titania crystals of various orientations. Shifts in the XPS spectra of the deposited metal are reflective of changes in the interaction between the metal and the underlying oxide surface. Increases in binding energy of the test metal correspond to tighter binding to the oxide, indicating a greater electron affinity.

2.9 REFERENCES

- [1] R.J. Hunter, Foundations of Colloid Science, volume 1. Clarendon Press, Oxford, 1987
- [2] J. Israelachvili, Intermolecular and Surface Forces 2nd Edition. Academic Press, New York, 2000
- [3] E.J.W. Verwey, J.T.G. Overbeek, and K.V. Nes, Theory of the Stability of Lyophobic Colloids. Elsevier Publishing Company, New York (1948)
- [4] Y. Hamnerius, I. Lundstrom, L.E. Paulsson, K. Fontell, and H. Wennerstrom, "Dielectric properties of lamellar lipid water phases." *Chem Phys Lipids* **22** (1978) 135
- [5] Z. Adameczyk and P. Weroński, "Application of the DLVO theory for particle deposition problems." *Adv Colloid Interf Sci* **83** (1999) 137
- [6] R. Hogg, T.W. Healy, and D.W. Furstenuau, "Mutual coagulation of colloidal dispersions." *Trans Farad Soc* **62** (1966) 1638
- [7] G.R. Wiese, and T.W. Healy, "Effect of particle size on colloidal stability." *Trans Farad Soc* **66** (1970) 490

- [8] S. Usui, "Interaction of electrical double layers at constant surface charge." *J Colloid Interf Sci* **44** (1973) 107
- [9] B.V. Derjaguin, "Friction and adhesion IV. The theory of adhesion of small particles." *Kolloid Zeitschrift* **69** (1934) 155
- [10] H.-J. Butt, B. Capella, M. Kappl, "Force measurements with the atomic force microscope: Technique, interpretation, and applications." *Surf Sci Rep* **59** (2005)
- [11] G.M. Bell, S. Levine, L.N. McCarty, "Approximate methods of determining the double-layer free energy of interaction between two charged colloidal spheres." *J Colloid Interf Sci* **33** (1970) 335
- [12] J. Gregory, "Interaction of unequal double layers at constant charge." *J Colloid Interf Sci* **51** (1975) 44
- [13] S. Assemi, J. Nalaskowski, J.D. Miller, and W.P. Johnson, "Isoelectric point of fluorite by direct force measurements using atomic force microscopy." *Langmuir* **22** (2006) 1403
- [14] M. von Smoluchowski, from Handbuch der Electizitat und des Magnetismus Vol 2, (1921) Graetz, Barth, Lipzig
- [15] R.J. Kershner, J.W. Bullard, and M.J. Cima, "Zeta potential orientation dependence of sapphire substrates." *Langmuir* **20** (2004) 4101
- [16] G.V. Franks and L. Meagher, "The isoelectric points of sapphire crystals and alpha-alumina powder." *Col Surf A* **214** (2003) 99
- [17] C. Werner, H. Körber, R. Zimmermann, S. Dukhin, and H.-J. Jacobasch, "Extended electrokinetic characterization of flat solid surfaces." *J Colloid Interf Sci* **208** (1999) 329
- [18] S.L. Walker, S. Bhattacharjee, E.M.V. Hoek, and M. Elimelech, "A novel asymmetric clamping cell for measuring streaming potential of flat surfaces." *Langmuir* **18** (2002) 2193
- [19] H.P. Boehm, "Acidic and basic properties of hydroxylated metal oxide surfaces." *Discuss Farad Soc* **52** (1971) 264
- [20] M. Předota, A. V. Bandura, P.T. Cummings, J.D. Kubicki, D.J. Wesolowski, A.A. Chialvo, and M.L. Machesky, "Electric double layer at the rutile (110) surface. 1. Structure of surfaces and interfacial water from molecular dynamics by use of *ab initio* potentials." *J Phys Chem B* **108** (2004) 12049
- [21] D.M. Griffiths and C.H. Rochester, "Infrared study of the adsorption of water on to the surface of rutile." *J Chem Soc Farad Trans I* **73** (1977) 1510

- [22] R. Schaub, P. Thostrup, N. Lopez, E. Lægsgaard, I. Stensgard, J.K. Nørskov, and F. Besenbacher, "Oxygen vacancies as active sites for water dissociation on rutile TiO₂(110)." *Surface Science* **218** (1989) 178
- [23] R.L. Kurtz, R. Stockbauer, and T.E. Madey, E. Román, and J.L. De Segovia, "Synchrotron radiation studies of H₂O adsorption on TiO₂(110)." *Surface Science* **218** (1989) 178
- [24] K.C. Hass, W.F. Schneider, A. Curioni, and W. Andreoni, "The chemistry of water on alumina surfaces: Reaction dynamics from first principles." *Science* **282** (1998) 265
- [25] P.J. Eng, T.P. Trainor, G.E. Brown, Jr., G.A. Waychunas, M. Newville, S.R. Sutton, and M.L. Rivers, "Structure of the hydrated α -Al₂O₃(0001) surface." *Science* **288** (2000) 1029
- [26] T. Hiemstra, W.H. Van Riemsdijk, and G.H. Bolt, "Multisite proton adsorption modeling at the solid/solution interface of (hydr)oxides: A new approach: I. Model description and evaluation of intrinsic reaction constants." *J Colloid Interf Sci* **133** (1989) 91
- [27] T. Hiemstra, P. Venema, and W.H. Van Riemsdijk, "Intrinsic proton affinity of reactive surface groups of metal (hydr)oxides: The bond valence principle." *J Colloid Interf Sci* **184** (1996) 680
- [28] G. Binnig, C.F. Quate, and C. Gerber, "Atomic Force Microscope." *Phys Rev Lett* **56** (1986) 930
- [29] J.W. Bullard and R.S. Smith, "Structural evolution of the MoO₃(010) surface during lithium intercalation." *Solid State Ionics* **160** (2003) 335
- [30] Y. Gan and G.V. Franks, "High-resolution AFM images of the single-crystal alpha-Al₂O₃(0001) surface in water." *J Phys Chem B* **109** (2005) 12474
- [31] R.L. Smith, G.S. Rohrer, K.S. Lee, D.K. Seo, and M.H. Whangbo, "A scanning probe microscopy study of the (001) surfaces of V₂O₅ and V₆O₁₃." *Surface Science* **367** (1996) 87
- [32] L.H. Dubois and R.G. Nuzzo, "Synthesis, structure, and properties of model organic surfaces." *Annu Rev Phys Chem* **43** (1992) 437
- [33] C.D. Frisbie, L.F. Rozsnyai, Y. Noy, M.S. Wrighton, and C.M. Lieber, "Functional group imaging by chemical force microscopy." *Science* **265** (1994) 2071
- [34] F.A. Ahimou, F.A. Denis, A. Touhami, Y.F. Dufrêne, "Probing microbial cell surface charges by atomic force microscopy." *Langmuir* **18** (2002) 9937
- [35] H.X. He, W. Huang, H. Zhang, Q.G. Li, S.F.Y. Li, and Z.F. Liu, "Demonstration of high-resolution capability of chemical force titration via study of acid/base properties of a patterned self-assembled monolayer." *Langmuir* **16** (2000) 517

- [36] D.V. Vezenov, A. Noy, L.F. Rozsnyai, and C.M. Lieber, "Force titrations and ionization state sensitive imaging of functional groups in aqueous solutions by chemical force microscopy." *J Am Chem Soc* **119** (1997) 2006
- [37] D. Dean, J. Seog, C. Ortiz, and A.J. Grodzinsky, "Molecular-level theoretical model for electrostatic interactions with polyelectrolyte brushes: Applications to charged glycosaminoglycans." *Langmuir* **19** (2003) 5526
- [38] J. Vandiver, D. Dean, N. Patel, W. Bonfield, and C. Ortiz, "Nanoscale variation in surface charge of synthetic hydroxyapatite detected by chemically and spatially specific high-resolution force spectroscopy." *Biomaterials* **26** (2005) 271
- [39] W.A. Ducker, T.J. Sneden, and R.M. Pashley, "Direct measurement of colloidal forces using an atomic force microscope." *Nature* **353** (1991) 239
- [40] H.-J. Butt, "Electrostatic interaction in atomic force microscopy." *Biophys J* **60** (1991) 777
- [41] R.J. Kershner, J.W. Bullard, and M.J. Cima, "The role of electrochemical reactions during electrophoretic particle deposition." *J Colloid Interf Sci* **278** (2004) 146
- [42] J.W. Bullard, R.J. Kershner, and M.J. Cima, "Scanning Probe Characterization of Localized pH Changes on a Sapphire Surface in the Presence of an Applied Field." *Proc Mat Res Soc* **782** (2003) A3.1.1
- [43] T. Kakui, T. Miyauchi, and H. Kamiya, "Analysis of the action mechanism of polymer dispersant on dense ethanol alumina suspension using colloidal probe AFM." *J Eur Ceram Soc* **25** (2005) 133
- [44] I. Larson, C.J. Drummond, D.Y.C. Chan, and F. Grieser, "Direct force measurements between TiO₂ Surfaces." *J Am Chem Soc* **115** (1993) 11885
- [45] H.G. Pederson and L. Bergström, "Forces measured between zirconia surfaces in poly(acrylic acid) solutions." *J Am Ceram Soc* **82** (1999) 1137
- [46] D.T. Atkins and R.M. Pashley, "Surface forces between ZnS and mica in aqueous electrolytes." *Langmuir* **9** (1993) 2232
- [47] A. Kauppi, K.M. Anderson, and L. Bergström, "Probing the effect of superplasticizer adsorption on the surface forces using the colloidal probe AFM technique." *Cement Concrete Res* **35** (2005) 133
- [48] K.M. Anderson and L. Bergström, "DLVO interactions of tungsten oxide and cobalt oxide surfaces measured with the colloidal probe technique." *J Colloid Interf Sci* **246** (2002) 309

- [49] Y.Q. Li, N.J. Tao, J. Pan, A.A. Garcia, and S.M. Lindsay, "Direct measurement of interaction forces between colloidal particles using the scanning force microscope." *Langmuir* **9** (1993) 637
- [50] C.M. Eggleston and G. Jordan, "A new approach to pH of point of zero charge measurement: Crystal-face specificity by scanning force microscopy (SFM)." *Geochem Cosmochem Acta* **62** (1998) 1919
- [51] H.K. Christenson and Per M. Claesson, "Direct measurements of the force between hydrophobic surfaces in water." *Adv Colloid Interf Sci* **91** (2001) 391
- [52] J.F. Moulder, W.F. Stickle, P.E. Sobol, and K.D. Bomben, Handbook of X-ray Photoelectron Spectroscopy. J. Chastain and R.C. King, Jr, eds, Physical Electronics, Inc, Eden Prairie, MN, 1995

Chapter 3: Orientation-Dependence of Surface Properties of Sapphire

3.1 Preface

The genesis of proceeding chapters of this thesis is rooted in initial results investigating the orientation dependence of the isoelectric point of various orientations of α -alumina single crystals, commonly referred to as sapphire. It is not this author's intention to claim ownership of this work; it was originally published in another thesis [1], and his contributions to this work have already been acknowledged [2]. Nevertheless, the results provide an important backdrop to much of the work that follows, as they represent the first successful investigation of isotropic colloidal behavior substantiated by independent analysis of the electronic properties of the surfaces in question. A brief summary of them therefore serves as an excellent context for ensuing analysis and discussion.

3.2 Streaming Potential and XPS Results

The initial work in CPRL investigating the relationship between atomic structure and colloidal behavior examined the isoelectric points of single crystal alumina as a function of surface orientation [2]. These measurements are the first to report on this effect, and successfully correlated mesoscale studies of streaming potential measurements to the results of x-ray photoelectron spectroscopy (XPS) analyses of the electronic structure of several sapphire orientations. Streaming potential measurements were performed on samples of epi-polished C-plane (0001), A-plane (11 $\bar{2}$ 0) and R-plane (1 $\bar{1}$ 02) surfaces over a broad range of pH values in aqueous KCl solutions with ionic strengths of 1mM, 10mM, and 100mM. The measurements indicated approximate isoelectric points of pH = 4.5 for R-plane surfaces, pH = 5.5 for A-plane surfaces, and pH = 6.0 for the C-plane orientation as shown below in Figure 3.1. That is, the R-plane is most acidic and the C-plane is most basic.

This orientation dependence was further shown to be linked to variations in the electronic structure of each surface. Electron beam deposition was used to coat a sample of each orientation in a film of iridium approaching the thickness of a single monolayer. Angle-resolved x-ray photoelectron spectroscopy (XPS) was performed using a non-monochromated Mg K α radiation

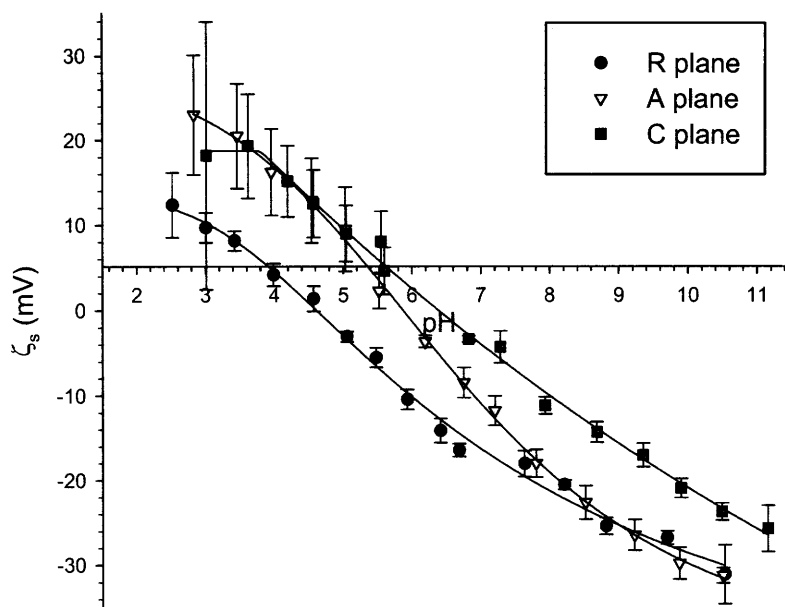


Figure 3.1: Results of streaming potential measurements conducted in a 10 mM KCl solution, replotted with error bars. All orientations are shown to illustrate dramatic shift in i.e.p. and increase in acidity of R-plane surface. Taken from [2].

source. Quantification of the Ir_{NNN} Auger peaks and the Ir_{4f} photoelectron peaks for monolayers deposited on each orientation was used to calculate the modified Auger parameter (MAP), a value representing the difference between the binding energies of these peaks that is used to filter out the influence of surface charging on the analysis. The results are shown in both Figure 3.2 and the table that follows.

The XPS spectra indicate nearly identical Auger peaks for all three orientations of sapphire, while a dramatic shift of over 0.5 eV was measured in the photoelectron peaks at 30° incidence. The C-plane surface peak was observed to occur at the lowest binding energy, with the highest binding energy peak corresponding to the R-plane sample. The calculated MAP at 70° incidence also reveals a similar (though less dramatic) shift spanning 0.09 eV. The energy required to remove a core electron from atoms contained within the Ir film is greatest for the monolayer deposited on the R-plane substrate. Considering a simple electrostatic model, it follows that this energy should increase with increasing positive net atomic charge. The effect of the more acidic R-plane substrate is to more strongly bind the outermost electrons of Ir. The A-

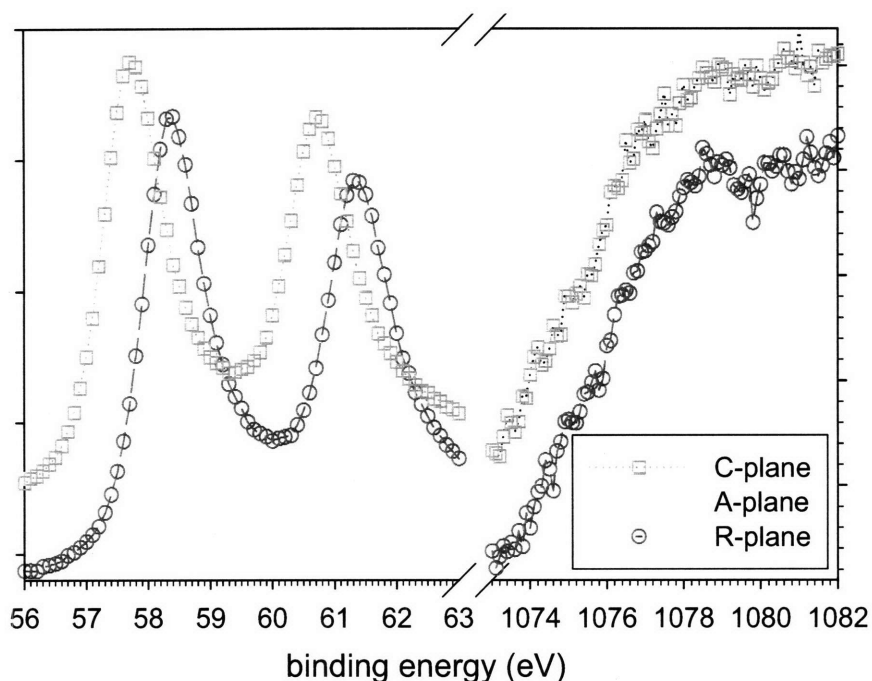


Figure 3.2. XPS analysis of an Ir monolayer deposited on the C-plane (squares), A-plane (triangles) and R-plane (circles) surfaces of Al_2O_3 . Overlapping Auger peaks are shown at higher binding energies, on the right-hand side of the plot. Differences in binding energies for each of the three photoelectron peaks is associated with differences in the electron affinities of each of the three underlying surfaces. Higher binding energies correlate to increased electron affinities, which also result in lower isoelectric points.

and C-plane substrates exhibiting a higher i.e.p. have a less dramatic effect on the Ir MAP. These less acidic surfaces will consequently bind the outer most iridium electrons less strongly, providing further validation for the observed shift in i.e.p. for the three different orientations of sapphire.

Orientation	Approx. i.e.p.	M.A.P. (eV)	Surface hydroxyls per nm^2
R-Plane	4.5	234.48	12.15
A-Plane	5.5	235.05	14.56
C-Plane	6.0	233.84	9.0

*Data taken from [2]

3.3 Discussion: Developing Structure-Property Relationships

Can these consistent experimental observations of surface chemistry be related to structure? The most stable form of alumina, the α - Al_2O_3 single crystal has a corundum structure with a hexagonal unit cell composed of two molecules and possessing rhombohedral symmetry of space group D_{3d}^6 . The unit cell contains 12 Al^{3+} and 18 O^{2-} ions with $a = 4.76 \text{ \AA}$ and $c = 12.99 \text{ \AA}$ [3]. The oxygen anions are arranged in a close-packed array, with aluminum cations occupying 2/3 of the available octahedral interstitial sites. This bulk structure results in each Al^{3+} being surrounded by six O^{2-} , while the coordination number of the oxygen sites is four. Considering first the easiest orientation to visualize, the C- (or basal) plane is oriented parallel to the close-packed array of oxygen sites and has been well-characterized in the literature. Several unique C-plane surfaces can be realized at each orientation depending on the manner in which the crystal is cleaved. The termination of the surface of the crystal is paramount to understanding the adsorption of potential-determining ions and other surface active species. The temperature-dependent surface reconstruction will also dictate the arrangement of surface ions, such that the total energy of the surface is minimized by the lateral motion of ions within the surface plane. Experimental [4-9] and theoretical [10] studies suggest that the C-plane surface possesses a (1x1) unreconstructed surface identical to the bulk crystal up to temperatures of approximately 1370 K, with various other reconstructions resulting from annealing at more elevated temperatures [11-13]. The existence of both oxygen [14] and aluminum C-plane terminated surfaces [15-17] has been reported in the literature. This latter conclusion is based on the highly stable nature of the electrically neutral Al-O-Al stacking sequence that occurs for this configuration.

Limited work concerning the reconstruction and termination of the A- and R-plane surfaces has been presented in the literature, although a few studies do tackle these more complicated structures. Guo, Ellis, and Lam reported termination of the R-plane surface with a single layer of O^{2-} [15], although more recent experimental evidence has not been provided. This conclusion was again based on the reduction in energy afforded by the oxygen termination. Reconstruction of the R-plane sapphire surface has not been reported at all. The A-plane surface, on the other hand, is known to exhibit a number of reconstructions upon annealing, with the lowest temperature (3x1) structure occurring at 900 K [6,18].

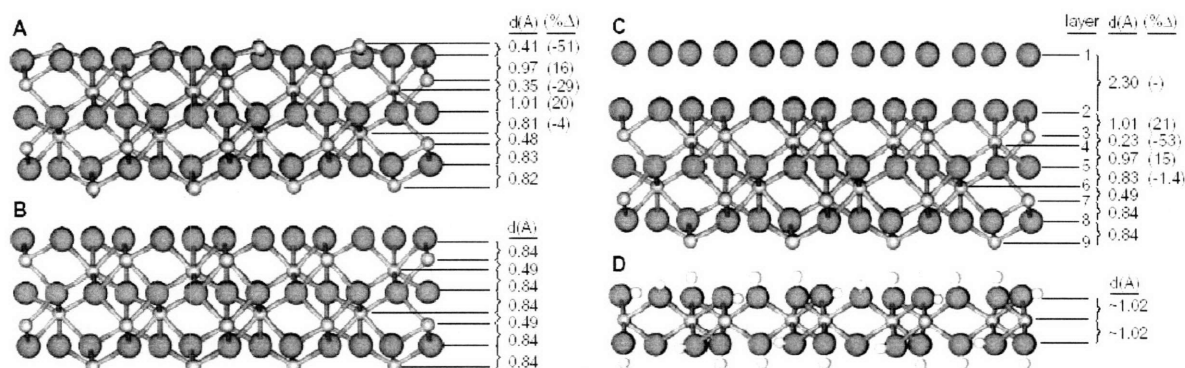


Figure 3.3. Various possible terminations of the atomic layering sequences in the [0001] direction for sapphire. (A) represents an aluminum-terminated surface, (B) an idealized oxygen-terminated surface, and (C) demonstrates the adsorption of a layer of water on top of a hydroxylated phase at the surface, whose full structure is shown in (D). The %Δ column in (A) and (C) represents the percent change in layer spacing from the idealized structure depicted in (B). Larger spheres represent oxygen atoms, while smaller ones represent aluminum. Taken from [24].

The formation of a surface by cleaving the crystal and polishing results in a reduction in coordination of the surface atoms as compared with the bulk. Each surface Al^{3+} is coordinated by three oxygen anions, regardless of the crystallographic orientation. This configuration is indifferent to orientation, but rotates with respect to a given surface plane such that the bond lengths are maintained. These rotations result in changes in atomic coordination at the surface, leading to varying degrees of surface relaxation, and thus giving rise to changes in surface acidity with orientation. The reduction in coordination as compared with the bulk is expected to have a dramatic effect on the position of the surface aluminum cations, causing them to effectively relax into the bulk structure towards the three coordinating oxygen anions below. This phenomenon has been studied in the literature for C-plane surfaces using advanced computational techniques which model up to eighteen alternating Al^{3+} and O^{2-} layers of the surface structure as a multi-layer slab [9,19-22]. Verdozzi, et. al. report the repositioning of the surface Al^{3+} layer by as much as -87.4% [19], with the minus sign denoting a relaxation into the plane of oxygen anions immediately below this surface layer such that the aluminum becomes nearly co-planar. These models also show a slight shift of the oxygen layer towards the surface such that the co-planar oxygens are displaced by approximately +3.0%. Much less dramatic shifts occur on various planes of subsurface atoms until the relaxations are eventually damped out in the bulk. The surface relaxations for aluminum ions on the A and C surfaces can be estimated using equivalent radii for the surface aluminum ion as determined from the C-plane. This is essentially equivalent to assuming a constant radii for tricoordinate aluminum ion. The

order of increasing aluminum ion coordination is determined to be R, A, C, which is the same order of decreasing acidity of these surfaces.

This apparent correspondence between structure and surface chemistry of alumina is complicated, however, by recent studies which suggest that water molecules can readily dissociate on pristine C-plane sapphire surfaces at ambient temperatures [23]. This dissociation results in the formation of a hydroxylated monolayer whose structure was identified by the investigating authors as the mineral gibbsite [24]. Oxygen layers of the hydroxylated gibbsite structure, however, exhibit an ABBA stacking sequence, resulting in the simple packing of layers in the stacking direction [25]. The alternative bayerite structure, however, exhibits a nearly identical in-plane arrangement of aluminum and oxygen atoms, yet stacks these layers in a close-packing arrangement [26], rendering it a more viable candidate for epitaxial growth.

The structures of both pristine, relaxed C-plane sapphire and its hydroxylated counterpart are shown above in Figure 2, along with the unrelaxed, oxygen-terminated structure shown for comparison. In this basal orientation, the surface exposure of the Al-O polyhedron is maximized, allowing for the hydroxylation of three oxygen sites for every aluminum atom and resulting in the formation of a uniform layer of aluminum hydrate on the surface. Changes in surface orientation correspond to a rotation of the Al-O polyhedron relative to the terminating surface, and result in a decrease in the number of hydroxylated oxygen sites per aluminum atom. This is shown below in Figure 3, which depicts oxygen-terminated surfaces of (a) C-plane, (b) A-plane, and (c) R-plane orientations. This change in hydroxyl density hinders the epitaxial growth of a uniform hydroxylated surface on non-basal orientations. Both R- and A- plane orientations are therefore presumed to contain significantly smaller quantities of the hydroxylated phase. The isoelectric point of the hydroxylated bayerite structure is typically accepted as approximately $\text{pH} = 9.0$, or 3-5 decades higher than measured values of single crystal sapphire surfaces. The aqueous behaviors of various orientations of sapphire are undoubtedly influenced by the extent to which this hydroxylated monolayer is present on the surface.

These preliminary studies successfully demonstrate measurable anisotropies in the surface potential characteristics of alumina surfaces using conventional measurement techniques. The structure-property correlations are further supported by atomic level investigations which expose variations in the electronic nature of each surface. Considering the results of Eng and co-workers [24], however, requires a more complex model of the influence of surface structure on

the properties of sapphire. Their observation of the formation of a hydroxylated surface phase on C-plane sapphire, for example, dictates that surfaces be described not only in terms of their assumed activity in solution, but also in terms of structural differences. These differences permit or deny the formation of new surface phases which have the potential to directly impact chemical behavior. Forging such links between the two separate investigations is a powerful means of understanding how atomic-scale anisotropies influence surface characteristics relevant to micron-scale interactions.

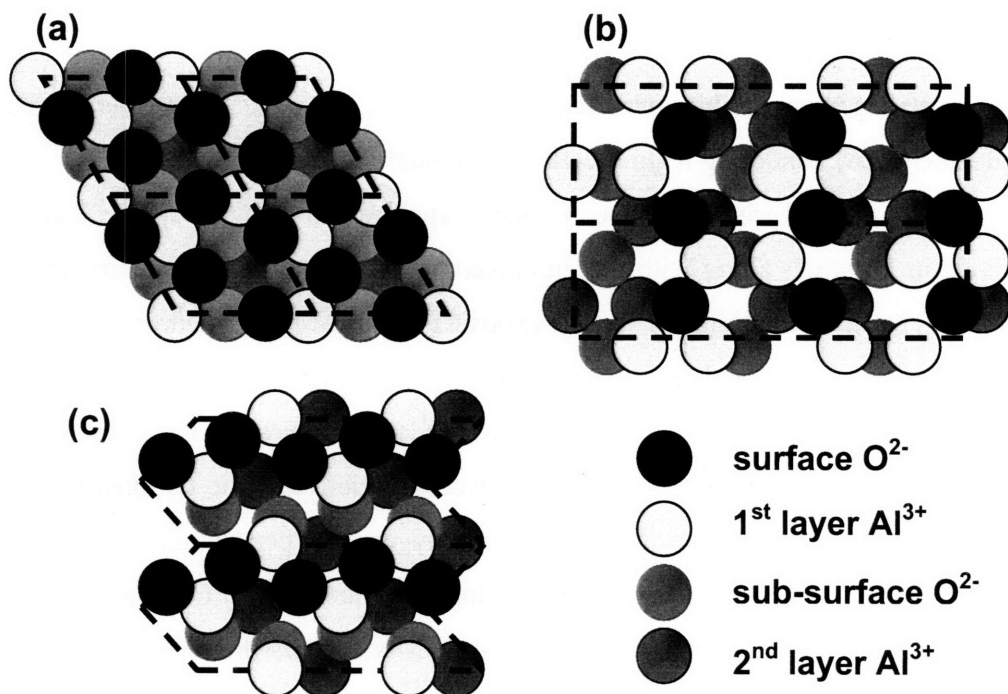


Figure 3.4: Oxygen-terminated schematic of the crystallographic orientations of the (a) C-plane, (b) A-plane, and (c) R-plane surface terminations of alumina. Changes in surface configuration result in a decrease, relative to the C-plane configuration, in oxygen sites per aluminum atom available for hydroxyl termination. This decrease likely corresponds to a reduction in the affinity of a given alumina surface for the growth of a bayerite epilayer. Dimensions of unit cells are delineated by dotted lines. Relative sizes of the ionic radii are exaggerated for clarity. Taken from [2].

3.4 REFERENCES

- [1] R.J. Kershner, Surface Forces During Electrophoretic Assembly of Micron Scale Silica Particles, *Doctoral Thesis*, M.I.T., 2004
- [2] R.J. Kershner, J.W. Bullard, and M.J. Cima, "Zeta potential orientation dependence of sapphire substrates." *Langmuir* **20** (2004) 4101
- [3] R.W.G. Wyckoff, *Crystal Structures. Vol. 2*. 2nd ed.; Interscience Publishers: New York, 1964
- [4] M. Gautier, J.P. Duraud, L. Pham Van, and M.J. Guittet, "Modifications of α -Al₂O₃ (0001) surfaces induced by thermal treatments or ion bombardment." *Surf. Sci.* **250** (1991) 71
- [5] J.M. Charig, "Low-energy electron diffraction observations of α -alumina." *Appl. Phys. Lett.* **10** (1967) 139
- [6] C.C. Chang, "LEED (low-energy electron diffraction) studies of the (0001) face of α -alumina." *J. Appl. Phys.* **39** (1968) 5570
- [7] T.M. French and G.A. Somorjai, "Composition and surface structure of the (0001) face of α -alumina by low-energy electron diffraction." *J. Phys. Chem.* **74** (1970) 2489
- [8] D.W. Susnitzky and C.B. Carter, "Identification of α -alumina surface structures by electron diffraction." *J. Am. Ceram. Soc.* **69** (1986) C217
- [9] S. Baik, D.E. Fowler, J.M. Blakely, and R. Raj, "Segregation of Mg to the (0001) surface of doped sapphire." *J. Am. Ceram. Soc.* **68** (1985) 281
- [10] R. Di Felice and J.E. Northrup, "Theory of the clean and hydrogenated Al₂O₃(0001)-(1x1) surfaces." *Phys. Rev. B* **60** (1999) R16287
- [11] C. Barth, and M. Reichling, "Imaging the atomic arrangements on the high-temperature reconstructed α -Al₂O₃ (0001) surface." *Nature* **414** (2001) 54
- [12] E.A.A. Jarvis and E.A. Carter, "Metallic character of the Al₂O₃(0001)-($\sqrt{31} \times \sqrt{31}$)R $\pm 9^\circ$ surface reconstruction." *J. Phys. Chem. B* **105** (2001) 4045
- [13] I. Vilfan, F. Lançon, and J. Villain, "Rotational reconstruction of sapphire (0001)." *Surf. Sci.* **392** (1997) 62
- [14] M. Arbab, G.S. Chottiner, and R.W. Hoffman, "An ARXPS (angle-resolved x-ray photoelectron spectroscopy) investigation of the initial growth of aluminum films on the (0001) face of sapphire." *Proc. Mat. Res. Soc.* **153** (1989) 63

- [15] J. Guo, D.E. Ellis, and D.J. Lam, "Electronic structure and energetics of sapphire (0001) and $(1\bar{1}02)$ surfaces." *Phys. Rev. B* **45** (1992) 13647
- [16] J. Ahn and J.W. Rabalais, Composition and structure of the $\text{Al}_2\text{O}_3(0001)-(1\times 1)$ surface." *Surf. Sci.* **388** (1997) 121
- [17] T. Suzuki, S. Hishita, K. Oyoshi, and R. Souda, "Structure of $\alpha\text{-Al}_2\text{O}_3(0001)$ surface and Ti deposited on $\alpha\text{-Al}_2\text{O}_3(0001)$ substrate: CAICISS and RHEED study." *Surf. Sci.* **437** (1999) 289
- [18] C.C. Chang, "Silicon-on-sapphire epitaxy by vacuum sublimation: LEED-Auger studies and electronic properties of the films." *J. Vac. Sci. Technol.* **8** (1971) 500
- [19] C. Verdozzi, D.R. Jennison, P.A. Schultz, and M.P. Sears, "Sapphire (0001) surface, clean and with d-metal overlayers." *Phys. Rev. Lett.* **82** (1999) 799
- [20] C. Pisani, M. Causa, R. Dovesi, and C. Roetti, "Hartree-Fock *ab initio* characterization of ionic crystal surfaces with a slab model. The (0001) face of α -alumina." *Progress in Surf. Sci.* **25** (1987) 119
- [21] M. Causa, R. Dovesi, C. Pisani, and C. Roetti, "*Ab initio* characterization of the (0001) and (10.hivin.10) crystal faces of α -alumina." *Surf. Sci.* **215** (1989) 259
- [22] V. E. Puchin, J.D. Gale, A.L. Shluger, E.A. Kotomin, J. Guenster, M. Brause, and V. Kempter, "Atomic and electronic structure of the corundum (0001) surface: Comparison with surface spectroscopies." *Surf. Sci.* **370** (1997) 190
- [23] K.C. Hass, W.F. Schneider, A. Curioni, and W. Andreoni, "The chemistry of water on alumina surfaces: Reaction dynamics from first principles." *Science* **282** (1998) 265
- [24] P.J. Eng, T.P. Trainor, G.E. Brown, Jr., G.A. Waychunas, M. Newville, S.R. Sutton, and M.L. Rivers, "Structure of the hydrated $\alpha\text{-Al}_2\text{O}_3(0001)$ surface." *Science* **288** (2000) 1029
- [25] H.D. Megaw, "The Crystal Structure of Hydrargillite, $\text{Al}(\text{OH})_3$." *Z. Krist.* **87** (1934) 13
- [26] R. Rothbauer, F. Zigan, and H. O'Daniel, "Verfeinerung der struktur des bayerits, $\text{Al}(\text{OH})_3$: Einschließlich eines vorschlag für die H-positionen" *Z. Krist.* **125** (1967) 317

Chapter 4: Anisotropy of the IEP of Rutile Surfaces

4.1 Introduction

Anisotropic characteristics of the behavior of the electrical double layer have been observed in a variety of materials systems. The edges and faces of kaolinite particles have long been known to acquire charges of opposite sign under certain solution conditions [1-3]. Recent measurements of double-layer properties of (110)-oriented CaF_2 [4] indicated a sharp contrast between the isoelectric points of that surface and the previously-studied (111) orientation [5,6]. Other work has noted anisotropy among hematite surfaces [7], and observed differences in various orientations of sapphire surfaces have been discussed previously [8,9].

Modern surface adsorption theory, known as Multi-Site Complexation (MUSIC) theory, predicts that the strength and extent of the acidity of a given surface will be a function of both the density and electron affinity of available adsorption sites. The most prominent of these sites are predicted to be cationic surface positions, which behave as Lewis acid sites and bond to solvated hydroxyl groups [10]. Anionic oxide positions, however, do not necessarily behave exclusively as basic loci. Many researchers, for example, have defined certain oxygen sites on the rutile surface to have a slightly acidic character. It further follows that as various surfaces of a given material system are exposed to a particular electrolyte, new and different complexation sites will interact at the interface.

The double layer behavior of various single-crystalline TiO_2 surfaces has been previously studied under a variety of experimental conditions. Larson and co-workers used AFM to make force-distance measurements between a silica probe tip and a single orientation of rutile [11]. Hu and coworkers made similar measurements on a sample of n-type (001) rutile, observing changes in the double layer as a function of applied potential [12]. Work by Fieler and collaborators used AFM to demonstrate the potential-determining influence of solvated phosphate ions on the surface potential of rutile [13]. More recently, Bedzyk has used the x-ray standing-wave (XSW) technique to study the adsorption of a variety of cations on both the (110) and (001) rutile surfaces [14,15], and others have used second-harmonic generation (SHG) to determine the isoelectric point of (110) rutile [16].

Presented here is what we believe to be the first comprehensive study of the pH-dependent behavior of the surface potential of rutile for (110), (001), and (100) surfaces. Force-

distance measurements were performed with an atomic force microscope (AFM) on each surface in aqueous solutions of two different ionic strengths and at multiple pH values. The experiments provide the opportunity to isolate the behavior of a surface of interest from that of other surfaces, and to compare results across orientations in order to begin to develop empirically-based structure-property relationships to explain the observed behavior. Specifically, the AFM work yielded important information regarding the isoelectric points (ieps) of the three surfaces.

AFM data were substantiated by investigations with X-ray photoelectron spectroscopy (XPS). These measurements involved the deposition of an approximately 5 Å thick layer of palladium metal on a surface of each of the three orientations of interest. The binding energy of core electrons associated with the Pd atoms was measured in the form of photoelectron peaks, and shifts in this energy were observed across orientations of the rutile substrates. The shifts provided a secondary means of gauging the electron affinity of each of the rutile surfaces; Pd signals at higher binding energies corresponded to surfaces of greater electron affinity, referred to as increased surface acidity. The relative acidities of the three surfaces of interest corresponded to the relative values of the iep, with the surface deemed most acidic through XPS analysis also exhibiting the lowest iep, and therefore binding electron-donating potential determining ions (i.e., hydroxyl groups) the tightest. The results presented build on previous work with sapphire surfaces that used a similar approach to quantifying observed differences in iep with a secondary means of analysis.

4.2 Materials and Methods

4.2.1 Solution and Sample Preparation

Aqueous potassium chloride solutions of varying ionic strengths were prepared in polypropylene bottles that were rinsed thoroughly with deionized water prior to use. High-purity, deionized water having a resistance of 18 MΩ was purchased from RICCA for both cleaning and solution preparation. 99.95% pure potassium chloride salt (Malinkroft) was used to prepare solutions of varying ionic strengths ranging from 1×10^{-4} M to 1×10^{-2} M concentrations. The pH of these solutions was adjusted with the addition of either HCl or KOH, and in the interest of maintaining as constant an ionic strength as possible in solutions across the pH spectrum, no solution was treated with both acid and base. Solutions used in a given set of experiments were prepared just prior to the start of an experiment. The same solution was used for measurements

on all three surfaces of interest, thereby maintaining as constant a pH value as possible across the experiments.

Single crystal titanium dioxide (rutile form) samples were purchased from Commercial Crystal Laboratories, Inc. (Naples, FL). Crystals having orientations of (110), (100), and (001) were used in these experiments. All crystals were epi-polished by the vendor, and etched in a 4:1 H₂SO₄:H₂O₂ bath, commonly referred to in the microfabrication industry as a piranha etch, upon receipt. Samples were then thoroughly rinsed in deionized water, blown dry with nitrogen gas, and stored in darkness in a dry box. X-ray photoelectron spectroscopy (XPS) of these samples demonstrated that the piranha etch was successful in removing organic contaminants from the surface without introducing any additional impurities. Samples were also imaged after piranha treatment with an atomic force microscope to confirm that their polish was appropriately smooth.

4.2.2 AFM Measurements

Force-distance measurements were performed on atomic force microscopes available at the Center for Materials Science and Engineering (CMSE) at MIT. Both a Digital Instruments Nanoscope III controller with a Dimension 3000 microscope and a Digital Instruments Nanoscope IV controller with a Dimension 3100 microscope were used, although the same piezoelectric scanner was employed in all experiments. Force-distance curves were taken at a scan rate of approximately 1 Hz, with approach ramps varying as a function of the adhesion of the tip on the retraction curve, which varied with crystallographic orientation of the surfaces. Generally speaking, approach distances varied from 250 nm to 600 nm corresponding to tip velocities of approximately 0.5 to 1.2 $\mu\text{m/s}$. Approximately 15-20 Force-distance curves were taken at three different locations on each sample. All data was exported in ASCII format for processing and statistical analysis in a Matlab program developed in-house. See Appendix I for the details of the major components of the Matlab analysis code.

Contact-mode AFM cantilevers with 5 μm diameter silica spheres attached in lieu of standard silicon nitride imaging tips were purchased from BioForce Nanosciences. An optical image of such a probe tip is shown in Figure 4.1, where it can be clearly seen that the conventional nitride tip has been replaced by a large silica sphere. Silica was selected as a colloid probe because of its extremely low isoelectric point at $\text{pH} \approx 2.0$ has been well-established in the

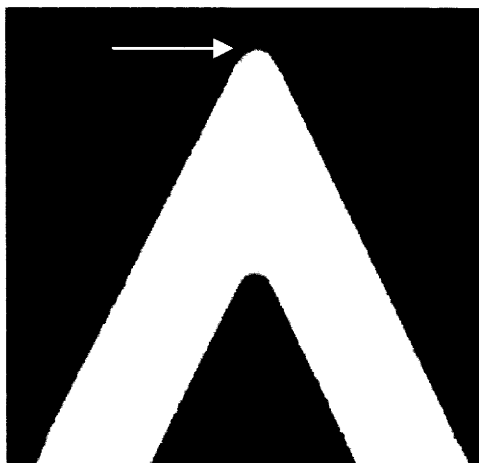


Figure 4.1. Optical image of a contact mode AFM cantilever with a 5 μm diameter colloid sphere attached in the usual presence of a silicon nitride imaging tip. The sphere is highlighted by the arrow.

literature [17-19], and also repeated here. This low value ensures that the electric double layer of the probe remains negative in sign over the entire pH spectrum used in AFM experiments. Therefore, any observed changes in force-distance measurements associated with a shift from repulsive to attractive long-range (i.e. non-van der Waals) interactions between surface and probe tip can be attributed to a change in sign of the electrical double layer of the rutile surface. The tips had nominal spring constants k_c of either 0.06 N/m or 0.12 N/m, depending on the thickness of the cantilever purchased. These values were initially confirmed using the Sader method on an Asylum Research MFP3D molecular force probe [20,21], a technique generally known to gauge k_c to within approximately 10%. Tips were stored in a sealed container inside a dry box when not in use, and were thoroughly rinsed in deionized water immediately prior to their use in AFM experimentation. Approximately 15-20 Force-distance curves were taken at three different locations on each sample.

Force-distance measurements were performed on each crystal orientation of interest as a function of pH. Variability in the conditions of the aqueous environment across samples were minimized by making measurements on all samples at a single pH value before solution conditions were changed, as opposed to making all measurements on a given surface across the pH spectrum before changing samples. This also ensured that any changes in solution conditions attributed to ambient influences as a function of time did not impact measurements on one sample any differently than measurements on another. That is, if the pH or ionic strength of a solution regarded as vulnerable to changes due to events such as evaporation or the adsorption of CO_2 from air over, these changes will impact the force measurements of all samples to the same

degree. However, measurement of the pH and conductivity of solutions used revealed them to be highly stable over several hours.

Measurements were made across the pH spectrum in order of decreasing pH, starting from $\text{pH} \approx 7.0$. The pH was adjusted by rinsing the surface thoroughly with the new solution of interest, and any residual solution from experiments at the previous pH was removed from the AFM tip by gently wetting it with a small ($\sim 5 \mu\text{L}$) droplet of the new solution. The sample was then placed beneath the cantilever with $40 - 50 \mu\text{L}$ of new solution and allowed to equilibrate for approximately five minutes. Care was taken to minimize variation in the time allowed for equilibration, as any significant evaporation from such a small droplet size could alter the ionic strength and pH of the solution.

4.2.3 Zeta Potential Measurements of Particles

The zeta-pH characteristics of dilute silica and rutile suspensions were probed with a ZetaPALS zetameter (Brookhaven Instrument Corp, NJ). Measurements of the zeta potential for silica spheres were made on diluted suspensions of monodisperse, $1.5 \mu\text{m}$ silica spheres (Duke Scientific), in order to approximate zeta of the colloidal force probes used in the AFM measurements. The zeta potential of $1 \mu\text{m}$ -diameter, high purity rutile powder (Toho, Japan) was measured to compare to values found in literature and to those measured on the single crystalline surfaces via AFM. Measurements of zeta on rutile also served as a first pass to confirm that the background electrolyte used in AFM experiments was not potentially determining.

The principles governing the use of the ZetaPALS zetameter were outlined in section 2.6. Measurements of zeta were made over a broad spectrum of pH, with KCl serving as the background electrolyte in all measurements. Measurements were taken with solutions containing 0.001 M and 0.010 M KCl to demonstrate that it is not potential determining for either oxide system. The pH of the suspensions was adjusted with the addition of 0.010 M HCl or 0.010 M KOH. Each data point is comprised of an average of fifteen measurements of zeta potential taken over a period of approximately eight minutes, with each individual measurement the result of 20 iterations of a fit to the phase signal of the instrument.

4.2.4 X-ray Photoelectron Spectroscopy

X-ray photoelectron spectroscopy (XPS) was used as a means of verifying the efficacy of the piranha etch cleaning technique on rutile samples, as a check against impurities on the surface, and as an analytical tool to determine the relative surface acidities of the three surfaces of rutile investigated. All XPS measurements were performed using monochromated Al K α radiation as an excitation source under UHV conditions, with a base-pressure on the order of 5×10^{-10} torr. Relative acidities of the rutile surfaces were determined by depositing a nominal monolayer of palladium on each of the three orientations with an electron beam evaporator and measuring both the Pd 3d photoelectron peaks and the Pd MMV Auger peak to determine the modified Auger parameter (MAP) of Pd as a function of substrate orientation. XPS spectra used for MAP determinations were measured at take-off angles of 0° , 30° , and 70° from normal incidence. Palladium was selected as a test metal for MAP measurements because of its stability as a noble metal in ambient conditions, its relatively sharp Auger peaks, and the occurrence of its characteristic XPS peaks in positions along the spectrum that do not coincide with principal XPS and Auger peaks of carbon, titanium, and oxygen.

4.3 Results

4.3.1 Zeta Potential of Silica and Rutile Powder Suspensions

The results of ZetaPALS measurements of ζ for suspensions of monodisperse silica spheres in 0.001 M KCl as a function of pH is shown in Figure 4.2. The data closely resemble other data published for silica systems [17-19], and suggest an iep for the silica spheres on the order of pH = 2.0, in good agreement with work done elsewhere. The consistently negative values of ζ for silica across all values of pH indicate that observed shifts in force-distance measurements from repulsive to attractive interactions between probe and surface can be attributed to a change in the sign of ζ the surface.

Results of ζ potential measurements of high-purity rutile suspensions in both 0.001 M and 0.100 M KCl solutions as a function of pH are presented in Figure 4.3. Both sets of data show an iep of roughly 5.3, which falls within the range of published values [22]. Moreover, the iep is shown to be independent of the concentration of KCl, confirming the role of the salt as a background electrolyte and not a source of potential-determining ions. This effect is confirmed in the AFM measurements presented in the next pages, which shows the rutile surfaces studied to interact with solvated K $^+$ and Cl $^-$ in a non-determining way.

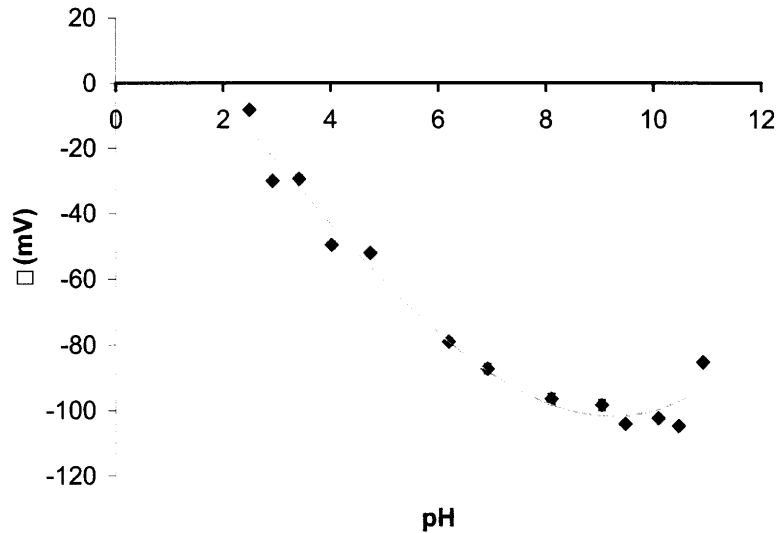


Figure 4.2. Characteristic ζ -pH dependence for silica spheres in 0.001 M KCl solution. The data indicates an isoelectric point of $\text{pH} \approx 2.0$, in general agreement with well-established values in the literature. The colloid probe tips used in AFM experiments are assumed to have a similar behavior, indicating that any change from repulsive to attractive force measurements observed in AFM experiments can be attributed to a change in sign of the double layer on the surface being measured.

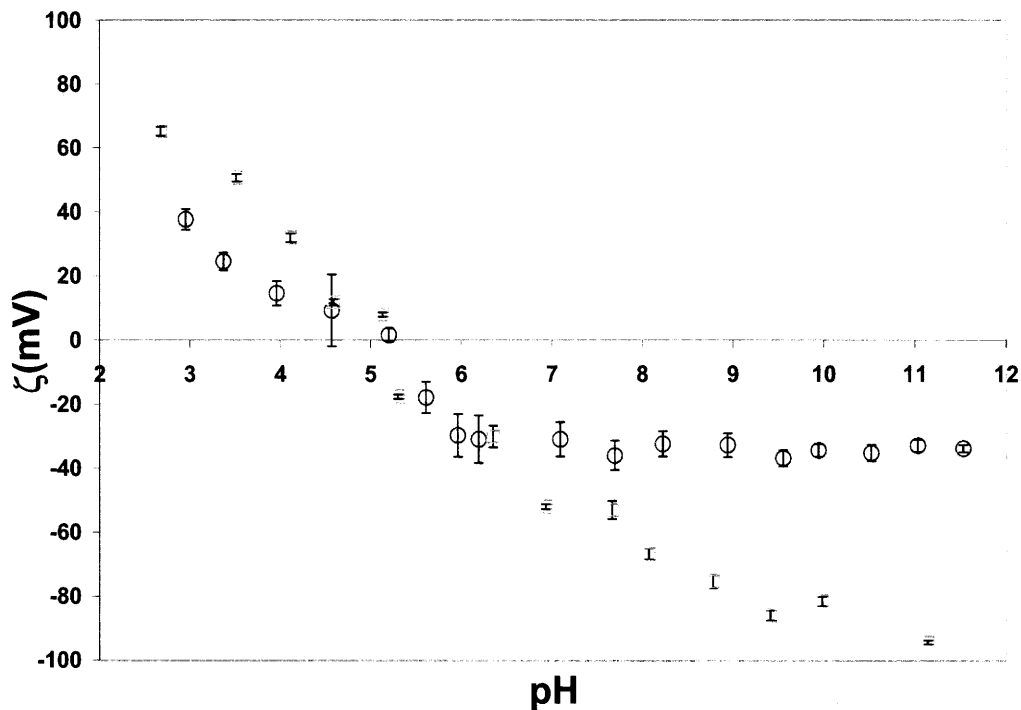


Figure 4.3. ZetaPALS measurements of the pH-dependent zeta potential of high-purity rutile powder in aqueous solutions of 0.001 M KCl electrolyte (squares) and 0.100 M KCl electrolyte (circles). Both data sets indicate that the isoelectric point of rutile is centered around $\text{pH} \approx 5.2$. The agreement between the measurements taken in solutions whose electrolyte concentration varies by two orders of magnitude indicates that neither K^+ nor Cl^- act as potential determining ions of rutile powder.

4.3.2 Surface Characterization

An XPS survey scan of a piranha-cleaned 110-oriented rutile surface is presented in Figure 4.4. All peaks visible in the survey can be attributed to titanium, oxygen, and adventitious carbon, the last of which is always present in XPS analyses of samples that have been exposed to anything but ultra-high vacuum conditions after cleaning. Broad surveys of all orientations studied were performed, and no significant differences in any of the spectra were observed. Moreover, no silicon signal was observed in any of the XPS spectra, indicating that cleaning and handling processes that made use of Pyrex and other glassware were not a source of silica contamination. This is an important point because adsorbed silica has been known to shift the iep to lower-than-expected values [23,24], and has previously served as the basis for arguments against the validity of observed differences in the isoelectric points of single crystalline surfaces in comparison with their polycrystalline and powder-based counterparts [25]. Contact-mode AFM images of piranha-cleaned rutile surfaces are shown in Figure 4.5. Samples of all three orientations used for this study demonstrate atomic-scale surface roughness, with root mean square (rms) roughness values on the order of 2 – 5 Å.

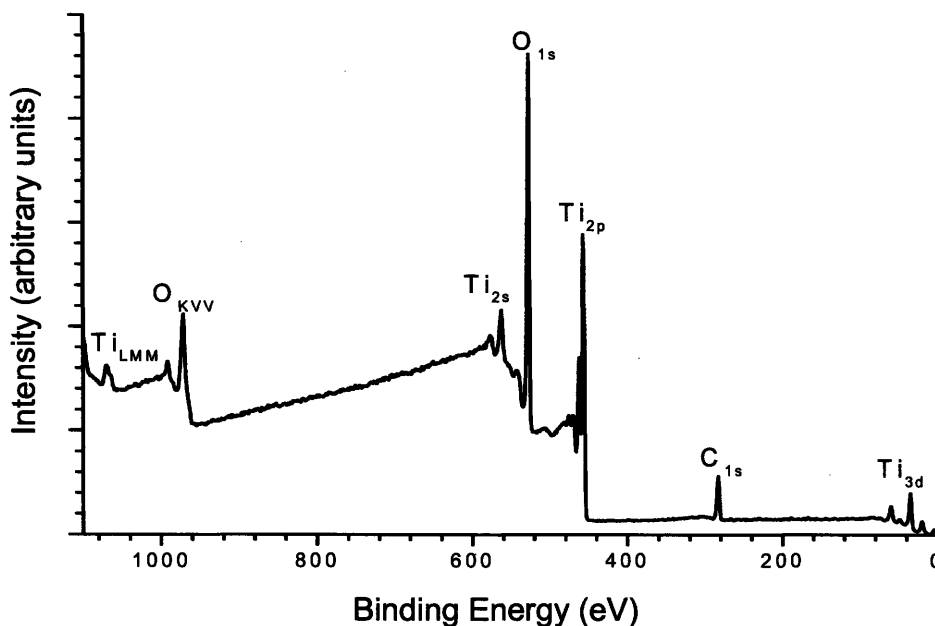


Figure 4.4. XPS survey scan of a (110)-oriented rutile surface after a 4:1 piranha clean. The survey was taken with monochromated Al K α radiation. All visible peaks are attributed to titanium, oxygen, and adventitious carbon, confirming the cleanliness of surfaces used in AFM experiments. No signal from silicon-containing contaminants, possible through handling samples in Pyrex beakers and other glassware, is observed.

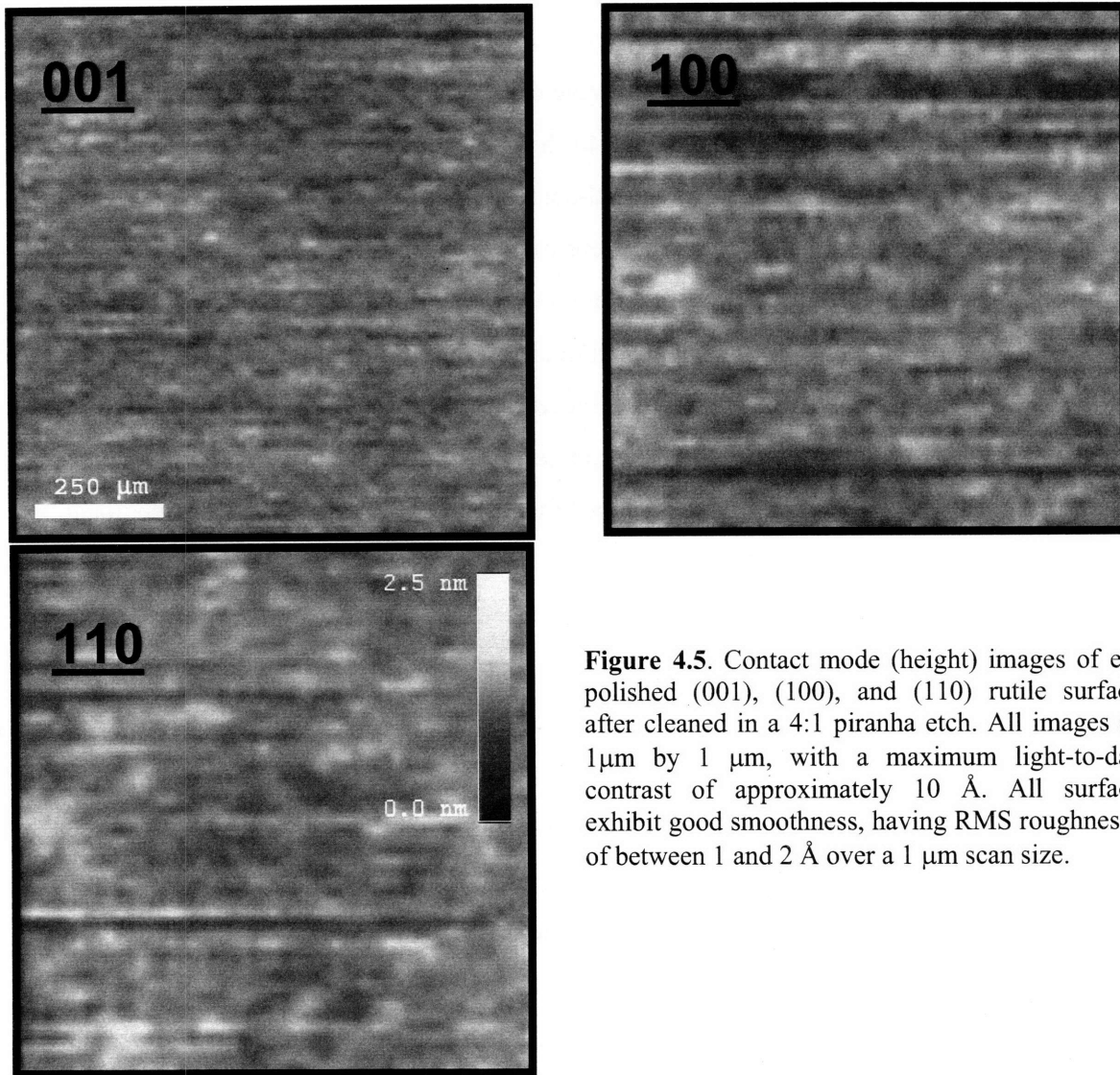


Figure 4.5. Contact mode (height) images of epi-polished (001), (100), and (110) rutile surfaces after cleaned in a 4:1 piranha etch. All images are $1\ \mu\text{m}$ by $1\ \mu\text{m}$, with a maximum light-to-dark contrast of approximately $10\ \text{\AA}$. All surfaces exhibit good smoothness, having RMS roughnesses of between 1 and $2\ \text{\AA}$ over a $1\ \mu\text{m}$ scan size.

4.3.3 Force Spectroscopy

4.3.3.1 General Criteria

The difficulty in generating repeatable force-distance measurements over a broad spectrum of specimens and solution conditions has been noted by other researchers [9]. A number of pitfalls await the scientist who attempts to perform a large quantity of experiments on nominally pristine surfaces over many hours. The characteristics of interactions between the probe tip and the surfaces of interest are susceptible to many external parameters whose impact cannot often be controlled and may, at times, go unnoticed until subsequent analysis of the data. Airborne particulate matter can adhere to the surfaces of crystals or probes, rendering a new geometry and unknown double layer characteristics to an experiment. The probe tip may be

positioned by over an optically undetectable surface defect of a crystal, resulting in measurements that are not necessarily representative of the majority of surface locales on a given sample. Excessive use of an AFM tip may lead to the dislodging of the silica sphere altogether, resulting in measurements between a tipless, gold-coated cantilever and a surface of interest.

Many of these experimental concerns were minimized by the use of common sense and clean, safe, laboratory practices, but the most potent guard against their potential to obfuscate results was to take multiple data points under identical conditions and to insist that all usable data to meet a handful of stringent criteria before acceptance. Specifically, data was taken at a minimum of three different locations on a given experiment under the same solution conditions, with approximately 20 force-distance curves generated in rapid succession at each location. These 20 curves were averaged to formulate a representative F-d curve at a specific location, as seen in Figure 4.6. Different positions on the surface were separated by at least 100 μm on large sample surfaces, and 50 μm on smaller ones. These data were averaged and compared for consistency, as shown in Figure 4.7.

AFM studies were also tested for repeatability. Figure 4.8 shows a comparison between force-distance measurements made on a (110) rutile surface in 0.001 M KCl electrolyte with two different tips, on two different days. Both data sets suggest comparable values for the iep of (110) rutile, and the magnitudes of measured interaction forces at similar pH values are generally similar to each other. These data also reflect the last major metric of reliability, which is the condition that their trends must reflect the expected behavior of a system across changes in solution conditions. Experiments shown in Figures 4.9, 4.10, and 4.11, for example, reflect a continual decline in the repulsive interactions between tip and surface with decreasing pH, as well as a shift to attractive interaction at sufficiently low pH. AFM experiments performed on a (110) surface where interaction force does *not* track well with pH, can be rejected as faulty. force curves at a lower pH show greater repulsive interactions than force curves taken previously at higher pH values. This suggests some change in the surface conditions of either the probe tip or the rutile surface, and the results of such an experiment are rejected for analysis of surface behavior.

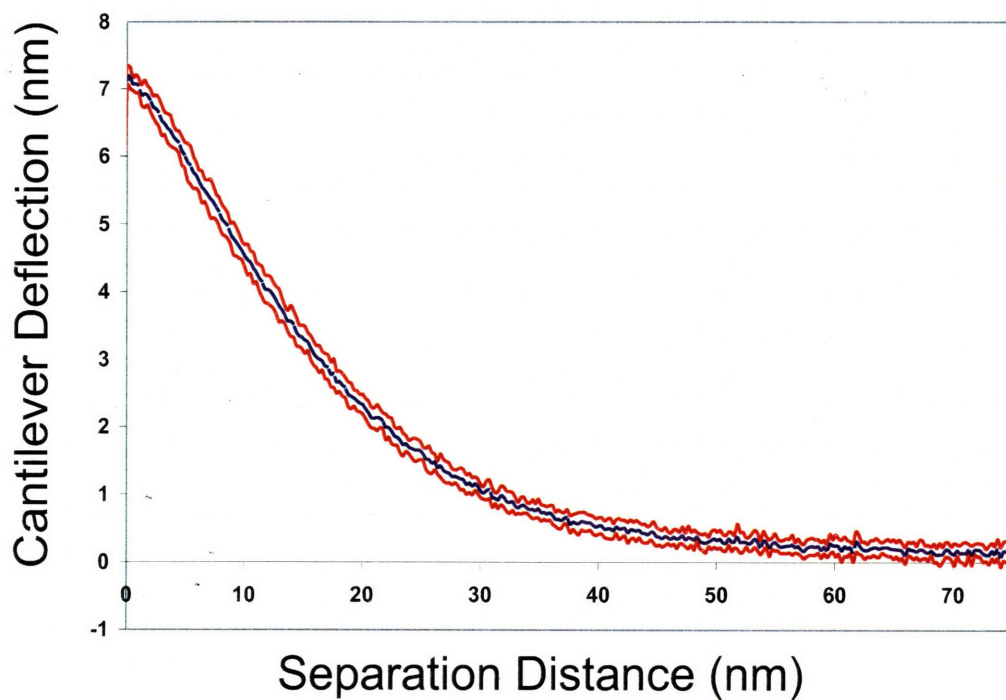
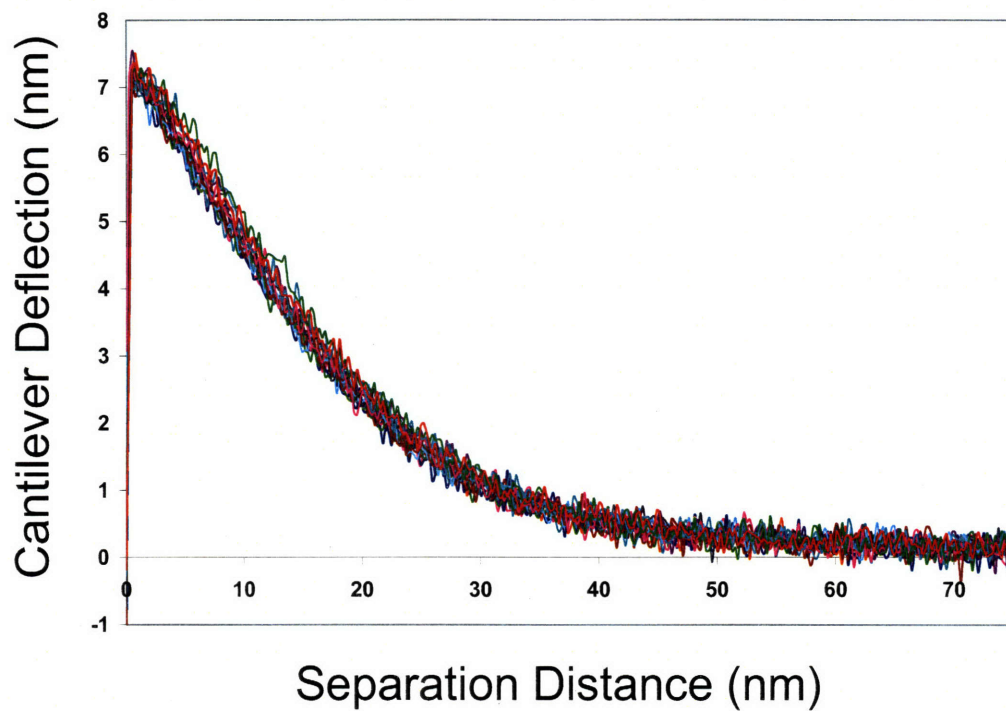


Figure 4.6. Transfer of approximately twenty raw force-distance curves at the same location on a sample surface to an averaged value. Error bars of one standard deviation from the mean value are represented by the red lines above and below the averaged data curve.

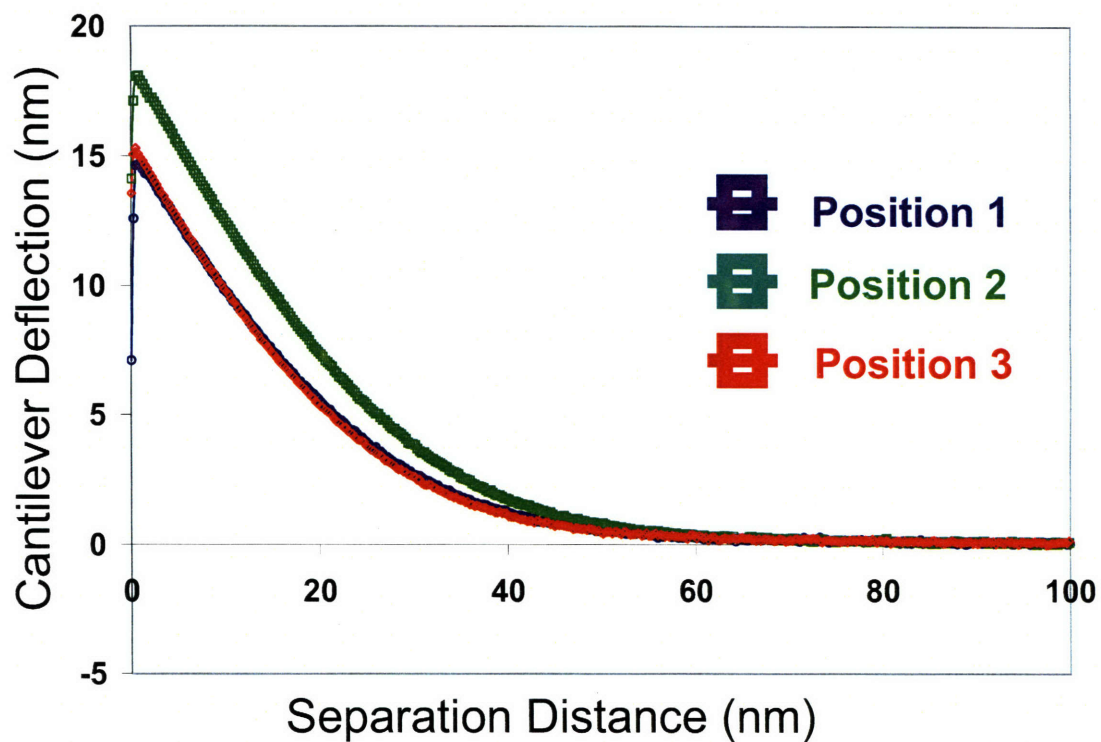


Figure 4.7. Averaged values of three force-distance measurements taken at different positions on the same surface under the same solution conditions. Each curve is a representative average akin to the curves shown in the bottom plot of Figure 4.6. Error curves have been removed for clarity.

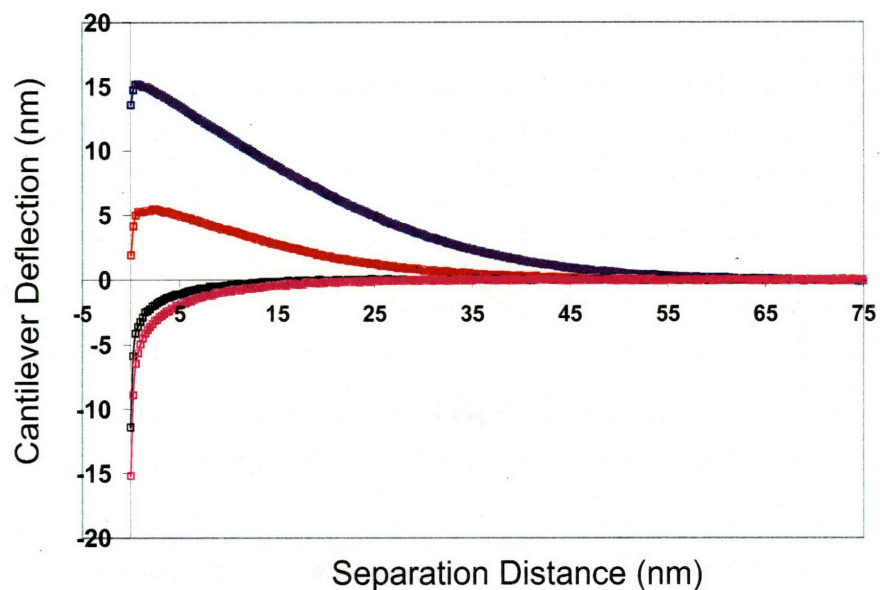
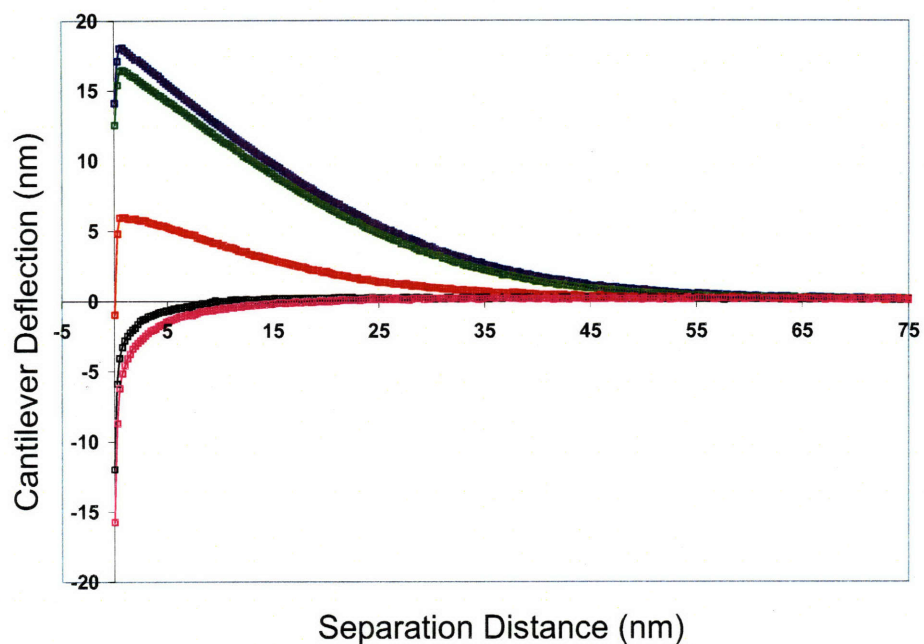


Figure 4.8. Interaction force as a function of separation distance for force spectroscopy measurements between two different probe tips and a (110) rutile surface in 0.001 M KCl solutions. Positive cantilever deflection denotes a repulsive force between surface and tip. The pH values of the solutions of each of the five curves are (from most repulsive to most attractive) 6.7, 6.3, 5.8, 5.5, 4.8, and 4.3 for the top data set, and values of 7.0, 5.5, 4.3, and 3.7 for the bottom set. Good agreement between the two experiments in both magnitude of deflection and lengthscale of interaction shows the repeatability of measurement.

4.3.3.2 Correlation of AFM Data to Streaming Potential Results

Force-distance measurements were performed on single crystalline sapphire surfaces with the same silica spheres used in experiments with rutile in order to demonstrate agreement in determination of the isoelectric point between AFM and streaming potential measurements. Samples of A-plane sapphire cut from samples used in previous streaming potential measurements were prepared as before and measured using the same techniques outlined above. Figure 4.8 shows the results of these proof-of-concept experiments. The force spectroscopy data in Figure 4.8a show a shift from repulsive to attractive tip-surface interactions between $\text{pH} \approx 6.0$ and $\text{pH} \approx 5.3$. The streaming potential data displayed in Figure 4.8b indicate that A-plane sapphire has an isoelectric point at a pH of approximately 5.5, indicating good general agreement between the two techniques.

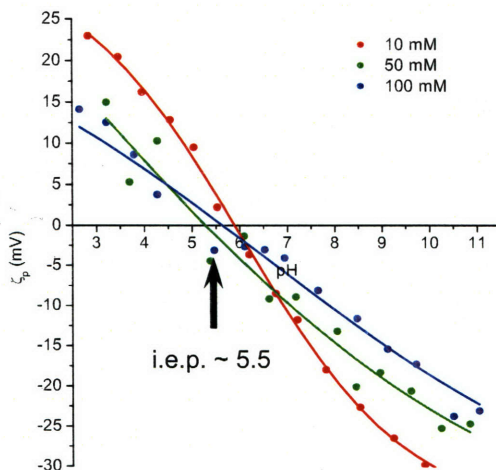
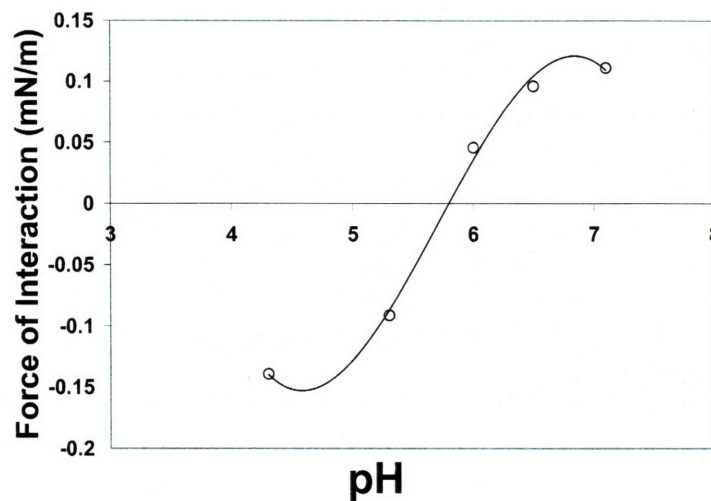


Figure 4.9. (a) The results of force-distance (above) and (b) streaming potential (left, from [8]) measurements of identically treated surfaces of A-plane sapphire. The shift from repulsive to attractive interactions in the AFM experiments occurs between $\text{pH} \approx 6.0$ and $\text{pH} \approx 5.3$. This correlates well to the established iep of $\text{pH} \approx 5.5$ for this orientation of sapphire, indicating that is a viable technique for measuring surface potential characteristics of a material. Trendlines have been added to guide the eye.

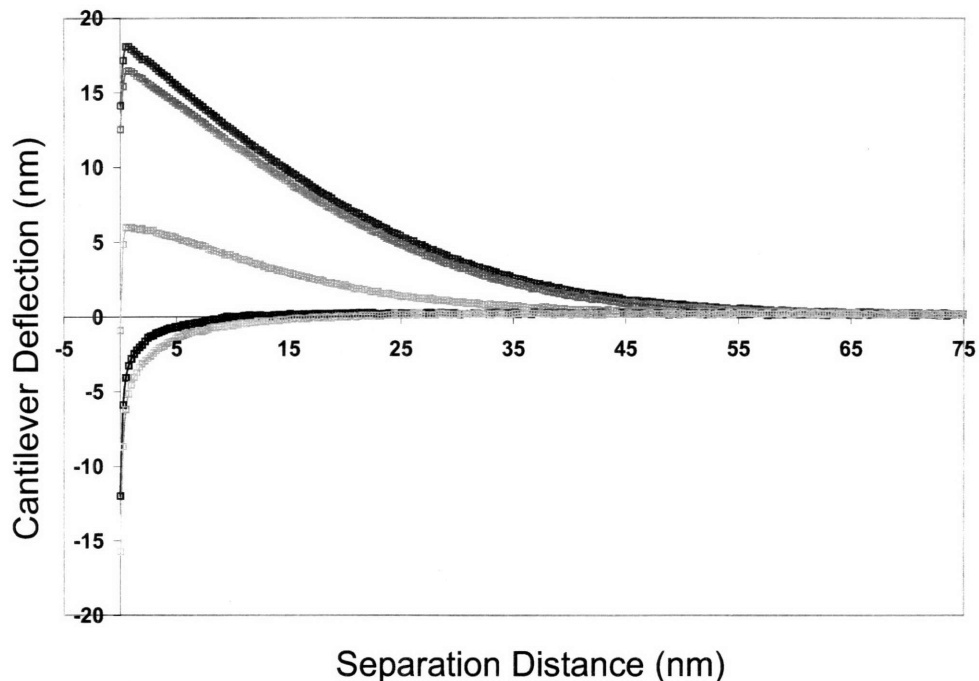


Figure 4.10. Interaction force as a function of separation distance for force spectroscopy measurements between a silica sphere and a (110) rutile surface in 0.001 M KCl solutions. Positive cantilever deflection denotes a repulsive force between surface and tip. The pH values of the solutions of each of the five curves are (from most repulsive to most attractive) 6.3, 5.8, 5.5, 4.8, and 4.3. The shift from repulsive to positive surface interactions indicates that the iep of this orientation of rutile lies between 5.5 and 4.8. Recent work using another technique (**Wesolowski**) identified the iep of the (110) surface as 4.8 ± 0.3 .

4.3.3.3 Force Spectroscopy Results of Rutile

Accepted force-distance data of 110, 100, and 001 rutile surfaces taken in 0.001 M KCl electrolyte solutions is presented in Figure 4.10, 4.11, and 4.12. These data were taken as one set of experiments performed with the same solution conditions and colloid probe tip. A comparison of the three data sets shows a clear distinction in the isoelectric points of the three surface orientations. The 100 surface, whose force-distance curves shift from repulsive to attractive between pH = 3.7 and pH = 3.2, exhibits the lowest isoelectric point of the three surfaces. The 001 surface, on the other hand, shows the same transition from repulsive to attractive interaction between pH = 5.8 and pH = 5.6, while the 110 surface transitions between pH = 5.6 and pH = 4.8.

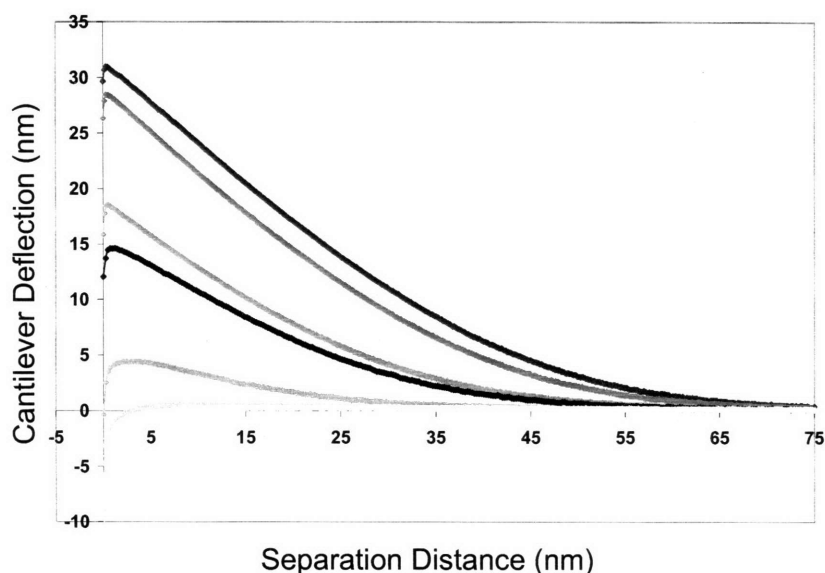


Figure 4.11. Interaction force as a function of separation distance for force spectroscopy measurements between a silica sphere and a (100) rutile surface in 0.001 M KCl solutions. Positive cantilever deflection denotes a repulsive force between surface and tip. The pH values of the solutions of each of the five curves are (from most repulsive to most attractive) 5.8, 5.5, 4.8, 4.3, 3.7, 3.2, and 2.8. The shift from repulsive to positive surface interactions indicates that the iep of this orientation of rutile lies between 3.7 and 3.2.

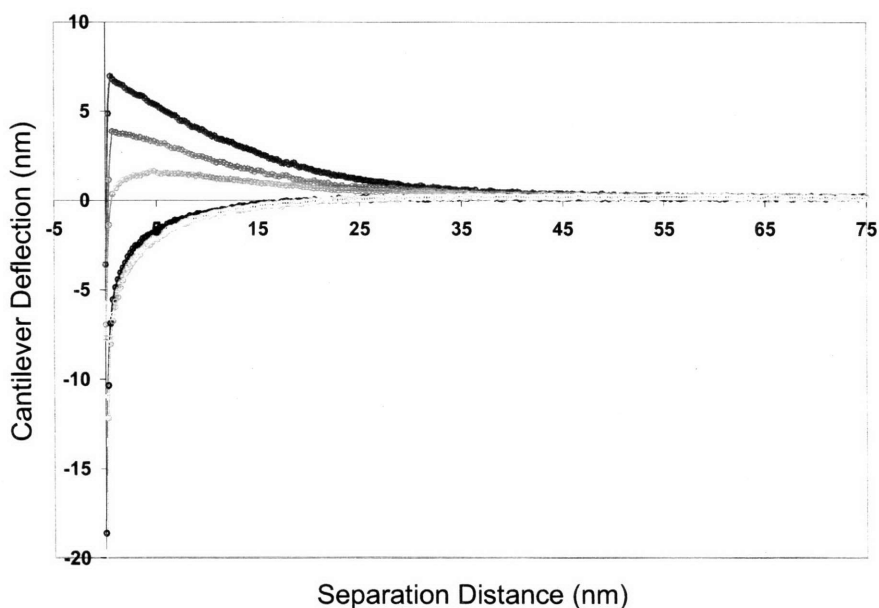


Figure 4.12. Interaction force as a function of separation distance for force spectroscopy measurements between a silica sphere and a (001) rutile surface in 0.001 M KCl solutions. Positive cantilever deflection denotes a repulsive force between surface and tip. The pH values of the solutions of each of the five curves are (from most repulsive to most attractive) 6.7, 6.3, 5.8, 5.5, 4.8, and 4.3. The shift from repulsive to positive surface interactions indicates that the iep of the (001) orientation of rutile lies between 5.8 and 5.5.

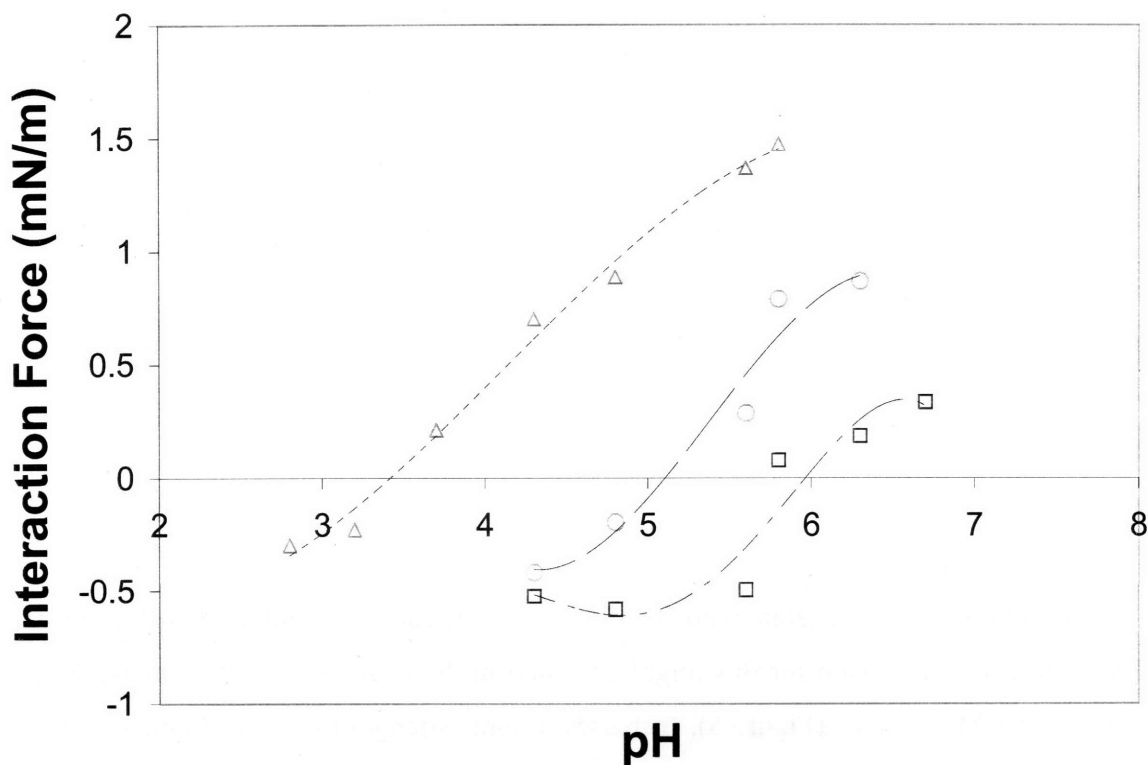


Figure 4.13. A plot of the maximum interaction forces measured on each of the three rutile surfaces in 0.001 M KCl as a function of solution pH. These values are determined by finding the peak, non-van der Waals interaction between surface and tip. The values of force are normalized by the approximate radius of the colloid probe. Trendlines are added to guide the eye, and highlight the sharp differences between the isoelectric points of the three orientations. Square data points correspond to the (001) surface, circles to (110), and triangles to the (100).

This relationship between surface orientation and isoelectric is emphasized in Figure 4.13, where force distance curves of all three samples are shown at the same pH. Measured values of the isoelectric point of both the (110) and (001) rutile surfaces are in good general agreement with the values determined by others [11,16], who also used other salts as background electrolytes.

The data shown in Figures 4.10, 4.11, and 4.12 also reveal a dramatic difference in the lengthscales over which the probe tip interacts with each of the three surfaces. Data for the (100) rutile surface reveals observable cantilever deflection in the repulsive regime when the separation distance between tip and surface is greater than 65 nm. The (110) surface displays observable tip-surface interaction at approximately 55 nm from the surface. Interactions between the (001) surface and the probe tip emerged at noticeably smaller separation distances, however, with observable repulsion of the tip appearing at distances of approximately 35 nm. Differences

in the lengthscale of interactions were more difficult to determine when attractive forces were observed between tip and surface.

Data in Figures 4.14 and 4.15 show Force-distance measurements for the (110) and (100) surfaces taken in 0.010 M KCl electrolyte solutions. The results reveal a shift from repulsive to attractive tip-surface interactions between similar pH levels in Figures 3 and 4, indicating that neither K^+ nor Cl^- is potential determining for any orientation of the rutile surface. Comparisons of Figure 3 to Figure 7 and Figure 4 to Figure 8 show decreases in both the magnitude and lengthscales of the interaction forces between tip and surface. These results are consistent with the expectation from DLVO theory that increases in ionic strength result in both reduced double layer thicknesses and values of ζ . This is also consistent with the measurements of ζ for rutile powders discussed earlier.

It was not possible to generate repulsive force-distance curves at similar pH values for the (001) rutile surface. The reason for this might be found in the relatively small repulsive forces observed in 0.001 M solutions (Figure 5). Increases in ionic strength to 0.010 M concentrations

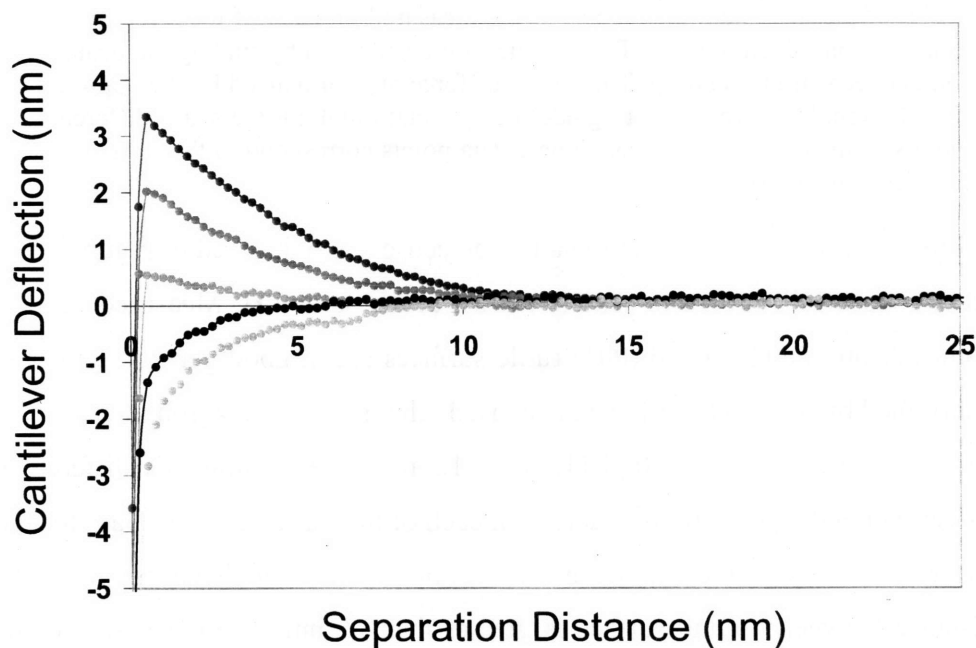


Figure 4.14. Force-distance measurements performed on a (110) rutile surface in 0.010 mM KCl solution. The curves, from most attractive to most repulsive, were taken in solutions with pH values of 6.6, 6.3, 5.5., 4.7, and 4.3. The shift from repulsive to attractive interactions between pH values of 5.5 and 4.7 is consistent with measurements performed in 0.001 mM KCl solutions, indicating that neither K^+ nor Cl^- acts as potential determining ions.

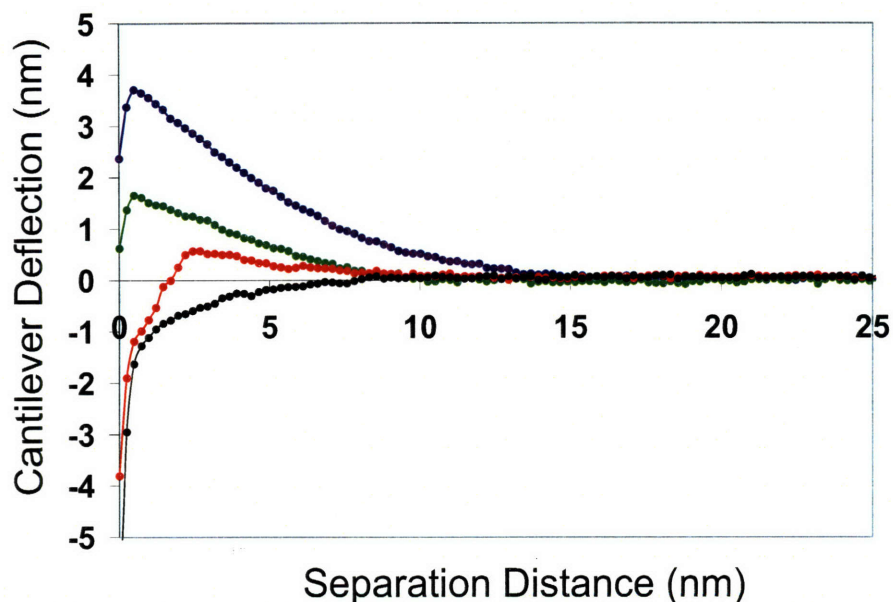


Figure 4.15. Force-distance measurements performed on a (100) rutile surface in 0.010 mM KCl solution. The curves, from most attractive to most repulsive, were taken in solutions with pH values of 4.7, 4.2, 3.8, and 3.3. The shift from repulsive to attractive interactions between pH values of 3.8 and 3.3 is consistent with measurements performed in 0.001 mM KCl solutions, indicating that neither K^+ nor Cl^- acts as potential determining ions.

may be sufficient to de-stabilize the tip-surface interactions with this surface to the point that repulsive interactions are no longer observable. Therefore, the attractive interactions observed in solutions of higher ionic strength but constant pH values do not necessarily indicate that Cl^- is potential determining with respect to the (001) surface.

4.3.4 X-Ray Photoelectron Spectroscopy

High-resolution XPS scans of both the 3d photoelectron peaks and the MMV Auger peaks of a monolayer of deposited Pd on each orientation of rutile are shown from a takeoff angle of 35° from normal incidence in Figure 4.16. The data show nearly overlapping Auger peaks of the Pd signal on all three orientations of rutile, but a significant difference of almost 0.6 eV between the photoelectron peaks of highest and lowest binding energies. The photoelectron peak of Pd on the (001) surface was observed to occur at the lowest binding energy, while the peak corresponding to the (110) surface occurred at a binding energy of approximately 0.15 eV higher, and the peak corresponding to the (100) surface appeared at nearly 0.35 eV higher energy

than that. Both the MAP for each of the three surfaces and the corresponding isoelectric point of each orientation are presented in Table 4.1.

A direct correlation between decreased isoelectric point and increased MAP is readily apparent, and the trend matches the one observed previously with Ir monolayers on sapphire surfaces [8]. One can interpret this correlation in trends between isoelectric point and MAP value by considering both phenomena from the viewpoint of a classic electrostatic model. The binding energy of atoms from a deposited monolayer should increase with an increase in net positive atomic charge of the substrate, which is considered to behave as a locus of Lewis acid sites. The substrate that binds electrons the tightest from the Pd monolayer is also the substrate that forms the strongest bonds to hydroxyl groups in aqueous solutions, requiring the addition of more hydrogen ions to change charge of the surface from negative to positive. Hence the relationship between MAP and iep.

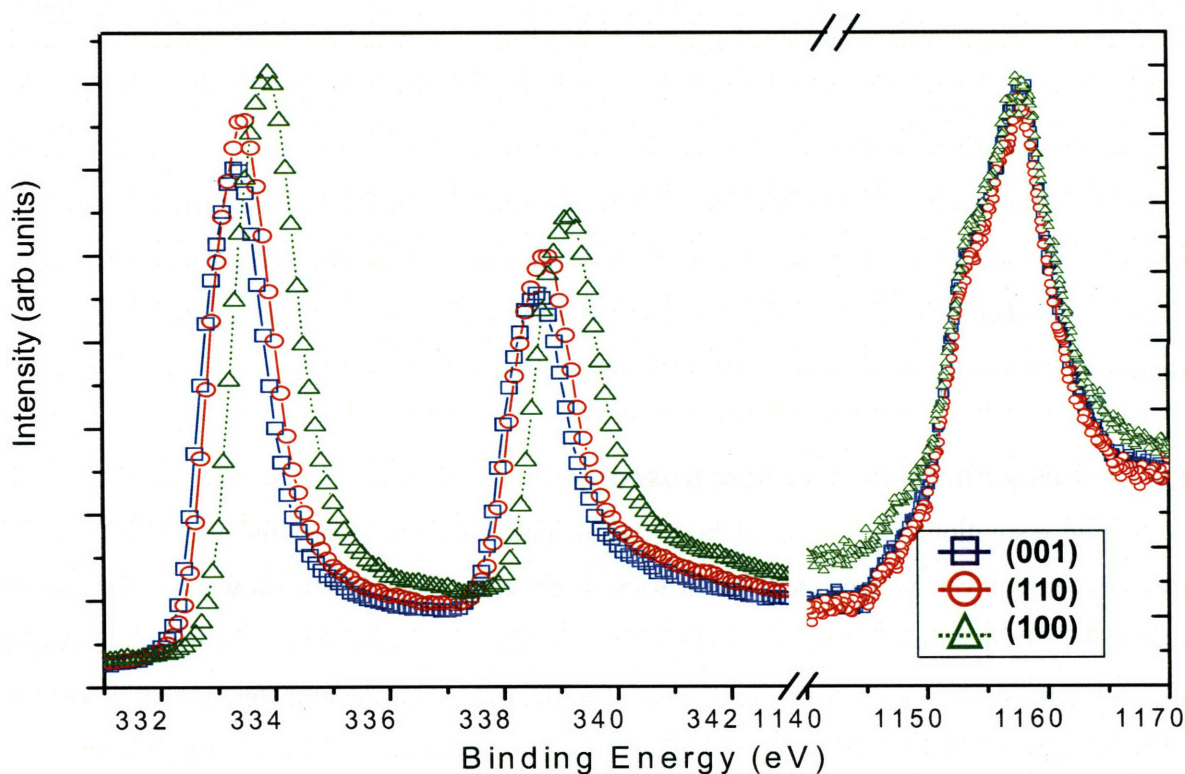


Figure 4.16. XPS data of the photoelectron (right side) and Auger (left side) peaks of an atomic monolayer of palladium deposited on the three surfaces of rutile investigated in this study. Auger peaks overlap well, but photoelectron peaks are offset by almost 0.6 eV. This difference in binding energy indicates a difference in the extent to which electrons from the Pd monolayer are bound to surface sites on their corresponding rutile substrates. These data were taken at a takeoff angle of 35 degrees from the surface normal. Square data points correspond to the (001) surface, circles to (110), and triangles to the (100).

Orientation	i.e.p Range	M.A.P.	Cation density (per nm²)
[100]	3.7 – 3.2	824.23	7.4
[110]	5.5 – 4.8	824.64	6.0
[001]	5.8 – 5.5	824.71	4.8

*Note that lower MAP values correspond to smaller differences between the binding energy of the photoelectron peak and the Auger peak. Because the Auger peak is always at a higher energy than the photoelectron peak, smaller MAP values therefore correspond to higher binding energies.

4.4 Discussion

The results of the force spectroscopy and XPS measurements presented above independently indicate a trend of varying surface acidity across crystal orientation. This behavior suggests a strong connection between the atomic structure of the surface and the observed differences in surface potential and colloidal interactions. Indeed, significant differences in the structure of each of the three surfaces are readily apparent, and their consideration is essential to a thorough analysis.

4.4.1 Structure of the (110) Rutile Surface

A schematic diagram of the (110) rutile structure is presented in Figure 4.17a. The unreconstructed surface contains two unique cationic positions, with alternating rows of five- and sixfold coordinated Ti sites running along the [001] direction. The surface also contains two different coordinations of oxygen sites. Threefold coordinated oxygen atoms occupy sites in the main plane of the surface, while twofold coordinated atoms are positioned in the bridging sites of the surface, above the sixfold coordinated Ti sites [26]. These atoms are depicted in light blue in Figure 4.17a. Surface relaxations in the (110) plane have been determined both theoretically [27-29] and with surface x-ray diffraction techniques [30]. Substantial downward relaxation of bridging oxygen atoms is observed, with smaller downward shifts in fivefold coordinated titanium atoms, and upward shifts in the sixfold Ti sites. Symmetric, in-plane movement of threefold coordinated oxygen atoms is also noted. The resulting surface morphology has been described elsewhere as having a “rumpled appearance” [26].

4.4.2 Structure of the (110) Rutile Surface

The (100) rutile surface is depicted schematically in 4.17b. This crystal face also contains both twofold and threefold oxygen sites, with the former positioned as a tilted analog to the bridging oxygen sites found on the (110) surface. The (100) face, however, is comprised entirely of fivefold coordinated titanium atoms. Surface energetic calculations [27, 31-33] predict significant relaxations of the titanium down into the surface, with lateral relaxations of both titanium and oxygen positions in opposite directions along $\langle 010 \rangle$, increasing the effective coordination of the fivefold coordinated titanium atoms [32]. The authors are unaware of any experimental data supporting these theoretical predictions. Lower coordination numbers have been associated with increased surface acidities before [8, 34-35]. Decreased atomic

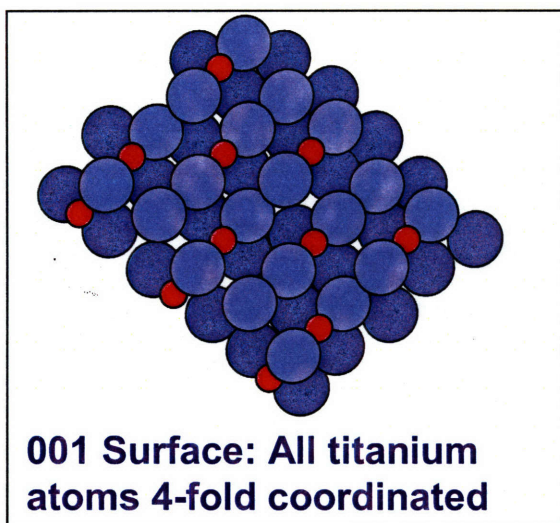
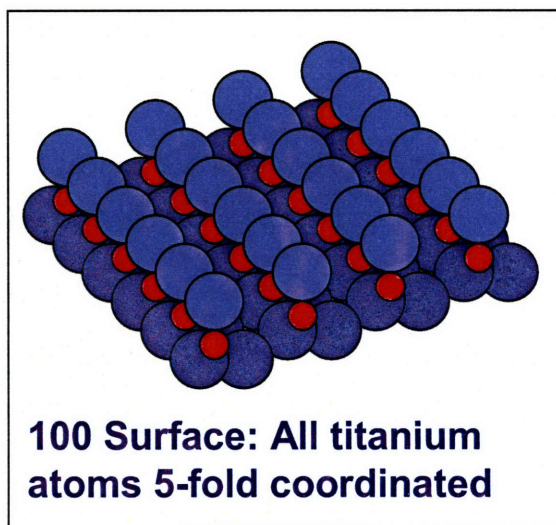
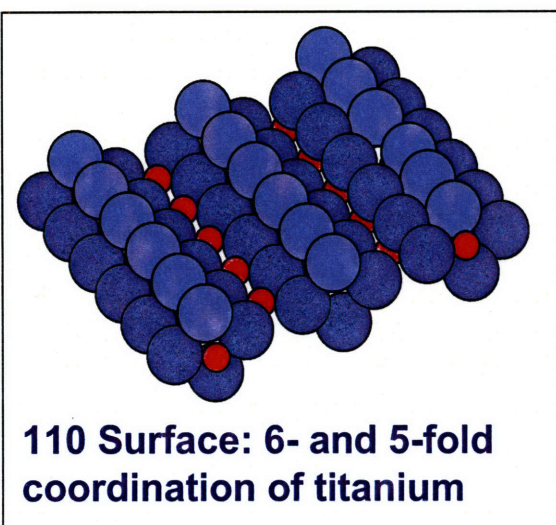


Figure 4.14. (Clockwise from top-left, a through c) Schematic diagrams of the idealized (110), (100), and (001) surfaces. Smaller red circles denote Ti positions, whereas larger blue circles represent O sites. The light-blue circles shown on the (110) and (100) surfaces represent twofold coordinated bridging O atoms. Structural differences between the three surfaces are discussed in the text.

coordination results in a greater number of dangling bonds and, for cationic positions, a corresponding increase in electron affinity. This may in part explain both the large shift in Pd XPS signals, as well as the significant difference in the isoelectric point of the (110) and (100) surface.

4.4.3 Structure of the (110) Rutile Surface

The (001) surface of rutile, however, does not readily fit the trend linking coordination number to surface acidity and isoelectric point. Shown in Figure 4.17c, this orientation of rutile is the least energetically stable surface of the three studied here [27, 31, 36-37]. Its ideal structure is comprised entirely of fourfold coordinated titanium sites and twofold coordinated oxygen sites, resulting in a higher number of broken bonds than both the (110) and (100) surfaces. The high surface energy of the (001) surface leads to theoretical predictions of large relaxations of surface Ti atoms towards the bulk, and lateral relaxation of surrounding O atoms [36]. Experimental data on the structure of the unreconstructed (001) surface is scant at best. LEED analysis has been performed on n-type surfaces [38], and AFM studies have been done on undoped, polished surfaces [39]. However, computational papers have argued that discrepancies between LEED data and theoretical treatments may be rooted in both poor long-range order of the experimental surface and the doping of the crystal, which has long been known to alter the electronic structure of the surface [36]. AFM data of polished surfaces lacks true atomic scale resolution, but the authors observed steps and terraces on the surface that were similar to features of (001) surfaces that were faceted with heat treatments [39]. These faceted structures, identified by LEED of annealed samples, have been assigned by researchers as having {011} and {114} indices. Both reconstructions were noted to shift the coordination number of many, but not all Ti sites from fourfold to fivefold, with sixfold coordinated positions emerging in the {114} reconstructions [37, 40-41]

Although a number of researchers have studied the relationship between annealing temperature and reconstruction of (001) surfaces [38-45], very little has been written about the structure of the unreconstructed surface. Given the high surface energy and number of dangling bonds on the surface, it is conceivable that mechanical polishing of the (001) provides enough energy for nanoscale facets to form on a polished surface, with ordering on a lengthscale too small for detection by most surface diffraction techniques. This possibility was suggested by

grazing-incidence X-ray adsorption fine structure (GI-XAFS) studies which noted that the roughness of polished, untreated (001) rutile samples was consistent with the presence of a high density of steps on the surface [46]. The likelihood of such reconstructions, coupled with the prediction of relaxations of surface sites from idealized positions, suggest that coordination numbers of atoms on the (001) rutile surface effectively higher than they may first appear.

These models may help explain the relatively high isoelectric point of the (001) surface in comparison to the other orientations studied here. Despite having the lowest coordination number for its cationic positions, strong relaxations and facile reconstruction energetics substantially increase the average coordination value. Furthermore, the exclusive presence of twofold coordinated oxygen sites on the ideal (001) surface, in contrast with a mixture of two- and threefold sites on the (110) and (100) surfaces, suggests that stronger and more numerous Lewis *base* sites exist on the (001) surface. This greater number of base sites would facilitate a stronger adsorption of solvated hydrogen ions to these positions. Turning the model of increased surface acidity corresponding to decreased isoelectric point on its head, the increased basicity of the (001) surface may be explained from increased quantity and strength of electron-donating oxygen positions on the surface.

The (001) surface of rutile is also the most “open” of the three surfaces under consideration, with a network of channels running in the $\langle 001 \rangle$ direction normal to this surface. These channels have a radius of approximately 0.8 Å, larger than the radius of Ti^{4+} ($\sim 0.6 \text{ \AA}$) [47]. These channels render the (001) surface the preferred orientation for rutile in electrochemical experiments, as the [001] direction is the crystallographic direction of highest conductivity [26]. Their presence may in part explain the smaller interaction distances and forces observed between the AFM tip and (001) surface relative to the other orientations studied. Increased conductivity on this surface could promote higher charge mobility, allowing the surface to maintain conditions closer to constant potential interactions. The (110) and (100) surfaces, by contrast, could be thought of as having less mobile surface charges that lead to force-distance interactions more closely resembling the interaction between two surfaces of constant charge. It may be that the bridging oxygen atoms and noted corrugated surface structure inhibits charge mobility across the surface, effectively locking charges in position as the probe tip approaches.

Cationic and anionic coordination number may not be the final word in explaining the observed anisotropy of the isoelectric points and MAPs of the rutile system. Pristine structures of

most oxide surfaces are not likely to exist in ambient conditions, as they are known to readily hydroxylate in the presence of even the slightest amounts of water. Rutile is no exception [48] and a number of studies have been carried out on the interaction between water molecules and rutile powders [49] and individual rutile surfaces [15-16, 50-55] under both ambient and UHV conditions. The hydration of rutile powders has been observed to result in the presence some hydroxyl groups believed to have a mildly acidic character [56-58].

4.4.4 Influence of Hydroxyl Groups on Surface Behavior

Generally speaking, the hydration of rutile surfaces is believed to result in the presence of two types of hydroxyl groups [52-53], as well as both weakly and strongly-adsorbed molecular H₂O [53]. The specifics of adsorption, however, have been shown to be a function of crystallographic orientation. Unfortunately, few comparative studies between orientations are known to exist, and none that involve the (001) surface. Work that studies the hydroxylation of specific rutile surfaces under non-UHV conditions [51,54] focuses exclusively on the (110) surface.

Work by Henderson [50] demonstrated significant differences in the adsorption of water on (110) and (100) rutile. Temperature-programmed desorption (TPD) studies revealed an intense peak in the signal of the (110) surface at ~275K, indicating the desorption of molecular water. The broader TPD signal of the (100) surface suggests the presence of a significant number of dissociated water molecules that form hydroxyl groups on the surface. These data are presented in Figure 4.18 (top), and the schematic of Henderson's proposed distinction between the two surfaces is shown in Figure 4.18 (bottom). As seen in the drawing, Henderson suggests that water molecules adsorbing on the planar, fivefold Ti sites on the (110) surface are not close enough to bridging oxygen atoms to allow a hydrogen-bonding interaction. The tilt of these sites on the (100) surface, however, permits interaction between the hydrogen atoms of adsorbed water and the twofold coordinated O atoms of the rutile surface. The result is the dissociation of

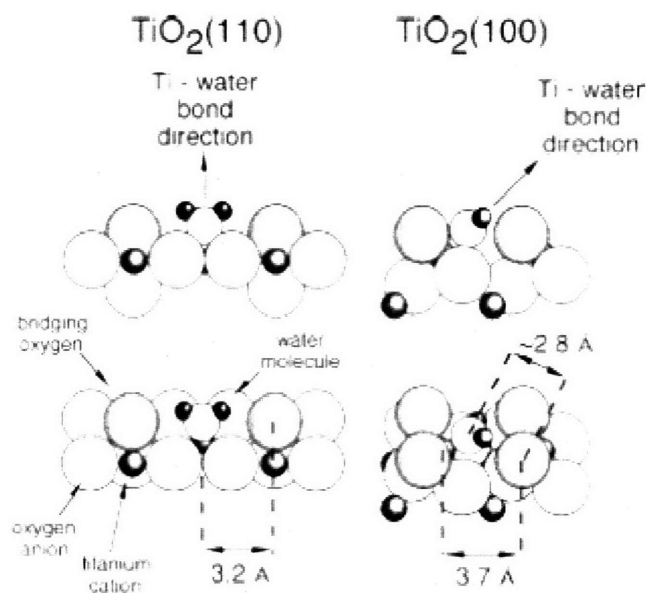
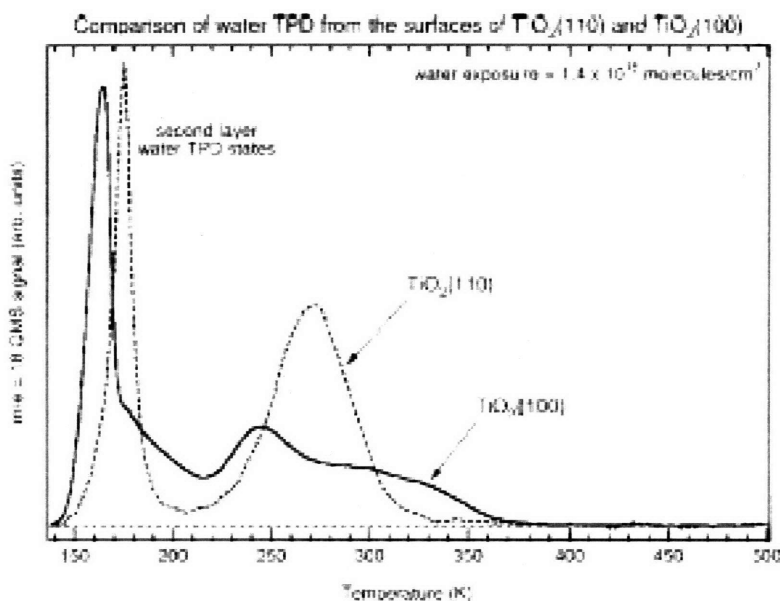


FIG. (*Top*) TPD studies by Henderson [50] on the (110) and (001) rutile surfaces. The relatively sharp peak of the $\text{TiO}_2(110)$ signal at $\sim 275\text{K}$ indicates the desorption of water molecules from the surface. The broad signal of the $\text{TiO}_2(100)$ surface with multiple shoulders indicates the desorption of water from several different surface states. Henderson argues that these data suggest that water molecules dissociate more readily on the (100) surface than on the (110) surface upon adsorption. (*Bottom*) Illustration explaining the differences in surface structure between the (110) and (001) rutile planes that lead to different mechanisms of water adsorption. The closer proximity of the twofold coordinated bridging O sites on the (110) surface (right) relative to those on the (110) surface allow for hydrogen bond formation between bridging O atoms and adsorbed water, promoting dissociation. This distance is too far to bridge on the (110) surface, and therefore only water molecules adsorbed at bridging vacancies are adsorbed dissociatively. Images taken from [50].

the water molecule and the formation of two hydroxyl groups on the surface. Both Henderson and Schaub [50,53] determined that on the (110) surface, vacant bridging O sites were essential to the dissociation of significant numbers of water molecules. This distinction between surfaces may serve as an explanation for the sharp contrast in isoelectric points between the (110) and (100) surfaces. Hydroxyl groups that are more tightly bound to a given surface would be expected to retain their positions at lower pH levels, resulting in a lowered iep. The XPS data presented here supports this hypothesis indirectly, as the shifted Pd signal indicates tighter binding to the (100) surface than to either the (110) or the (001) surface.

Unfortunately, no comparative studies involving the adsorption of water to the (001) surface are known to exist. However, the relative proximity of the binding energies of Pd monolayers on the (110) and (001) surfaces suggest that the two surfaces have similar electron affinities, which may explain their comparable iep. The role of bridging oxygen atom sites in the dissociation of water on other rutile surfaces may be an indicator of the differences in observed behavior of the (001) and (100) surfaces. Despite having the lowest (theorized) coordination number of cation surface sites, the absence of bridging sites on the (001) surface may result in fewer incidences of dissociative water adsorption. This, coupled with the previously-discussed presence of fewer cationic acid sites and more (and lower coordinated) basic site per unit area, may explain the large difference in surface acidity and isoelectric point between the (100) and (001) surface.

4.4.5 Connections between Single Crystalline and Powder Behavior

The results of streaming potential measurements on sapphire surfaces demonstrated a marked difference in the isoelectric points of each single crystal surface and the generally accepted range of values of the iep of conventional α -alumina powders. However, zetaPALS measurements of single crystalline alumina powders indicated an isoelectric point of approximately 3.8 [8]. The similarities between the calculated Wulff shape and the morphology of the suspended particles led to the conclusion that the large R-plane surfaces, present in the crystal habit, measured to have an iep of approximately 4.5, played a role in the significant reduction of the measured iep of the powder. Presumably, other orientations whose streaming potential was not measured (e.g., P-plane and S-plane) would also have sufficiently low iep values that would drive the value of the iep of particle down to its measured value.

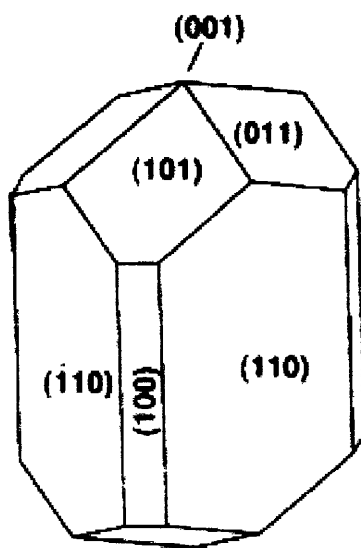


FIG. The equilibrium habit of a rutile crystal based on the Wulff construction and calculated surface energies of Ramamoorthy. The tetragonal structure of the rutile unit cell indicates that the (101) and (011) surfaces are not part of the {110} family. Regardless, the preponderance of the {110} surfaces is notable, given the close correlation between the measured isoelectric point of rutile powder (see FIG) and that of the (110) and (001) surfaces using AFM techniques. Image taken from [27].

Two of the three isoelectric points measured for the rutile surfaces in this work fall relatively close to the value indicated by zeta potential measurements of rutile powder. This may be related to the Wulff shape of rutile (from [27]), shown in Figure 4.19. The habit is dominated by the presence of (110) surfaces, and the measured value of the iep of the powder ($\text{pH} \approx 5.2$) is very close to the value determined for the (110) surface seen in the plot of ΔF vs. pH in Figure 4.13. The (100) surface, whose iep was measured to be substantially lower than both that of the powder and other orientations of rutile, constitutes a relatively small percentage of surface area as indicated by the Wulff shape.

4.5 Conclusions

Both XPS and AFM studies of a series of three different orientations of rutile show strong anisotropic behavior in measured surface acidity. The (100) surface, measured by AFM to have the lowest isoelectric point among the three orientations, was also determined by XPS to bind most strongly to a deposited monolayer of palladium, confirming the relationship between electron affinity measured *in vacuo* and surface acidity as manifested by iep. The (001) surface, by contrast, exhibited both the highest iep and the weakest binding of the Pd monolayer. The vast body of work on the structure and properties of various rutile surfaces provides some insights

into the atomic origins of this phenomenon. Surface acidity is seen as a function of the coordination number and areal density of both cationic and anionic surface sites, but may also be related to the stability and density of dissociated hydroxyl groups.

4.6 REFERENCES

- [1] N. Street, "The rheology of Kaolinite suspensions." *Aus J Chem* **9** (1956) 467
- [2] R.K. Schofield and H.R. Samson, "Flocculation of kaolinite due to the attraction of oppositely charged crystal faces." *Farad Discuss Chem Soc* **18** (1954) 135
- [3] R.M. Torres Sanchez, C. Volzone, E. Pereira, E.M. Curt, "Influence of the kaolin oxide composition in structural parameters and physiochemical properties." *J. Mater. Sci. Lett.* **9** (1990) 368
- [4] S. Assemi, J. Nalaskowski, J.D. Miller, and W.P. Johnson, "Isoelectric point of fluorite by direct force measurements using atomic force microscopy." *Langmuir* **22** (2006) 1403
- [5] J. Oberndorfer and B. Dobias, "Adsorption mechanism of anionic surfactants on sparingly soluble minerals." *Colloids Surf* **41** (1989) 69
- [6] K. Fa, T. Jiang, J. Nalaskowski, and J.D. Miller, "Interaction forces between a calcium dioleate sphere and calcite/fluorite surfaces and their significance in flotation." *Langmuir* **19** (2003) 10523
- [7] T. Hiemstra and W.H Van Riemsdijk, "Effect of different crystal faces on experimental interaction force and aggregation of hematite." *Langmuir* **15** (1999) 8045
- [8] R.J. Kershner, J.W. Bullard, and M.J. Cima, "Zeta potential orientation dependence of sapphire substrates." *Langmuir* **20** (2004) 4101
- [9] G.V. Franks and L. Meagher, "The isoelectric points of sapphire crystals and alpha-alumina powder." *Col Surf A* **214** (2003) 99
- [10] T. Hiemstra, P. Venema, and W.H Van Riemsdijk, "Intrinsic proton affinity of reactive surface groups of metal (hydr)oxides: The bond valence principle." *J Col Interf Sci* **184** (1996) 680
- [11] I. Larson, C.J. Drummond, D.Y.C. Chan, and F. Grieser, "Direct force measurements between TiO₂ Surfaces." *J Am Chem Soc* **115** (1993) 11885

- [12] K. Hu, F.-R. Fan, A.J. Bard, and A.C. Hillier, "Direct measurement of diffuse double-layer forces at the semiconductor/electrolyte interface using an atomic force microscope." *J Phys Chem B* **101** (1997) 8298
- [13] A. Feiler, P. Jenkins, and J. Ralston, "Metal oxide surfaces separated by aqueous solutions of linear polyphosphates: DLVO and non-DLVO interaction forces." *Phys Chem Chem Phys* **2** (2000) 5678
- [14] Z. Zhang, P. Fenter, L. Chang, N.C. Sturchio, M.J. Bedzyk, M.L. Machesky, and D.J. Wesolowski, "Model-independent X-ray imaging of adsorbed cations at the crystal-water interface." *Surface Science* **554** (2004) L95
- [15] Z. Zhang, P. Fenter, L. Cheng, N.C. Sturchio, M.J. Bedzyk, M. Předota, A. Bandura, J.D. Kubicki, S.N. Lvov, P.T. Cummings, A.A Chialvo, M.K. Ridley, P. Bénézeth, L. Anovitz, D.A. Palmer, M.L. Machesky, and D.W. Wesolowski, "Ion adsorption at the rutile-water interface: Linking molecular and macroscopic properties." *Langmuir* **20** (2004) 4954
- [16] J.P. Fitts, M.L. Machesky, D.J. Wesolowski, X. Shang, J.D. Kubicki, G.W. Flynn, T.F. Heinz, and K.B. Eisenthal, "Second-harmonic generation and theoretical studies at the water/ α -TiO₂(110) interface." *Chem Phys Lett* **411** (2005) 399
- [17] I. Larson, C.J. Drummond, D.Y.C. Chan and F. Grieser, "Direct force measurements between silica and alumina." *Langmuir* **13** (1996) 2109
- [18] L.H. Allen and E. Matijevic, "Stability of colloidal silica, I. Effect of simple electrolytes." *J Col Interf Sci* **31** (1969) 287
- [19] J. Depasse and A. Watillon, "The stability of amorphous colloidal silica." *J Col Interf Sci* **30** (1970) 430
- [20] J.E. Sader, J.W.M. Chon, and P. Mulvaney, "Calibration of rectangular atomic force microscope cantilevers." *Rev Sci Instrum* **70** (1999) 3967
- [21] J.E. Sader, J. Pacifico, C.P. Green, P. Mulvaney, "General scaling law for stiffness measurement of small bodies with applications to the atomic force microscope." *J Appl Phys* **97** (2005) 124903
- [22] M. Kosmulski, "The significance of the difference in the point of zero charge between rutile and anatase." *Adv Coll Interf Sci* **99** (2002) 255
- [23] D.N. Furlong, P.A. Freeman, and A.C.M. and Lau, "The adsorption of soluble silica at solid-aqueous solution interfaces. I. Leaching from glass—an electrokinetic study." *J Colloid Interf Sci* **80** (1981) 20
- [24] J.S. Moya, J. Rubio, and J.A. Pask, "Electrokinetic behavior of silica-bearing alumina surfaces." *Ceramic Bull* **59** (1980) 1198

- [25] M. Kosmulski, "Comment on 'Point of zero charge of a corundum-water interface probed with optical second harmonic generation (SHG) and atomic force microscopy (AFM): New approaches to oxide surface charge' by A.G. Stack, S.R. Higgins, and C.M. Eggleston." *Gecochim Cosmochim Acta* **65** (2001) 3055
- [26] U. Diebold, "The surface science of titanium dioxide." *Surf Sci Rep* **48** (2003) 53
- [27] M. Ramamoorthy and D. Vanderbilt, "First-principles calculations of the energetics of stoichiometric TiO₂ surfaces." *Phys Rev B* **49** (16721)
- [28] N.M. Harrison, X.G. Wang, J. Muscat, and M. Scheffer, "The influence of soft vibrational modes on our understanding of oxide surface structure." *Faraday Discuss, Chem Soc* **114** (1999) 305
- [29] S.P. Bates, G. Kresse, and M.J. Gillan, "A systematic study of the surface energetics and structure of TiO₂(110) by first-principles calculations." *Surface Science* **385** (1997) 386
- [30] G. Charlton, P.B. Howes, C.L. Nicklin, P. Steadman, J.S.G. Taylor, C.A. Muryn, S.P. Harte, R. McGrath, D. Norman, T.S. Turner, and G. Thornton, "Relaxation of TiO₂(110)-(1x1) using surface x-ray diffraction." *Phys Rev Lett* **78** (1997) 495
- [31] P. Reinhardt and B.A. Heß, "Electronic and geometrical structure of rutile surfaces." *Phys Rev B* **50** (1994) 12015
- [32] J. Muscat, N.M. Harrison, and G. Thornton, "Effects of exchange, correlation, and numerical approximations on the computed properties of the rutile TiO₂(100) surface." *Phys Rev B* **59** (1999) 2320
- [33] P.J.D. Lindan, N.M. Harrison, J.M. Holender, M.J. Gillan, and M.C. Payne, "The TiO₂(100)-(1x3) reconstruction: Insights from *ab initio* calculations." *Surface Science* **364** (1996) 431
- [34] S. Akhter, K. Lui, and H.H. Kung, "Comparison of the chemical properties of the zinc-polar, oxygen-polar, and the nonpolar surfaces of zinc oxide." *J Phys Chem* **89** (1984) 1958
- [35] J.M. Vohs and M.A. Barteau, "Structure sensitivity and selectivity of proton abstraction from alkynes on the polar surfaces of zinc oxide." *J Phys Chem* **91** (1987) 4766
- [36] J. Muscat and N.M. Harrison, "The physical and electronic structure of the rutile (001) surface." *Surface Science* **446** (2000) 119
- [37] R.H. Tait and R.V. Kasowski, "Ultraviolet photoemission and low-energy-electron diffraction studies of TiO₂ (rutile) (001) and (110) surfaces." *Phys Rev B* **20** (1979) 5178

- [38] C.G. Mason, S.P. Tear, T.N. Doust, and G. Thornton, "A low-energy electron-diffraction analysis of the structure of the titanium dioxide (001) surface." *J Phys Cond Matt* **3** (1991) S97
- [39] B.A. Watson and M.A. Barteau, "Atomic-force microscopy imaging of TiO₂ surfaces active for C-C bond formation reactions in ultrahigh-vacuum." *Chem Mater* **6** (1994) 771
- [40] L.E. Firment, "Thermal faceting of the rutile TiO₂(001) surface." *Surface Science* **116** (1982) 205
- [41] M.A. Barteau, "Organic reactions at well-defined oxide surfaces." *Chem Rev* **96** (1996) 1413
- [42] G.E. Poirier, B.K. Hance and J.M. White, "Identification of the facet planes of phase I TiO₂(001) rutile by scanning tunneling microscopy and low-energy electron diffraction." *J Vac Sci Technol B* **10** (1992) 6
- [43] K.-i Fukui, R. Tero, and Y. Iwasawa, "Atom-resolved structures of TiO₂(001) surface by scanning tunneling microscopy." *Jpn J Appl Phys* **40** (2001) 4331
- [44] H. Nörenberg, F. Dinelli, and G.A.D. Briggs, "Network-like $(7\sqrt{2} \times \sqrt{2})R45^\circ$ surface reconstruction on rutile TiO₂(001) by non-equilibrium self-organization." *Surface Science* **436** (1999) L635
- [45] H. Nörenberg, F. Dinelli, and G.A.D. Briggs, "The surface structure of TiO₂(001) after high temperature annealing studied by AFM, STM, and optical microscopy." *Surface Science* **446** (2000) L83
- [46] S.N. Towle, G.E. Brown, Jr., and G.A. Parks, "Sorption of Co(II) on metal oxide surfaces. I. Identification of specific binding sites of Co(II) on (110) and (001) surfaces of TiO₂ (Rutile) by grazing-incidence XAFS spectroscopy." *J Coll Interf Sci* **217** (1999) 299
- [47] H.O. Finklea, ed., "Semiconductor Electrodes." Elsevier, New York, 1988
- [48] H.P. Boehm, "Acidic and basic properties of hydroxylated metal oxide surfaces." *Discuss Farad Soc* **52** (1971) 264
- [49] M. Primet, P. Pichat, and M.-V. Mathieu, "Infrared study of the surface of titanium dioxides. I. Hydroxyl groups." *J Phys Chem* **75** (1971) 1216
- [50] M.A. Henderson, "Structural sensitivity in the dissociation of water on TiO₂ single-crystal surfaces." *Langmuir*, **12** (1996) 5093
- [51] M. Předota, A. V. Bandura, P.T. Cummings, J.D. Kubicki, D.J. Wesolowski, A.A. Chialvo, and M.L. Machesky, "Electric double layer at the rutile (110) surface. 1. Structure of

- surfaces and interfacial water from molecular dynamics by use of *ab initio* potentials.” *J Phys Chem B* **108** (2004) 12049
- [52] D.M. Griffiths and C.H. Rochester, “Infrared study of the adsorption of water on to the surface of rutile.” *J Chem Soc Farad Trans I* **73** (1977) 1510
- [53] R. Schaub, P. Thostrup, N. Lopez, E. Lægsgaard, I. Stensgard, J.K. Nørskov, and F. Besenbacher, “Oxygen vacancies as active sites for water dissociation on rutile TiO₂(110).”
- [54] R.L. Kurtz, R. Stockbauer, and T.E. Madey, E. Román, and J.L. De Segovia, “Synchrotron radiation studies of H₂O adsorption on TiO₂(110).” *Surface Science* **218** (1989) 178
- [55] V.E. Henrich and R.L. Kurtz, “Surface electronic structure of TiO₂: Atomic geometry, ligand coordination, and the effect of adsorbed hydrogen.” *Phys Rev B* **23** (1981) 6280
- [56] B. Erdem, R.A. Hunsicker, G.W. Simmons, E.D. Sudol, V.L. Dimonie, and M.S. El-Aasser, “XPS and FTIR surface characterization of TiO₂ particles used in polymer encapsulation.” *Langmuir* **17** (2001) 2664
- [57] L. Ferretto and A. Glisenti, “Surface acidity and basicity of a rutile powder.” *Chem Mater* **15** (2003) 1181
- [58] M. Primet, P. Pichat, and M.-V. Mathieu, “Infrared study of the surface of titanium dioxides. II. Acidic and basic properties.” *J Phys Chem* **75** (1971) 1221

Chapter 5: Photoinduced changes in EDL Properties of Rutile Surfaces

5.1 Introduction

The photoresponsive properties of both the rutile and anatase structures of TiO₂ are well-known, with early work examining the generation of current and photolysis of water on n-type rutile surfaces with ultraviolet irradiation (UV) [1]. The discovery has fostered over three decades of work on utilizing the photoactivity of both rutile and anatase for a variety of applications ranging in scope from the photocatalysis of specific chemical reactions [2-4], to use in solar power technologies [5-7], to the light-induced adsorption of specific compounds [8-9]. This phenomenon is related to the excitation of electrons across the ~3.0 eV titania bandgap [10], which generates electron-hole pairs that can participate in oxidative and reductive reactions at the surface.

The dynamics of the photocatalytic behavior of TiO₂ are complex, as photogenerated carrier pairs are believed to interact with each other, with ambient molecular species, and with specific surface sites that can alter the properties of the TiO₂ interface [11]. This creates an array of structural and electronic changes to surface states that cannot necessarily be decoupled. The photosensitive behavior of various polymorphs of TiO₂ has been investigated sparingly with regard to the electroosmotic properties of TiO₂ suspensions. Variations in electrophoretic mobility have been observed [12-13] as a function of UV exposure. More recently, work has been done [14] to modulate electroosmotic flow rates in microfluidic cells with this capability. Differences in flow were observed between microchannels coated with a TiO₂ film that were utilized in darkness and ones exposed to UV. The work represents the first effort to capitalize on the externally-tunable properties of TiO₂ to control an electrokinetic phenomenon.

Other work with TiO₂ surfaces observed significant changes in the wetting properties of the surface as a function of UV irradiation. The exposure of surfaces to UV dramatically reduced the wetting angle of water droplets, indicating a shift from a hydrophobic surface to an extremely hydrophilic surface. This behavior has been seen in both rutile and anatase, and in both single crystals of various orientations and crystalline and amorphous thin films [15-17]. The researchers argued that the process functioned separately from the conventional photoactive behavior of TiO₂, stressing the generation of oxygen defects on the surface associated with UV irradiation as a means of altering the wetting properties. These structural changes facilitate the adsorption of

water molecules which can dissociate more readily at vacancies to hydroxylate the surface. The hydroxyl groups, in turn, enable hydrogen bonding to ambient water molecules and promote complete wetting.

Recent work, however, questions the validity of the model of defect-driven changes in hydrophilicity, instead attributing the UV-induced shift to a change in the concentration of adsorbed organic species [18-20]. This attribution is rooted in findings of UHV and controlled-atmosphere studies where adsorption of water molecules [19] or the measured wetting angle [20] on pristine (i.e., carbon-free) surfaces was unaffected by the presence or absence of UV radiation. Adsorption and wetting angle were observed to change with a UV stimulus, however, when specified doses of organic molecules were added to the surface.

Changes in hydrophilicity and surface potential are clear indicators that significant changes in colloid behavior are also happening upon exposure to UV. The work in this chapter aims to quantify this effect as a function of crystallographic orientation. Force-distance measurements were performed with an AFM on multiple crystal surfaces of rutile, and comparisons were made for each orientation before and after its exposure to UV. Photoinduced changes were observed in the double layer interactions between tip and surface, as evident in extension curves taken during AFM measurements. Changes in adhesive forces between tip and surface were also found upon analysis of the retracting AFM data. The results suggest that significant changes in the colloidal behavior of TiO₂ surfaces can be achieved through UV irradiation, and may be a viable method of directed assembly.

5.2 Materials and Methods

Many of the same samples, solutions, and preparation techniques described in the previous chapter were employed in this study as well. Rutile crystals of the same three orientations were purchased from the same vendor, aqueous solutions containing potassium chloride as the background electrolyte were prepared with the same reagents, and silica-tipped colloid probes (e.g., Figure 4.1) were purchased from the same supplier. All probes used in these studies, however, had a spring constant of 0.12 N/m.

Force-distance measurements between rutile surfaces and a colloidal probe tip were made under similar conditions to those outlined in the previous chapter. All measurements discussed in

this chapter, however, were performed on the same Digital Instruments Dimension 3100 microscope and Nano IV controller used in a portion of studies described in the previous chapter.

Much remains unknown about the photoresponsive properties of rutile surfaces, including the length of time that any effects of UV illumination have on a given surface. This uncertainty created a significant obstacle in trying to make comparisons between surface orientations in addition to between irradiated and non-irradiated surface of a given orientation. Other uncertainties in the experimental setup, such as changes in probe tip characteristics and surface cleanliness over time, made it impossible to correlate AFM measurements to differences between three orientations probed with the same tip and exposed to/shielded from UV for the same amounts of time.

The problem is greatly simplified by focusing instead on only the differences between a specific rutile surface with and without exposure to UV irradiation. This is achieved by cutting a 10 x 10 mm² sample of a given orientation into two similarly sized pieces on a conventional diesaw (Disco). The samples are then cleaned in a piranha etch simultaneously, with great care taken to make certain that neither piece has turned over, which could result in the comparison of two surfaces with slightly differing off-axis polishes. Both samples are then stored in dark, and force-distance measurements are made under identical solution conditions as a check that initial (pre-UV) behavior between tip and surface is identical for both samples.

The surfaces are then rinsed thoroughly in deionized water, and one is stored in darkness while the other is placed beneath an intense 3000 mW (output) ultraviolet lamp (make) for 10 minutes. Force-distance measurements are made on the surface of the UV-irradiated specimen under the same solution conditions as before. The control sample is also re-measured to ensure that any observed changes are associated with UV irradiation and not with ambient contamination of adventitious carbon or other potential pollutants. The solution is then changed to a solution of slightly decreased pH, and the cycle is repeated, with the UV-irradiated sample measured once, exposed to UV for 10 additional minutes, and measured once again. The control sample is only measured once at each pH level.

5.3 Results

5.3.1 EDL Interactions of the Rutile (100) Surface

Force distance curves at $\text{pH} = 6.8$ of both the (100) surface stored in dark and the (100) surface exposed to UV, but prior to UV exposure, show good agreement with each other, with comparably large repulsive interactions between tip and surface on both samples. These data are a good indication that the two surfaces, which were cut from the same original sample and have been treated under the same processing steps prior to use in force-distance measurements, do indeed exhibit the same behavior and can therefore be assumed to track similarly across changes in solution conditions excepting the fact that one surface will be exposed to UV and the other will not. A comparison of the force-distance curves of the two surfaces at the same pH and after one surface has been exposed to UV is shown in Figure 5.1. A slight decline in the cantilever deflection is observed when comparing the two deflection curves.

This differential becomes more evident in Figure 5.2, where the F-d curves of the two surfaces are taken at $\text{pH} = 5.6$, and prior to a second exposure of the same rutile surface to additional UV. A clear distinction is apparent between the two surfaces, and the surface stored in dark shows a far stronger repulsive interaction with the silica probe than the surface exposed to UV. Further exposure to UV, however, does not appear to have a significant effect on EDL characteristics. Figure 5.3 compares the F-d curves at $\text{pH} = 5.5$ of the UV-exposed (100) surface before and after 10 additional minute of irradiation. Differences between the two are well within the range of experimental error, and the consistency between them suggests that additional exposure of the (100) surface to UV does not influence behavior.

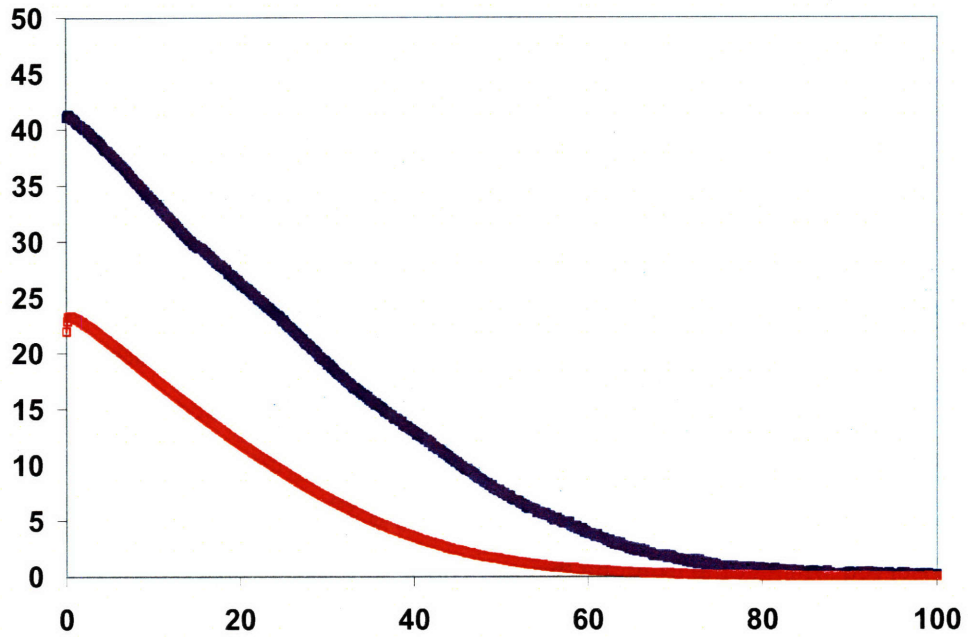


Figure 5.2 Comparison between the force-distance curves of two (100) rutile surfaces at a pH of 5.6. The blue (top) curve is that of a sample stored in darkness between runs, whereas the red curve represents deflection data of a surface exposed to UV irradiation for 10 minutes prior to measurement.

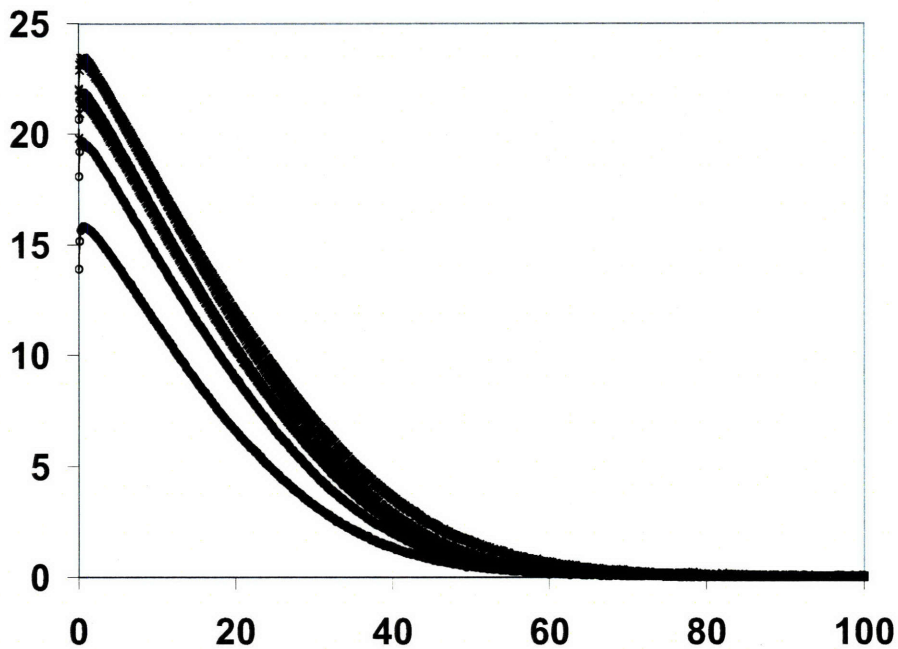


Figure 5.3. Force distance data for the UV-exposed surface before (circles) and after (hash marks) exposure of the surface to an additional ten minutes of irradiation at pH = 5.6. Differences in deflection are in line with differences arising from taking data at multiple positions on a sample, indicating that further UV exposure has little effect on behavior.

The trend of diminished repulsive interactions continues across pH values of 4.8 and 4.3, with the repulsive force of the UV exposed surface approximately half that of the surface stored in darkness. This is shown on the subsequent page in Figures 5.4 and 5.5. Additionally, the lengthscales over which the tip and surface interact appear to diminish slightly at these lower pH values. This suggests that UV irradiation not only reduces the surface potential of the (100) rutile plane, but also diminishes the characteristic Debye length, perhaps by trapping an increased number of indifferent ions at the surface. This might occur as a result of interactions between photogenerated electron-hole pairs, or between solvated species and charged defect sites at the surface.

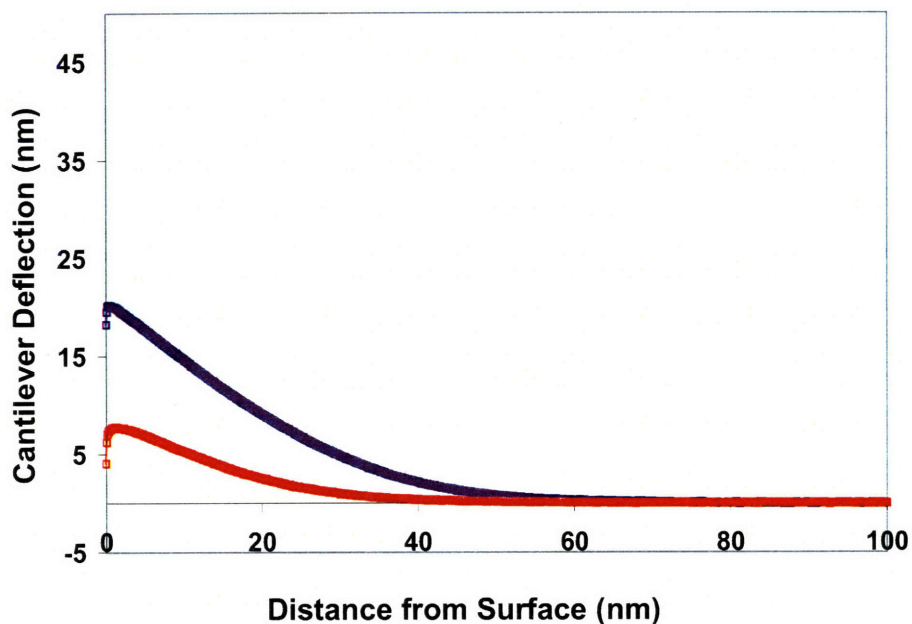


Figure 5.4. Force distance plots for a UV-exposed (red) and dark-stored (blue) rutile (100) surfaces at a pH of 4.8. The data continue to show a significant reduction in repulsive interaction and a slight decrease in the maximal distance from the surface over which the tip interacts with the sample, suggesting a decrease in Debye length of the photo-exposed surface.

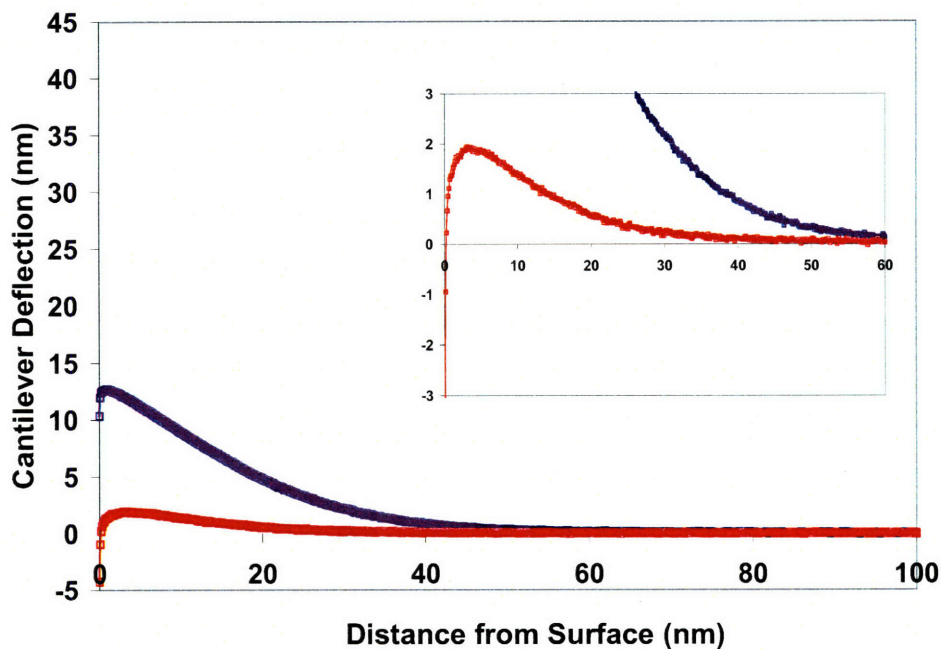


Figure 5.5. Force distance plots for a UV-exposed (red) and dark-stored (blue) rutile (100) surfaces at a pH of 4.3. The data show a continuance in the trend of figures 5.2 and 5.4. Inset shows that the UV-exposed surface is still clearly repulsive.

5.3.2 EDL Interactions of the 110 Surface

Force spectroscopy data of two samples of the same (110)-oriented rutile crystal taken at pH = 6.4 prior to exposure to UV are shown in Figure 5.6. The data show good correlation between the separate samples, indicating once again that one sample stored in dark can be used as a control to test against the sample exposed to UV. A comparison of the surface stored in dark and the surface exposed to 10 minutes of UV irradiation at the same pH is shown in Figure 5.7. Exposure to UV clearly induces a dramatic change in the interaction between surface and probe tip, changing the dynamics from repulsive to attractive. Because no change in EDL characteristics are expected from the probe tip, the switch is attributed to a change in the sign of the surface potential of the UV-exposed (110) surface.

Figure 5.8 underscores this point by showing the differences in the F-d curves of the two surfaces at pH = 5.7. The interaction between the silica probe tip and the surface stored in darkness remains repulsive, whereas the interaction between the tip and the UV-irradiated

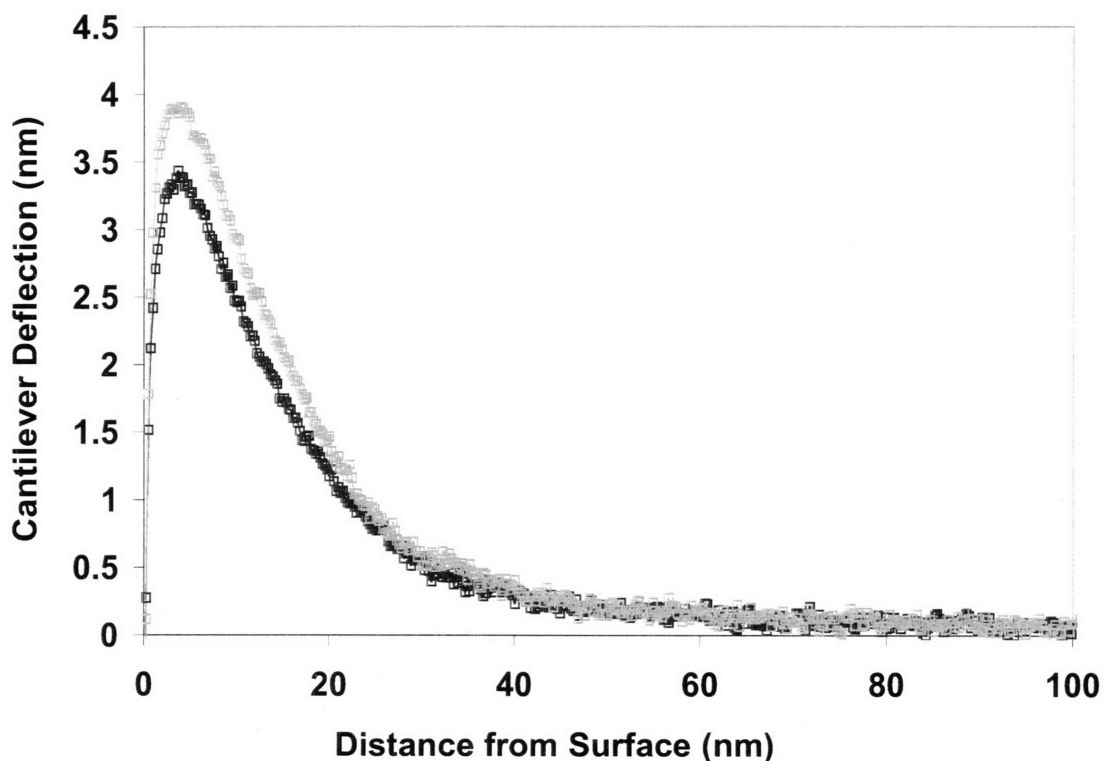


Figure 5.6. Force-distance curves of two identically-oriented (110) rutile surfaces prior to any UV exposure at a pH of 6.4. The data show no significant difference in interaction forces between the two samples.

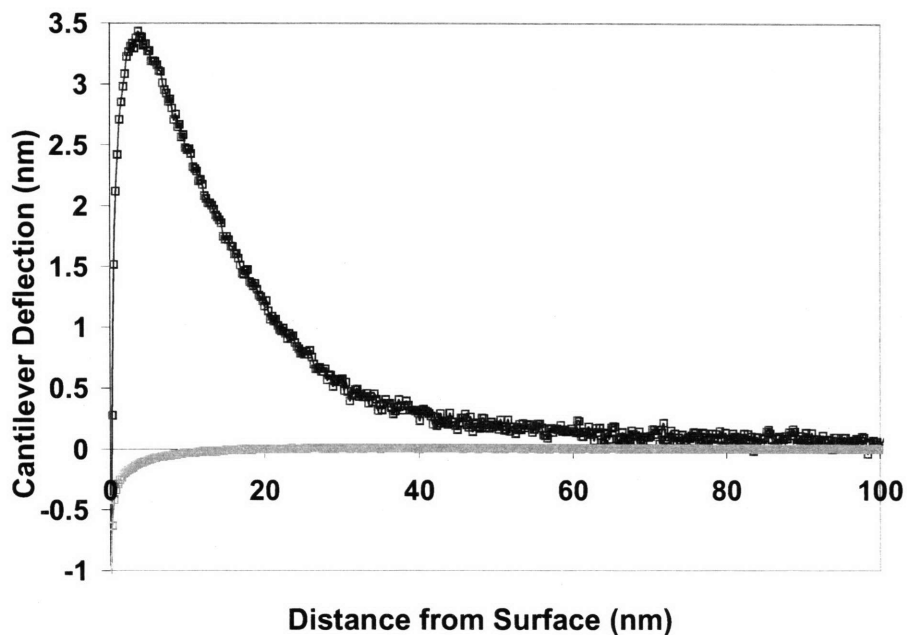


Figure 5.7. Force-distance curves of two identically-oriented (110) rutile surfaces shielded from (repulsive) and exposed to (attractive) 10 minutes of UV exposure at a pH of 6.4. The data show a dramatic shift in the nature of the interactions between tip and surface, indicating a photoinduced change in sign of the rutile EDL.

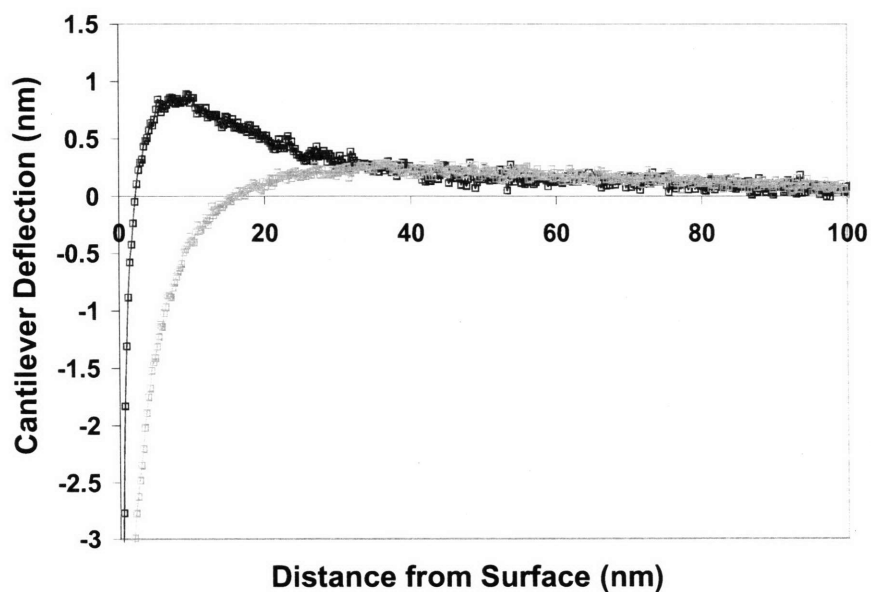


Figure 5.8. Force distance curves of the same two surfaces depicted in Figure 5.7 at a pH of 5.7 and after exposing one surface to 10 additional minutes of UV. The surface that has not been exposed to UV retains its repulsive interaction with the probe tip, ruling out contamination as a source of the observed behavior.

surface remains attractive. These data support the attribution of the shift from repulsive to attractive interaction on the UV-exposed surface to a change in the properties of the surface itself, rather than some (problematic) change in the properties of the probe tip.

The tip-surface interactions of the (110) surface stored in darkness shift from repulsive to attractive at $\text{pH} = 5.2$, roughly consistent with the iep determined for the surface in the previous chapter. Continued F-d measurements do little to distinguish between the UV-exposed surface and the surface stored in darkness, because differences in attractive interactions between samples are difficult to deconvolute, as shown by the data in Figure 5.9. These plots show that differences in characteristics between the two surfaces studied do not rise above the error in the attractive range of interaction.

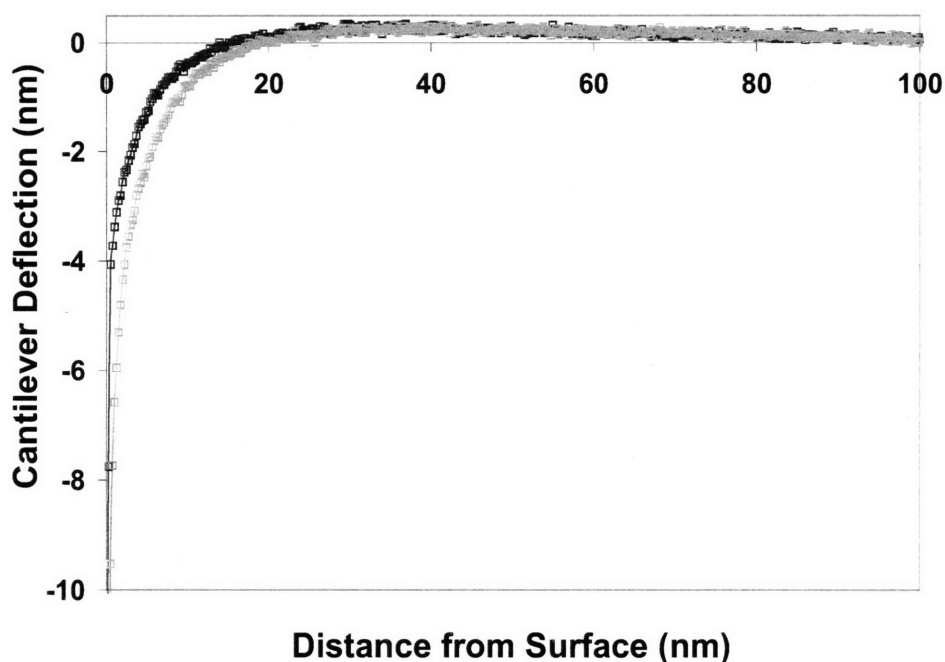


Figure 5.9. Force-distance measurements for the two (110) samples at $\text{pH} = 5.2$. Differences in attractive forces are difficult to see, and the variance shown here is not conclusively attributable to UV exposure.

5.3.3 Photoinduced Changes in Adhesion Forces

The retraction curves of both the (100) and (110) surfaces were also studied as a function of exposure to UV irradiation. Figure 5.10 shows a plot of the changes in adhesion forces for both the UV-exposed and untreated (100) surfaces as function of pH. The untreated surface exhibits essentially no adhesive interaction with the probe tip at pH = 6.4 (not shown) or pH = 5.5. An exemplary retraction curve is shown in the inset; its characteristics resemble that of two hard, non-deformable surfaces interacting. Slight increases in adhesive interaction are evident at pH = 4.8, and again at pH = 4.3.

Adhesion forces emerge more rapidly between the probe tip and the UV-exposed (100) surface. Although no adhesive interactions are observed at pH = 6.4 (not shown) either before or after UV illumination, they are readily seen at all subsequent pH values. These forces are observed to be significantly larger than the adhesive interactions observed between the tip and the untreated surface, approaching double the adhesion forces of the non-irradiated surface. This approximate inequality holds true at all values of pH studied here. Similar increases in adhesive interaction were observed on the (110) surfaces. Adhesive interactions increased as both a function of UV exposure and pH.

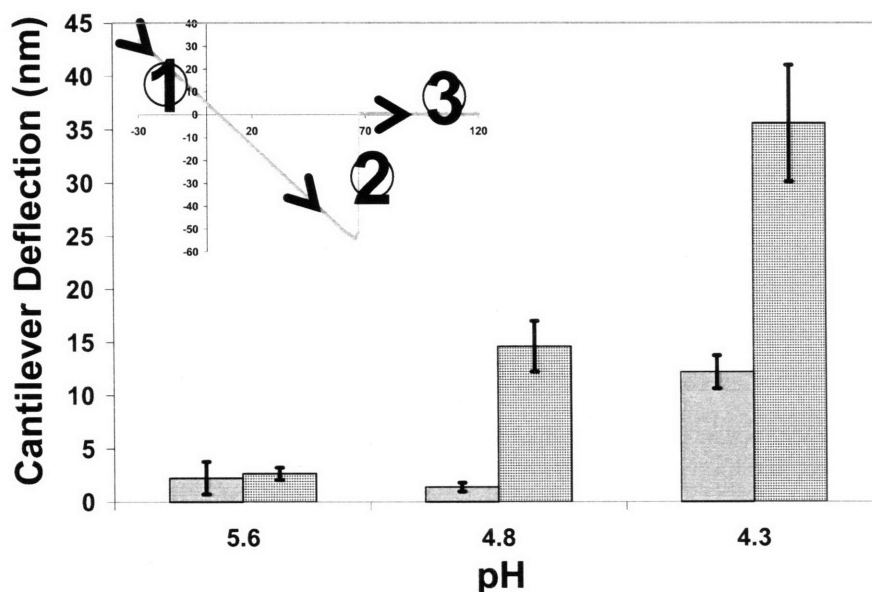


Figure 5.10. A plot of adhesive interaction as a function of pH for the (100) rutile surface stored in darkness (solid gray) compared to the UV-exposed surface (checkered). Exposure to UV promotes hydrophilicity of the rutile surface, which may result in increased hydrogen bonding with the hydrophilic colloid probe. Inset: A typical adhesion curve from which these data are gathered. See chapter 2 for a more detailed discussion.

5.4 Discussion

5.4.1 Influence of UV on EDL Interactions

Both the (100) and (110) rutile surfaces exhibit marked changes in the double layer properties as a function of UV irradiation. The (100) surface undergoes a significant decrease in repulsive interactions with the silica probe tip, indicating an appreciable decrease in surface potential. The (110) surface, on the other hand, shifts from a repulsive interaction to an attractive one, signifying a change of surface potential not only in magnitude but also in sign.

These results differ significantly from previous studies on the changes in properties of TiO₂ surfaces related to colloidal behavior. Dunn and coworkers, for example, studied changes in the electrophoretic mobility of anatase powders as a function of pH both in darkness and in the presence of UV illumination. Their data suggests no shift in the iep of powders exposed to UV, but does reveal a significant decrease in the electrophoretic mobility of particles upon UV exposure at pH levels lower than the iep of the material. They attribute this to an accumulation of negative charge on the surface which offsets the positively charged H⁺ species that adsorb at these pH levels. A study by Boxall and Kelsall, on the other hand, compared the electrophoretic mobility of amorphous titania powders in light and dark across a broad spectrum of pH values. This work showed an increase in electrophoretic mobility on both sides of the iep of the powder, corresponding to an increase in net positive charge on the surface at pH values lower than the iep, and increases in net negative charge at pH values greater than the iep.

Work by Moorthy and coworkers explored the ability to modulate electroosmotic flow through microchannels whose walls were coated with a deposited TiO₂ film. They found that changes in electroosmotic flow were greatest at pH levels near the iep of the surface, and attributed this to the generation of carriers that were not offset by the presence of large quantities of charged species in the EDL. Changes in flow at pH levels more acidic and more basic than the iep generated different responses. A change in the direction of flow was observed at lower pH, whereas in more basic solutions, the change in flow upon exposure to UV was much less drastic than changes near the iep, but in the same direction. The researchers attributed all of these results to increases in negative charge on the surface under all conditions, and cited the aforementioned work by Dunn in support of their findings. No mention is made of the crystal morphology of the TiO₂ films used in the work.

The changes in double layer interactions presented here cannot be explained within the same framework of the photogeneration of electrical carriers that interact on the surface. Studies on the (100) surface revealed decreases in EDL interactions at pH levels that were higher than the isoelectric point previously determined, whereas the studies discussed above suggested either no change or increases in the zeta potential of the systems at pH values greater than the iep. The observed shift in iep of the (110) surface is also not explainable by the models presented by other workers. This discrepancy may be rooted in the structural differences between the surfaces investigated in separate studies. The differing results suggest a different mechanism for the alteration of the surface potential of the (100) rutile surface in contrast to cumulative changes on other polycrystalline or amorphous TiO₂ surfaces.

It is worth noting that previous studies considered only the photolytic influence of UV irradiation on TiO₂ systems, focusing on the interaction of generated electron-hole pairs with both the surface and solvated species. This phenomenon originates as a bulk process in many polymorphs of TiO₂, with excitation of electrons across the band gap. The specifics of the interactions of these carriers at the double layer interface are not well-understood, and it is likely that behavior varies across both crystal structure and orientation, as well as between grains and grain boundaries. Moreover, UV irradiation has been shown to induce changes in the surface structure of rutile [15-16], weakening bonds between titanium atoms and bridging oxygen sites. The result is an increase in the adsorption of water molecules at these locations, which are generally believed to dissociate to form a pair of neighboring hydroxyl groups. However, changes in the properties of surfaces lacking these bridging oxygen groups, such as the (001) surface, have also been observed [17], which suggests that oxygen defects may also be generated at other lattice sites.

Ignoring for a moment the impact of excited electronic carriers, the generation of structural defects at oxygen sites, if uncorrected, would be expected to result in a surface containing titanium atoms of a slightly lowered average coordination number. A lower coordination number was previously linked to a lowered iep, as evinced by differences between iep among variously oriented rutile surfaces. The (110) surface, however, shifts to a higher iep upon irradiation. This suggests that vacancies created during exposure to UV are filled by some electron-rich species that results in the preferential adsorption of H⁺ at higher pH values. The adsorption of water at these locations may be such a possibility. Generally speaking, the changes

in EDL properties on both the (100) and (110) surfaces are likely related to both structural and electronic changes associated with UV irradiation. Their interplay is complex, however, and teasing out the origins of each influence may not be possible.

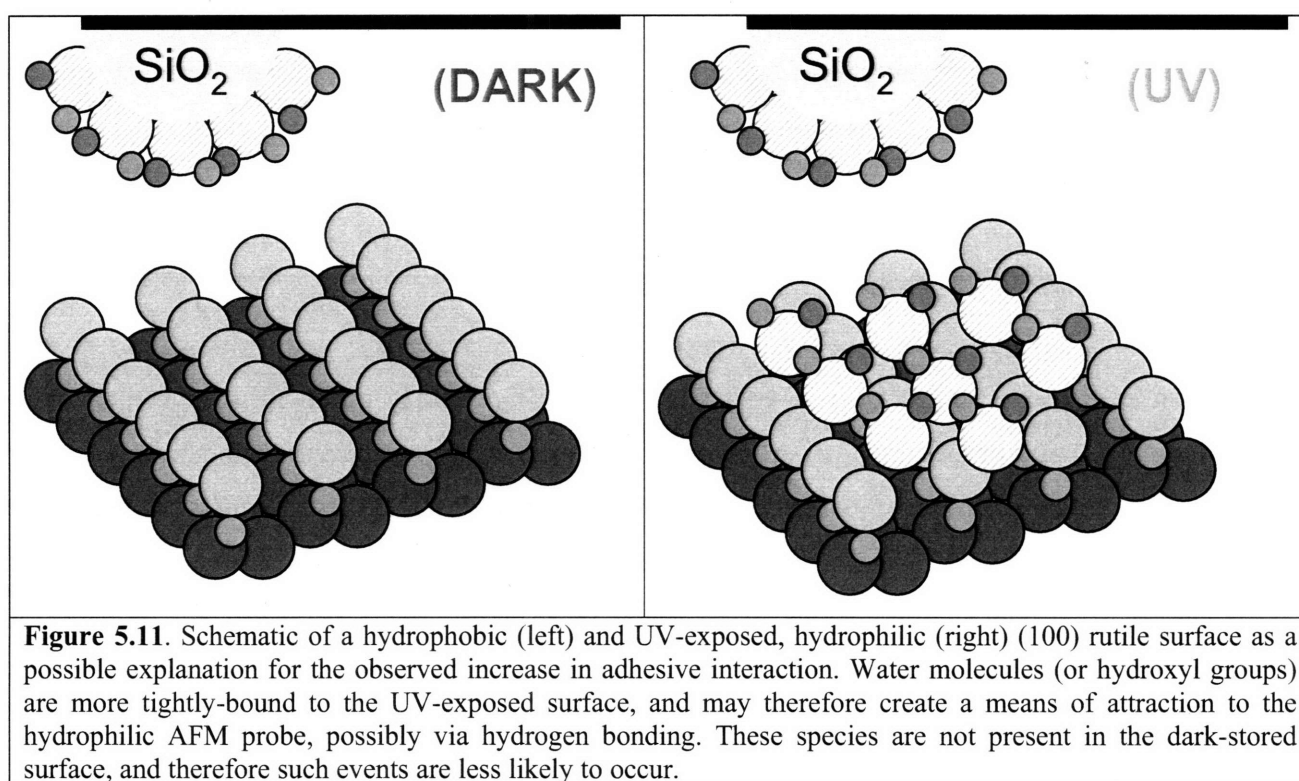
Evidence for an accumulation of charged species on the (100) surface, however, may be found in the observed decrease in the characteristic Debye length at low pH levels. A decrease in the Debye length of a surface is typically associated with a change in the ratio of surface potential to surface charge, as discussed in chapter 2. This is commonly achieved by an increase in the ionic strength of an electrolytic solution, which results in a greater charge density in the EDL and subsequent reduction in diffuse layer thickness. It is possible that increases in charge density are attributable to the interaction of photogenerated carriers at the surface with solvated ions in the double layer. The greater charge density might attract background electrolyte from solution, which would result in a small decline of double layer thickness and surface potential.

5.4.2 Influence of UV on Forces of Adhesion

Observed changes in the adhesion forces between rutile surfaces and silica spheres as a function of UV exposure are likely associated with the previously observed phenomenon of changes in wetting properties of these surfaces [15-16]. This light-induced amphiphilicity was explained by the creation of defective oxygen sites on a surface which were replaced by adsorbed water or hydroxyl groups. These groups improved the wettability of the surface by facilitating hydrophilic interactions with water molecules, such as hydrogen bonding. Hydrophilic nanodomains were observed to be ordered along the direction of bridging oxygen atoms on a given surface, resulting in an atomic landscape of what are considered oleophilic and amphiphilic regions. Macroscopic shifts in the wetting angle of water droplets on the surface were observed, with hydrophobic interactions signified by wetting angles of tens of degrees changing in favor of complete wetting of the surface.

This so-called “superhydrophilicity” signifies a photoinduced shift from a hydrophobic surface to an extremely hydrophilic one. The behavior may explain the observations made in this study of a generally larger adhesive interaction of the probe tip with the UV-irradiated surface than with the surface stored in darkness. Improved wettability of the rutile is expected to result in greater interactions between the tip, surface, and ambient water molecules. These interactions are likely to be manifest in increases in capillary forces between the surfaces of sample and tip,

which could emerge as a result of probe tip roughness, as well as in increases in hydrogen bonding. This second effect is a likely outcome of increased surface wettability, as water molecules adsorbed on the rutile surfaces could interact with those on the (also hydrophilic) silica sphere after contact has been made.



5.5 REFERENCES

- [1] A. Fujishima and K. Honda, "Electrochemical photolysis of water at a semiconductor electrode." *Nature* **238** (1972) 37
- [2] W.F. Jardim, S.G. Moraes, and M.M.K. Takiyama, "Photocatalytic degradation of aromatic chlorinated compounds using TiO₂: Toxicity of intermediates." *Water Research* **31** (1997) 1728
- [3] P. Pichat, "Partial or complete heterogeneous photocatalytic oxidation of organic-compounds in liquid organic or aqueous phases." *Catal Today* **19** (1994) 313
- [4] T. Ohno, T. Kigoshi, K. Nakabeya, and M. Matsumura, "Stereospecific oxidation of 2-hexene with molecular oxygen on photoirradiated titanium dioxide powder." *Chem Lett* **9** (1998) 877
- [5] B. O'Regan and M. Grätzel, "A low-cost, high-efficiency solar cell based on dye-sensitized colloidal TiO₂." *Nature* **353** (1991) 737
- [6] S. Sakaguchi, H. Ueki, T. Kato, R. Shiratuchi, W. Takashima, K. Kaneto, and S. Hayase, "Quasi-solid dye-sensitized solar cells solidified with chemically cross-linked gelators – control of TiO₂/gel electrolytes and counter Pt/gel electrolytes interfaces." *J Photochem Photobiol A* **164** (2004) 117
- [7] Q.B. Meng, K. Takahashi, X.T. Zhang, I. Sutanto, T.N. Rao, O. Sato, A. Fujishima, H. Wantanabe, T. Nakamori, and M. Uragami, "Fabrication of an efficient solid-state dye-sensitized solar cell." *Langmuir* **19** (2003) 3572
- [8] P.A.M. Hostenpiller, J.D. Bolt, W.E. Farneth, J.B. Lowekamp, and G.S. Rohrer, "Orientation dependence of photochemical reactions on TiO₂ surfaces." *J Phys Chem B* **102** (1998) 3216
- [9] J.B. Lowekamp, G.S. Rohrer, P.A.M. Hostenpiller, J.D. Bolt, and W.E. Farneth, "Anisotropic photochemical reactivity of bulk TiO₂ crystals." *J Phys Chem B* **102** (1998) 7323
- [10] H.O. Finklea, ed., "Semiconductor Electrodes." Elsevier, New York, 1988
- [11] O. Carp, C.L. Huisman, and A. Reller, "Photoinduced reactivity of titanium dioxide." *Prog Sol State Chem* **32** (2004) 33
- [12] W.W. Dunn, Y. Aikawa, and A.J. Bard, "Characterization of particulate titanium dioxide photocatalysts by photoelectrophoretic and electrochemical measurements." *J Am Chem Soc* **103** (1981) 3456
- [13] C. Boxall and G.H. Kelsall, "Photoelectrophoresis of colloidal semiconductors Part I: The technique and its applications." *J Chem Soc Farad Trans* **87** (1991) 3537

- [14] J. Moorthy, C. Khoury, J.S. Moore, and D.J. Beebe, "Active control of electroosmotic flow in microchannels using light." *Sensors Actuators B* **75** (2001) 223
- [15] R. Wang, K. Hashimoto, A. Fujishima, M. Chikuni, E. Kojima, A. Kitamura, M. Shimohigoshi, and T. Watanabe, "Light-induced amphiphilic surfaces." *Nature* **388** (1997) 431
- [16] R. Wang, N. Sakai, A. Fujishima, T. Watanabe, and K. Hashimoto, "Studies of surface wettability conversion on TiO₂ single-crystal surfaces." *J Phys Chem B* **103** (1999) 2188
- [17] A. Nakajima, S. Koizumi, T. Watanabe, and K. Hashimoto, "Effect of repeated photo-illumination on the wettability conversion of titanium dioxide." *J Photochem Photobiol A* **146** (2001) 129
- [18] A. Kanta, R. Sedev, and J. Ralston, "Thermally and photo-induced changes in the water wettability of low-surface-area silica and titania." *Langmuir* **21** (2005) 2400
- [19] J.M. White, J. Szanyi, and M.A. Henderson, "The photon-driven hydrophilicity of titania: A model study using TiO₂ (110) and adsorbed trimethyl acetate." *J Phys Chem B* **107** (2003) 9029
- [20] T. Zubkov, D. Stahl, T.L. Thompson, D. Panayotov, O. Diwald, and J.T. Yates, Jr., "Ultraviolet light-induced hydrophilicity effect on TiO₂(110)(1x1). Dominant role of the photooxidation of adsorbed hydrocarbons causing wetting by water droplets." *J Phys Chem B* **109** (2005) 15454

Chapter 6: Summary and Future Work

The study of anisotropic colloidal behavior of specific metal oxide surfaces provides an important connection between surface structure, chemistry, and properties. Various and complimentary techniques have now been used to detail this relationship in two prominent crystal systems, expanding the fundamental knowledge base in the field. The novel method of measuring the electron affinity of a surface *in vacuo* and correlating it to observed colloidal behavior in the form of relative values of isoelectric points suggests an effective approach to predicting relative behaviors without making direct measurements. Studies on the induction of changes in colloid behavior of model rutile surfaces via UV irradiation point to the viability of using external stimuli to tune surface properties in an aqueous environment. The author hopes that results from these experiments will serve as the foundation for future research thrusts aimed in a number of different directions. There are many opportunities to both continue the progression of the fundamental work that has been performed here, as well as to utilize much of what has been learned with an eye towards more practical engineering applications.

Perhaps the most evident area for further work is in the continued development of a library of the isoelectric points of model metal oxide systems as a function of crystallographic orientation. This work will help continue to bridge the gaps between surface complexation theory, colloidal behavior, and atomic structure, providing empirical data to serve as a check against existing models. Further, the continued coupling of conventional colloidal characterization techniques such as streaming potential and force spectroscopy with secondary means of analysis, such as XPS, strengthens both the quality of the current analysis and the possibility of developing predictive techniques to determine behavior *a priori*. The more times XPS analyses are successful in determining the relative acidities of oxide surfaces, the more readily the method will be accepted as valid. This may be essential to the study of surfaces whose properties in solution change over time, or whose interest resides in nonaqueous environments that may be difficult to study with conventional probative methods, such as the surfaces cathodic materials of lithium ion batteries.

Studies on both alumina and titania model surfaces can also be continued, with research focusing on the role of potential determining ions other than H^+ and OH^- . One interesting avenue of exploration would be a study on the behavior of polydentate ligands on highly ordered surfaces. A bi-dentate ligand might be chosen, for example, to be of a certain length and having

active groups targeted to bind to cationic surface sites of a given material. Differences in distances between cationic sites on different crystals may result in differences in surface complexation as a function of orientation. Surfaces with sufficiently small distances between cationic sites would be expected to interact with both ends of the ligand. A surface with distances between adsorption sites that were larger than the length of the entire ligand, however, may not be able to interact in the same way, leading to differences in which components of a ligand molecule are exposed at the interface. Alternatively, varying crystal structures of a given oxide might promote or inhibit the ordering of more complex potential determining species in ways that could raise or lower the free energy of the system. Such behavior would be akin to the adsorption of pentacene molecules on thiolated gold surfaces [1], which are known to adsorb onto the surface with benzene rings parallel to the surface at low concentrations, and normal to it in well-ordered rows at higher concentrations. If adsorption could be controlled by surface characteristics rather than by species concentration, surfaces could be tuned to expose specific faces of an adsorbing molecule at the interface, possibly in highly-ordered arrays.

The photoactive properties of titania provide another opportunity for applications in controlling colloidal behavior beyond what has been discussed in these pages. Their ability to catalyze chemical reactions might be harnessed to alter the characteristics of the EDL by facilitating reactions with organic species at specific locations on a surface. The electroosmotic properties of a monolayer of adsorbed organic material on a metal oxide surface are expected to differ from those of a pristine surface. Exposure of a titania surface to UV irradiation could drive an interaction with a specific solvated species, changing the nature of interactions between the titania and its environment. This permits both spatial and temporal control, and would be a novel way to dictate behavior. One additional degree of freedom is added through the ability to select a reacting species for specific properties, perhaps for example, allowing for the tuning of the iep to a specific value above or below the iep of the original oxide surface.

The current body of work studying the role of atomic structure on colloidal behavior has been largely successful in making strong connections between structure and properties, but is insufficient to explain this behavior at defect sites on a surface. The model systems used for study are assumed to be massive, monolithic surfaces whose equilibrium quantities of defects are too small to be studied with the relatively crude tools of streaming potential and AFM measurements. Fortunately, TiO_2 surfaces have served as model systems in a variety of fields for

decades, and all manners of introducing appreciable levels of defects are well-known [2-3]. These techniques could be used to introduce a known quantity of defects into the system, and comparisons could be made between the behaviors of equilibrium and defect-rich surfaces. The surface reconstruction of various orientations of rutile has also been studied (see [2]), providing the opportunity to control surface morphology at the atomic level through thermal treatments, and introducing controllable densities of faceted steps and terraces onto epi-polished faces. This too, could lead to an improved understanding of the behavior of rutile at defective surface locations, and might provide a means for complexation control at the atomic level.

Future work on titania behavior should also progress away from model systems and towards more realistic ones, such as thin films and polycrystalline surfaces. As a first step, work on anisotropic behavior should be studied in the context of these more complex surfaces, with measurements of the colloidal behavior performed at discrete, sub-micron positions on the surface. Recent work by Vandiver and co-workers, for example, showed differences in the surface charge density of hydroxyapatite at different positions on a polycrystalline surface, with values changing both across grains and as a function of the distance away from a grain boundary within a given grain [4]. This work was performed with site-specific force spectroscopy, using nanoscale colloid probe tips that are now commercially available, in which a topographic image of the surface is gathered using conventional AFM imaging, and force-distance measurements are performed on locations mapped by the image.

This work could be performed in conjunction with the orientation imaging microscopy (OIM) analysis technique [5], which is capable of determining via x-ray diffraction the crystallographic orientation and relative tilts of every grain of a polycrystalline material. The coupling of the two methods would allow for the individual analysis of the colloidal properties of every orientation present on a surface, and would also enable the study of the grain boundaries as well. Such a study might help to explain the large differences observed between the isoelectric points of conventional and single crystalline α -alumina powders, as discussed briefly in chapter 3. Moreover, it may be possible to probe the behavior of specific crystallographic orientations not commonly available from vendors as single crystal samples.

One major issue that will arise in future work is that few metal oxide systems are commercially available in sample sizes large enough to use with conventional streaming potential instrumentation. Brookhaven instruments is currently developing a fluid cell for use

with smaller samples, but surfaces will still have to be somewhere between 10 and 20 mm in at least one dimension. Although this work (and many others) has demonstrated the efficacy of force spectroscopy technique for probing the behaviors of a given surface, the method is not without its drawbacks. Work is limited to interactions in solutions in which the adhesive used to attach the colloid probe to the AFM cantilever is insoluble, ruling out work in many organic solvents that might be useful in exploring the interfaces in, among other things, lithium battery materials. The AFM technique also suffers from various sources of uncertainty; the reliability of results is intimately related to the cleanliness of the tip probes, the extent to which the colloid characteristics of the probe material are understood as a function of the experimental variable, and the stability of the numerous components of the instrument that are exposed to the suspension. This last concern relates to the metallic clip used to hold the cantilever in place, the optical coating and surface of the fluid cell used to protect the piezo-electric components of the instrument, and the gold-coated silicon or silicon nitride of the cantilever chip itself. Single crystal surfaces have an extremely low surface to volume ratio and highly limited number of adsorption sites, making them readily susceptible to contamination with tiny amounts of unwanted solute. AFM analysis is also limited to ionic strengths low enough to make detectable measurements of interaction forces, which typically compel researchers to operate in solutions between 1×10^{-4} M and 1×10^{-2} M. The lower limit may not be of significant consequence; there are significant questions as to the validity of the DLVO model below concentrations of this magnitude. The upper limit, however, prohibits studies of potentially practical interest.

Although streaming potential measurements lack site specificity and are not indicators of an actual interaction between two surfaces, their use is not restricted by solvent characteristics or electrolyte strength. The fundamental challenge to making quality streaming potential measurements, then, lies in transferring the technique to smaller sample sizes. A conventional fluid cell might be reduced in scale to handle the measurement of small single crystal surfaces. Perhaps a more interesting approach would be to fabricate a microfluidic device capable of operating on the smallest of surfaces. A substantial amount of work on this front has already been performed, and Appendix 2 contains a few calculations and observations on past failures and successes in this effort.

Results from this work also lay the foundation for more application-driven research in the area of photodirected assembly methods. The results from chapter 5 show a clear influence of

UV irradiation on the double layer characteristics of specific rutile surfaces. This behavior could be utilized to directly and locally alter the isoelectric point of a model surface, which would allow for the designation of specific interactions (repulsive or attractive) between the surface and suspended media. A more circuitous path to assembly control might also be achieved by altering the stability ratio of the substrate-particle interactions, using UV to control fast and slow flocculation kinetics without changing the sign of the EDL potential. Furthermore, the shift from hydrophobicity to hydrophilicity as a function of UV exposure could be utilized in conjunction with the influence of UV on the EDL to manipulate multi-component particle systems. Shifts towards hydrophilicity could be useful in directing the preferential adhesion of a hydrophilic particle over that of a hydrophobic one, as the well-known strong interaction forces between hydrophobic surfaces are diminished. This work could be used, for example, as a partial solution to the problem of synthesizing colloidal crystals with a diamond cubic structure, which are currently produced by placing silica and polystyrene spheres at alternating locations in a close-packed configuration, and subsequently baking out the organic, leaving only silica in half of the FCC lattice sites. A templated approach to synthesis would resolve the current issue of physically placing each individual sphere at its desired location.

REFERENCES

- [1] D. Käfer, G. Witte, P. Cyanik, A. Terfort, and C. Wöll, "A comprehensive study of self-assembled monolayers of anthracenethiol on gold: Solvent effects, structure, and stability." *J Am Chem Soc* **128** (2006) 1723
- [2] U. Diebold, "The surface science of titanium dioxide." *Surf Sci Rep* **48** (2003) 53
- [3] T.L. Thompson and J.T. Yates, "TiO₂-based photocatalysis: Surface defects, oxygen, and charge transfer." *Topics in Catal* **35** (2005) 197
- [4] J. Vandiver, D. Dean, N. Patel, W. Bonfield, and C. Ortiz, "Nanoscale variation in surface charge of synthetic hydroxyapatite detected by chemically and spatically specific high-resolution force spectroscopy." *Biomaterials* **26** (2005) 271
- [5] B.L. Adams, S. Ta'asan, D. Kinderlehrer, I. Livshits, D.E. Mason, C.T. Wu, W.W. Mullins, G.S. Rohrer, A.D. Rollett, and D.M. Saylor, "Extracting grain boundary and surface energy from measurement of triple junction geometry." *Interf Sci* **7** (1999) 321

APPENDIX: Matlab AFM Analysis Program

A Matlab code written for the rapid manipulation of the thousands of force-distance curves generated by AFM experiments is presented below. The code is the second of its kind to be written for AFM-related work in CPRL¹. This code is superior to the first in that capitalizes on a simpler algorithm resulting in faster analysis, although it lacks the convenience of a graphical user interface. However, the code presented below suffers from the limitation that if the jump-to-contact feature of an AFM curve is not larger than the noise among baseline data points, the data cannot be properly positioned along the x and y axes, although this problem does not often arise. Future versions of such an analysis program would benefit from an algorithm capable of detecting the jump-to-contact by means of discerning a change in the slope of the data set that arises after the tip has contacted the surface. A code similar to the one below was written for the analysis of retraction curves. Boldface text below indicates comments present in the original code. It appears alongside Matlab commands whenever possible.

itc.m

```
%*****
%The lines below take user input to identify the files of interest. AFM
%data is stored (in ASCII format) by date in YYMMDD format, and in folders
%under the directory C:\Research\AFM\TiO2_AFM\AFM_TiO2_YYMMDD\YYMMDD_ASCII.
%As long as this nomenclature remains consistent, the following lines of
%code should access the ASCII files of interest for analysis.

datadir = char(input('Enter the date on which these experiments were performed (YYMMDD): ',
's'));

datadirbase1 = char('c:\Research\AFM\TiO2_AFM\AFM_TiO2_'); %Build the necessary
character string
datadirbase2 = char('\'); %to open the proper files
datadirbase3 = char('_ASCII\');
datadirbase4 = char('_Processed\'); %Made for later (writing and saving files)

totaldatadir = mat2str([datadirbase1, datadir, datadirbase2, datadir, datadirbase3]);
totaldatadir = char(totaldatadir);

data_set = char(input('Enter the name of the dataset that you would like to analyze: ', 's'));
```

¹ See R.J. Kershner, Surface Forces During Electrophoretic Assembly of Micron Scale Silica Particles, *Doctoral Thesis*, M.I.T., 2004

**%The above line is a simplified version of a previous code that attempted
 %to open and analyze all files of a given experiment date at once. This
 %line requires the user to input a single experiment one at a time.**

```
all_files = dir([totaldatadir]);    %Opens the folder specified and places  

                                   %all files in a structured array
```

```
file_mat = strvcat(all_files.name); %The .name portion of the structured array  

                                   %contains the names of all the files in the folder. The  

                                   %strvcat command builds a vertical matrix of these  

                                   %strings
```

```
file_find = strmatch(data_set, file_mat); %Finds the files of interest matching user input for  

                                           %analysis
```

```
k_tip = 0.12; %Tip spring constant in N/m; will be user input  

diam_tip = 5; %Tip diameter in microns; will be user input  

rad_tip = diam_tip./2;
```

```
%*****  

%The lines below build a matrix of filenames whose prefixes match the  

%inputed value 'data_set'. This matrix will be called in a subsequent loop  

%to open and operate on the files of interest.
```

```
for i = 1:size(file_find, 1)  

    file_names(i, :) = file_mat(file_find(i), :);  

end  

%*****
```

```
warning off MATLAB:divideByZero
```

```
debye = 8;    %Define Debye length (could take user input)  

filenamecount=1;  

currentcol = 1; %Also unnecessary for the case where only one set of data is analyzed  

                 %at a given time. Use to scroll through colors (next) to  

                 %generate multi-color plots (at end)
```

```
colors = [0 0 1; 0 0.5 0; 1 0 0; 0 0.75 0.75;  

          0.75 0 0.75; 0.75 0.75 0; 0.25 0.25 0.25  

          0 0 1; 0 0.5 0; 1 0 0; 0 0.75 0.75;  

          0.75 0 0.75; 0.75 0.75 0; 0.25 0.25 0.25  

          0 0 1; 0 0.5 0; 1 0 0; 0 0.75 0.75;  

          0.75 0 0.75; 0.75 0.75 0; 0.25 0.25 0.25  

          0 0 1; 0 0.5 0; 1 0 0; 0 0.75 0.75;  

          0.75 0 0.75; 0.75 0.75 0; 0.25 0.25 0.25  

          1 1 0; 1 0 1; 0 1 1; 1 1 0.5; 1 0.5 1  

          0.5 1 1; 0.5 0 0; 0.5 0.5 0.5; 0 0 0.5;
```

```

0.5 0.5 0.25; 0.5 0.25 0.5; 0.25 0.5 0.5
0.5 0.25 0.25; 0.25 0.5 0.25; 0.25 0.25 0.5
0.5 0.5 0.75; 0.5 0.75 0.5; 0.75 0.5 0.5
0.75 0.75 0.5; 0.75 0.5 0.75; 0.5 0.75 0.75
0.25 0.5 0.75; 0.25 0.75 0.5; 0.75 0.25 0.5
0.75 0.5 0.25];
%*****

%*****
%Begin the for loop to run through and analyze all of the data sets of interest
for j = 1:size(file_names, 1)

    %4 lines below open file and locate beginning/ends of extend and
    %retract data:
    fname = char(file_names(j,:));
    contents = textread([totaldatadir fname], '%s','delimiter','\n','whitespace',""); %Parameters
copied from textread help file
    finder1 = strmatch('Extend Data', contents, 'exact');
    finder2 = strmatch('Retract Data', contents, 'exact');

    % The 2 loops that follow turn the character array (from above) into
    % 2 matrices - data_mat_ex and data_mat_ret - which contain all data
    % from the ASCII file of the extension and retraction curves for the
    % given experiment being opened at this point in the "for" loop

    for k = (finder1 + 1): (finder2 - 2)    %This loop takes data from cell "contents" and turns
                                           %it into an nx2 matrix
        data_line_ex = char(contents(k));
        data_build_ex((k-finder1), :) = sscanf(data_line_ex, '%f');
    end

    for m = (finder2 + 1):size(contents, 1)
        data_line_ret = char(contents(m));
        data_build_ret((m - finder2), :) = sscanf(data_line_ret, '%f');
    end

    data_mat_ex(:,1) = data_build_ex(:,1);
    data_mat_ex(:,2) = data_build_ex(:,2);
    data_mat_ret(:,1) = data_build_ret(:,1);
    data_mat_ret(:,2) = data_build_ret(:,2);

    %The following two lines and subsequent for loop reverse the deflection
    %data such that a plot of deflection vs. z position displays
    %interaction at low separation distance rather than high. The creation
    %of 'new_ex_mat' is then used to re-format data_mat_ex.

    orig_z = data_mat_ex(:, 1);
    n = length(orig_z) + 1;

    for p = 1:length(orig_z)

```

```

    new_z_vals(p) = orig_z(n-p);
end

if filenamecount == 1
    new_z_vals = new_z_vals'; %Piezo position data
end

new_mat_ex = [new_z_vals data_mat_ex(:,2) data_mat_ex(:,2).*(k_tip./rad_tip)];
data_mat_ex = new_mat_ex;

%*****
%Below loop finds the difference in value between neighboring
%deflection values in data_mat_ex, and builds an array ('diffval') of
%these values. The line following the loop makes all of these
%differences of positive sign so that the proper maximum difference can
%be located.

for q = 1:size(data_mat_ex,1)-1
    diffval(q) = data_mat_ex((q+1),2) - data_mat_ex(q,2);
end
diffval = abs(diffval);
[maxdiff, zdiffpos] = max(diffval); %Locate maximum diff val and its position
data_ex_min = data_mat_ex((zdiffpos - 1):(zdiffpos + 10), 2);
[jtc_val, jtc_pos] = min(data_ex_min); %Locate jump-to-contact position as minimum in
                                     vdW regime
[jtc_coord_row, jtc_coord_col] = find(data_mat_ex == jtc_val);

if size(jtc_coord_row,1) > 1 %Statement insures that the proper jtc value will be taken
    jtc_coord_row = min(jtc_coord_row); %should identical values be found
end

max_and_pos(filenamecount, 1) = jtc_val; %Build matrix of max diff val and its position
max_and_pos(filenamecount, 2) = jtc_coord_row;

%The following line shifts values such that maximal interaction is now at x = 0.
z_shift = data_mat_ex(:,1) - data_mat_ex((max_and_pos(filenamecount, 2)), 1);

%Define a baseline between 8 and 12 debye lengths to shift data in y
%direction (deflection = 0 at no interaction with surface). The
%positions in the matrices baseline_adj_min and baseline_adj_max that
%contain the minimum values in these arrays correspond to the positions
%of the values in z_shift that are closest to the exact values of
%10*debye and 15*debye (100 and 150 nm if Debye = 10).

baseline_adj_min = abs(z_shift - (10*debye));
[baseline_adj_min_val, baseline_adj_min_pos] = min(baseline_adj_min);
baseline_adj_max = abs(z_shift - (15*debye));
[baseline_adj_max_val, baseline_adj_max_pos] = min(baseline_adj_max);

%Define the zero-baseline shift as b/w max to min vals b/c values at
%longer distances away from surface occur first, since we have flipped

```

```

%the distances:
ex_shift_val = mean(data_mat_ex((baseline_adj_max_pos:baseline_adj_min_pos), 2));
ex_shift = data_mat_ex(:,2) - ex_shift_val;
%Repeat with actual force values as well:
F_shift_val = ex_shift_val.*k_tip;
F_shift = data_mat_ex(:,2).*k_tip - F_shift_val; %Convert deflection to force
F_shift_norm = F_shift./rad_tip; %Normalize forces for radius size

%Write shortened data file containing only zeroed force of interaction
%and a suitable baseline.

cut_data_ex = [z_shift(baseline_adj_max_pos:max_and_pos(filenamecount,2))...
              ex_shift(baseline_adj_max_pos:max_and_pos(filenamecount,2))...
              F_shift_norm(baseline_adj_max_pos:max_and_pos(filenamecount,2))];

%*****
%Also create data set of tip position (not piezo position) and zero it:

tip_z = z_shift + ex_shift;
tip_z = tip_z - tip_z(jtc_coord_row);
tip_mat = [tip_z, ex_shift, F_shift_norm];
cut_tip_mat = [tip_z(baseline_adj_max_pos:(jtc_coord_row + 50))...
              ex_shift(baseline_adj_max_pos:(jtc_coord_row + 50))...
              F_shift_norm(baseline_adj_max_pos:(jtc_coord_row + 50))];

%*****

if filenamecount == 1
    total_file_ex(:,1) = cut_data_ex(:,1);
    total_file_ex(:,(j+1)) = cut_data_ex(:,2);
    total_file_F(:,1) = cut_data_ex(:,1);
    total_file_F(:,(j+1)) = (cut_data_ex(:,2).*k_tip)./rad_tip;
    total_tip_ex(:,1) = cut_tip_mat(:,1);
    total_tip_ex(:,(j+1)) = cut_tip_mat(:,2);
    total_tip_F(:,1) = cut_tip_mat(:,1);
    total_tip_F(:,(j+1)) = (cut_tip_mat(:,2).*k_tip)./rad_tip;
else
    total_file_ex(:,j+1) = cut_data_ex(:,2);
    total_file_F(:,j+1) = (cut_data_ex(:,2).*k_tip)./rad_tip;
    total_tip_ex(:,(j+1)) = cut_tip_mat(:,2);
    total_tip_F(:,(j+1)) = (cut_tip_mat(:,2).*k_tip)./rad_tip;
end

currentcol = currentcol + 1;
filenamecount = filenamecount + 1;
end
%*****

%*****
%Add a final two columns to each matrix of data containing the standard
%deviation of the deflection (and force) values

```

```

for r = 1:size(total_file_ex, 1)

    mean_vect_ex(r) = mean(total_file_ex(r, 2:size(total_file_ex,2)));
    std_vect_ex(r) = std(total_file_ex(r, 2:size(total_file_ex,2)));
end

for rr = 1:size(total_tip_ex, 1)
    mean_tip_ex(rr) = mean(total_tip_ex(rr, 2:size(total_tip_ex,2)));
    std_tip_ex(rr) = std(total_tip_ex(rr, 2:size(total_tip_ex,2)));
end

mean_vect_ex = mean_vect_ex';
std_vect_ex = std_vect_ex';
mean_tip_ex = mean_tip_ex';
std_tip_ex = std_tip_ex';

for s = 1:size(total_file_F, 1)
    mean_vect_F(s) = mean(total_file_F(s, 2:size(total_file_F,2)));
    std_vect_F(s) = std(total_file_F(s, 2:size(total_file_F,2)));
end

for ss = 1:size(total_tip_F, 1)
    mean_tip_F(ss) = mean(total_tip_F(ss, 2:size(total_tip_F,2)));
    std_tip_F(ss) = std(total_tip_F(ss, 2:size(total_tip_F,2)));
end

mean_vect_F = mean_vect_F';
std_vect_F = std_vect_F';
mean_tip_F = mean_tip_F';
std_tip_F = std_tip_F';

%Add the mean and standard dev info as the last columns of data in each
%matrix (The 'size(x) + 1' insures it's the last column.)
total_file_ex(:, (size(total_file_ex,2) + 1)) = mean_vect_ex(:);
total_file_ex(:, (size(total_file_ex,2) + 1)) = mean_vect_ex(:) + std_vect_ex(:);
total_file_ex(:, (size(total_file_ex,2) + 1)) = mean_vect_ex(:) - std_vect_ex(:);
total_file_F(:, (size(total_file_F,2) + 1)) = mean_vect_F(:);
total_file_F(:, (size(total_file_F,2) + 1)) = mean_vect_F(:) + std_vect_F(:);
total_file_F(:, (size(total_file_F,2) + 1)) = mean_vect_F(:) - std_vect_F(:);

total_tip_ex(:, (size(total_tip_ex,2) + 1)) = mean_tip_ex(:);
total_tip_ex(:, (size(total_tip_ex,2) + 1)) = mean_tip_ex(:) + std_tip_ex(:);
total_tip_ex(:, (size(total_tip_ex,2) + 1)) = mean_tip_ex(:) - std_tip_ex(:);
total_tip_F(:, (size(total_tip_F,2) + 1)) = mean_tip_F(:);
total_tip_F(:, (size(total_tip_F,2) + 1)) = mean_tip_F(:) + std_tip_F(:);
total_tip_F(:, (size(total_tip_F,2) + 1)) = mean_tip_F(:) - std_tip_F(:);
%*****

%*****
%Plot data in four plots: Two of force, two of deflection, with each

```

**%parameter measured displayed fully in one plot (all curves) and averaged
%in another (mean values with standard deviation lines).**

%Plot cut/zeroed extension data in a colorful figure

```
figure(1)
for zz = 2:size(total_file_ex,2)
    plohandles(zz) = plot(total_file_ex(:,1), total_file_ex(:,zz));
    set(plohandles(zz),'color',colors(zz,1:3));
    hold on
end
xlabel('Distance from Surface (nm)')
ylabel('Cantilever Deflection (nm)')
title(['Deflection Curves for Experiment ', data_set])
```

%Plot cut/zeroed Force values in a colorful figure

```
figure(2)
for aa = 2:size(total_file_ex,2)
    plohandles(aa) = plot(total_file_F(:,1), total_file_F(:,aa));
    set(plohandles(aa),'color',colors(aa,1:3));
    hold on
end
xlabel('Distance from Surface (nm)')
ylabel('Interaction Force (mN/m)')
title(['Force Curves for Experiment ', data_set])
```

%Make plots of mean deflection (and force) data with standard deviation

%Deflection data in Fig. 3:

```
figure(3)
plot(total_file_ex(:,1), total_file_ex(:,(size(total_file_ex,2)-1)), 'k-+')
hold on
plot(total_file_ex(:,1), (total_file_ex(:,(size(total_file_ex,2)-1)) + ...
    total_file_ex(:,size(total_file_ex,2))), 'r')
hold on
plot(total_file_ex(:,1), (total_file_ex(:,(size(total_file_ex,2)-1)) - ...
    total_file_ex(:,size(total_file_ex,2))), 'r')
xlabel('Distance from Surface (nm)')
ylabel('Cantilever Deflection (nm)')
title(['Average Cantilever Deflection and Standard Deviation: Experiment ', data_set])
```

%Force data in Fig. 4

```
figure(4)
plot(total_file_F(:,1), total_file_F(:,(size(total_file_F,2)-1)), 'k-+')
hold on
plot(total_file_F(:,1), (total_file_F(:,(size(total_file_F,2)-1)) + ...
    total_file_F(:,size(total_file_F,2))), 'r')
hold on
plot(total_file_F(:,1), (total_file_F(:,(size(total_file_F,2)-1)) - ...
    total_file_F(:,size(total_file_F,2))), 'r')
xlabel('Distance from Surface (nm)')
ylabel('Interaction Force (mN/m)')
```

```
title(['Average Force and Standard Deviation: Experiment ', data_set])
```

```
%*****  
%Repeat plots from figure 1-4 for tip-adjusted data in figures 5-8:  
figure(5)  
for hh = 2:size(total_tip_ex,2)  
    plohandles(hh) = plot(total_tip_ex(:,1), total_tip_ex(:,hh));  
    set(plohandles(hh),'color',colors(hh,1:3));  
    hold on  
end  
xlabel('Tip Distance from Surface (nm)')  
ylabel('Cantilever Deflection (nm)')  
title(['Deflection Curves for Experiment ', data_set, 'Tip-Adjusted'])
```

```
%Plot cut/zeroed Force values in a colorful figure  
figure(6)  
for ii = 2:size(total_tip_F,2)  
    plohandles(ii) = plot(total_tip_F(:,1), total_tip_F(:,ii));  
    set(plohandles(ii),'color',colors(ii,1:3));  
    hold on  
end  
xlabel('Tip Distance from Surface (nm)')  
ylabel('Interaction Force (mN/m)')  
title(['Force Curves for Experiment ', data_set, 'Tip-Adjusted'])
```

```
figure(7)  
plot(total_tip_ex(:,1), total_tip_ex(:,(size(total_tip_ex,2)-1)), 'k-+')  
hold on  
plot(total_tip_ex(:,1), (total_tip_ex(:,(size(total_tip_ex,2)-1)) + ...  
    total_tip_ex(:,size(total_tip_ex,2))), 'r')  
hold on  
plot(total_tip_ex(:,1), (total_tip_ex(:,(size(total_tip_ex,2)-1)) - ...  
    total_tip_ex(:,size(total_tip_ex,2))), 'r')  
xlabel('Tip Distance from Surface (nm)')  
ylabel('Cantilever Deflection (nm)')  
title(['Average Cantilever Deflection and Standard Deviation: Experiment ', data_set, 'Tip-Adjusted'])
```

```
figure(8)  
plot(total_tip_F(:,1), total_tip_F(:,(size(total_tip_F,2)-1)), 'k-+')  
hold on  
plot(total_tip_F(:,1), (total_tip_F(:,(size(total_tip_F,2)-1)) + ...  
    total_tip_F(:,size(total_tip_F,2))), 'r')  
hold on  
plot(total_tip_F(:,1), (total_tip_F(:,(size(total_tip_F,2)-1)) - ...  
    total_tip_F(:,size(total_tip_F,2))), 'r')  
xlabel('Tip Distance from Surface (nm)')  
ylabel('Interaction Force (mN/m)')  
title(['Average Force and Standard Deviation: Experiment ', data_set, 'Tip-Adjusted'])
```

```

%*****
%The following section of the code outputs the data of interest in the form
%of an Excel-readable .dat file

process_dir = mat2str([datadirbase1 datadir datadirbase2 datadir datadirbase4]);

charbuild = char(['%7.4ft ']); %Build a character string long enough to format every
                             %column of the outputted data file
for bb = 1:size(total_file_ex, 2) - 1;
    sbuild(bb,:) = char(charbuild);
end
sbuild((bb+1),:) = char('%7.4f\n '); %Last format string must dictate a new line ('\n')

for cc = 1:size(sbuild,1)
    together((8.*cc-7):(8.*cc)) = char([sbuild(cc,:)]); %Build string of proper number of format
                                                %comands
end

cropfile = fopen([process_dir data_set '_ex.dat'],'w+');
for dd = 1:size(total_file_ex,1)
    fprintf(cropfile, together, total_file_ex(dd,:));
end
fclose(cropfile);

cropfile2 = fopen([process_dir data_set '_F.dat'],'w+');
for ee = 1:size(total_file_F,1)
    fprintf(cropfile2, together, total_file_F(ee,:));
end
fclose(cropfile2);

cropfile3 = fopen([process_dir data_set '_tip_ex.dat'],'w+');
for ff = 1:size(total_tip_ex,1)
    fprintf(cropfile3, together, total_tip_ex(ff,:));
end
fclose(cropfile3);

cropfile4 = fopen([process_dir data_set '_tip_F.dat'],'w+');
for gg = 1:size(total_tip_F,1)
    fprintf(cropfile4, together, total_tip_F(gg,:));
end
fclose(cropfile4);
%*****
end

```